2017

Low-temperature Fabrication Process for Integrated High-Aspect Ratio Metal Oxide Nanostructure Semiconductor Gas Sensors

William Paul Clavijo
Virginia Commonwealth University

Low-temperature Fabrication Process for Integrated High-Aspect Ratio Metal Oxide Nanostructure Semiconductor Gas Sensors

Ph.D. Doctoral Dissertation

by

William P. Clavijo

Advisor: Gary Atkinson, Ph.D.
Director Wright-Virginia Microelectronics Center
Associate Professor of Electrical and Computer Engineering

Department of Electrical and Computer Engineering
Virginia Commonwealth University
Richmond, Virginia
April 2017

Acknowledgement

First of all, I would like to thank my academic advisor, Dr. Gary Atkinson, not only for his invaluable help and support, but also for giving me the wonderful opportunity to work with him and learn from his experience. I also thank him for his encouragement during my undergrad and graduate studies at VCU.

I would like to thank to Dr. Surpriyo Bandyopadhyay, Dr. Karla Mossi, Dr. Michael Cabral, and Dr. W. Hong Yeo for serving as members of my committee and for all their great ideas for future work on my research.

I would also like to acknowledge Dr. Dmitry Pestov, Dr. Carlos Castano, Dr. Cy Wilson, Dr. Janos Volk and Dr. Romualdo Ferreira for their very advantageous ideas for my research.

I would also like to thank to my colleagues and friends at Wright-Virginia Microelectronics Center, Josh Starliper, Iftekhar Hossain, and Josh Smak for their help in the cleanroom.

I would also like to thank my parents, Manuel y Marcela for their unconditional support. I also thank my older brother, Luis, younger sister, Grace, and parents-in- law, Carlos and Sori for all their support.

Lastly, and most important, I would like to express my gratitude to my wife, Carla. Without her support and encouragement every day, my success would not have been possible.

Table of Content

List of Illustrations

List of Tables

Abstract

Low-Temperature Fabrication Process for Integrated High-Aspect Ratio Metal Oxides Nanostructures MOSFET Gas Type Sensors

By William P. Clavijo

A research dissertation submitted in partial fulfillment of the requirements for the degree of Doctor of Philosophy in Electrical Engineering.

Virginia Commonwealth University, 2017

Director: Gary Atkinson, PhD
Director Wright-Virginia Microelectronics Center
Associate Professor of Electrical and Computer Engineering

This work presents a new low-temperature fabrication process of metal oxide nanostructures that allows high-aspect ratio zinc oxide (ZnO) and titanium dioxide (TiO_2) nanowires and nanotubes to be readily integrated with microelectronic devices for sensor applications. This process relies on a new method of forming a close-packed array of self-assembled high-aspect-ratio nanopores in an anodized aluminum oxide (AAO) template in a thin (2.5 μm) aluminum film deposited on a silicon and lithium niobate substrate ($LiNbO_3$). This technique is in sharp contrast to traditional free-standing thick film methods and the use of an integrated thin aluminum film greatly enhances the utility of such methods. We have demonstrated the method by integrating ZnO nanowires, TiO_2 nanowires, and multiwall TiO_2 nanotubes onto the metal gate of a MOSFET (Metal-Oxide-Semiconductor Field-Effect Transistor) and the delay line of a surface acoustic wave (SAW) device to form an integrated ChemFET (Chemical Field-Effect Transistor) and a orthogonal frequency coded (OFC) SAW gas sensor.

The novel thin film AAO process uses a novel multi-stage aluminum anodization, alumina barrier layer removal, ZnO/TiO_2/Al_2O_3 atomic layer deposition (ALD), and wet release etching. This new process selectively forms the ZnO nanowires, TiO_2 nanowires, and TiO_2 multiwall nanotubes on the aluminum gate of the transistor while maintaining the remainder of the aluminum film intact for other integrated device components and interconnects. A fabrication process was also optimized to integrate multiwall TiO_2 nanotubes onto the delay line of an OFC SAW gas sensor using a sequential ALD of TiO_2 and Al_2O_3. The self-assembled high-density AAO template was selectively formed in an ultra-smooth 2.5 μm thick aluminum layer deposited through e-beam evaporation without the electropolishing required in AAO template formation in traditional 100 μm thick free standing films. The resulting nanopore AAO template consists of nanopores of 90 nm in diameter and 1 μm in height at an aerial density of $1.3x10^{10}$ nanopores/cm^2. This thin film AAO template was then filled with ZnO or TiO_2 using ALD at 200°C, forming polycrystalline ZnO nanowires, TiO_2 nanowires, and multiwall TiO_2 nanotubes inside the pores. The alumina template was then removed with a buffered sodium hydroxide, or chromic phosphoric acid solution leaving free standing ZnO nanowires, TiO_2 nanowires and multiwall TiO_2 nanotubes of 1-1.7 μm height and 40-100 nm diameter, offering an increase of up to 220X the surface area over a standard flat metal oxide film for sensing applications. The process is selective so that the remaining, unanodized aluminum film can be used for the source/drain contacts, reflectors or interdigitated transducers (IDT) required for other parts of these integrated sensor devices. The metal oxide nanostructures were characterized by SEM, EDX, TEM and Hall measurements to verify stoichiometry, crystal structure and electrical properties.

Additionally, the electrical response of ChemFETs and OFC SAW gas sensors with ZnO nanowires, TiO_2 nanowires, and multiwall TiO_2 nanotubes were measured using 25-200 ppm ammonia as a target gas at room temperature (24ºC). The ammonia response of the ChemFET with ZnO nanowires to the threshold limit value (TLV) concentration of ammonia (25 ppm), shows a +56 mV shift in threshold voltage, an overall sensitivity of 14%, an 8 minute response time, and a 27 minute recovery period. The ChemFET with TiO_2 nanowires showed a -50 mV shift in threshold voltage to 200 ppm NH_3, and a detection limit of 50 ppm NH_3. The ChemFET with multiwall TiO_2 nanotubes showed a 2.87% sensitivity to 25 ppm NH_3, an 8 minute response time, and a recovery period of 2 hours. On the other hand, the OFC SAW gas sensor with multiwall TiO_2 nanotubes showed a frequency shift of about 500 Hz to 200 ppm NH_3, a recuperation time of 45 minutes and a detection limit of 100 ppm NH_3.

The metal oxide nanostructure fabrication sequence that we present is accomplished at low-temperature (< 200 °C) and can be accomplished selectively, making it readily amenable to integration with standard MOSFET and SAW processing technology as well as other microelectronic sensors. This new process has initially been demonstrated using ZnO, and TiO_2 but is also adaptable to a variety of metal oxide materials using appropriate deposition methods as well as selective release methods. This allows the potential to conveniently fabricate a variety of high-aspect ratio metal oxide nanostructure based microelectronic sensors for a range of applications.

Chapter 1 Introduction and Motivation

A sensor is a device that converses nonelectrical physical or chemical quantities into electrical signal. This signal can be read by an observer or by an electronic instrument. They help electronics to have an interface with the real world. Sensors have become an essential element of process control and analytical measurement systems. There are innumerable applications for sensors of which most people are never aware. Applications include, for example, industrial monitoring, factory automation, the automotive industry, transportation, telecommunications, computers and robotics, environmental monitoring, health care, and agriculture; in other words, sensors are in all spheres of our life [1].

Rapid progress in semiconductor technology, involving microcomputers and VLSI (Very Large System Integration) has increased the capabilities of electronic equipment used in industry. New products and companies have emerged to develop an integration of sensors with electronic equipment. This has stimulated sensor devices to development new kind of technology in sensor applications. There are different physical and chemical quantities in nature. For that reason sensor technology could be classified as thermal, mechanical, chemical, magnetic and radiant [2]. Sensors could be also be divided in two categories depending on whether they use auxiliary source or not. First, self-generating or passive sensing systems are devices that do not require an auxiliary source. Second, modulating or active sensors generate an output signal with the help of an auxiliary force.

A sensing system has three basic components. Fig. 1.1 shows a simple block diagram of a sensing system. First, the input transducer is responsible to sense the outside world, and to gather information about a physical or chemical quantity. Second, signal

processing is required since the input signal is usually weak and it needs some kind of signal amplifier before going to the actuator. Third, the actuator gets the signal from the signal processing block and it converts it into some kind of action. The main goal of a sensing system is to making it smart where electrical signals created by the sensors are amplified, converted to digital form, and then transferred to a microprocessor all in one single chip.

FIG. 1.1. Block diagram of a sensor device.

Semiconductor chemical sensor technology is a very promising type of sensing system since there has been an increasing concerning about real-time monitoring of the environment. Semiconductor gas sensors will be vital over the years to study the effects of pollution on health and safety stress since hazardous, and vital gases are always around us. Gas sensors are needed to monitor these gases for safety, amenity, energy saving, health, environment protection etc. Gas sensors are utilized to avoid gas explosions, incomplete combustion accidents, exposure to poison gases, as thermal detectors and breathe control checkers, and CO detectors in auto damper systems [3].

A semiconductor gas sensor is defined as a sensor that used a semiconductor material for the receptor and/or transducer and could be classified into five different types: (1) resistor, (2) diode, (3) oxygen concentration cell, (4) MOSFET (Metal-Oxide-Semiconductor Electric-Field Transistor), and (5) SAW (Surface Acoustic Wave). As shown in Fig. 1.2, a semiconductor gas sensor has two main components: a receptor and a

transducer. The receptor is usually made of a material that changes its work function, dielectric constant, electrode potential, or mass when it is interacting with a target gas. On the other hand the transducer transform the changes of the receptor to an electrical signal.

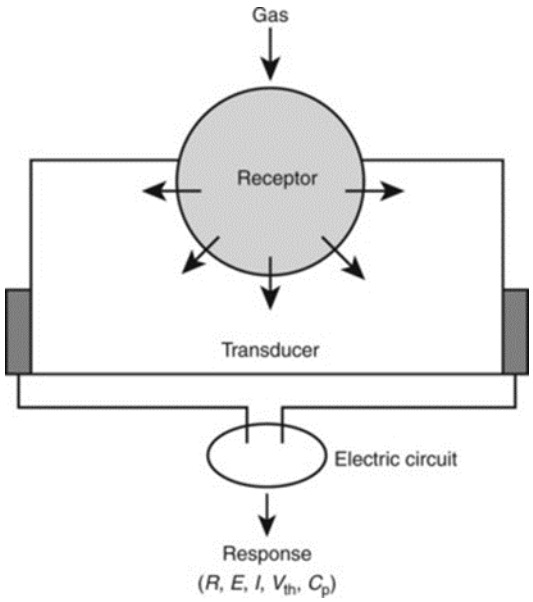

FIG. 1.2. Components of semiconductor gas sensor [4]

A semiconductor could be non-oxide (e.g. silicon) that can work as a transducer in the form of a MOSFET or MIS capacitor. A semiconductor could also be an oxide that can work as a receptor and transducer. Table 1.1 shows a summary of different type of semiconductor gas sensor with different types of material as receptor and transducer for different target gases [4-6]. Out of the five types of gas sensors, MOSFETs show a potential in the gas sensor market due to the potential of integration for an all-in-one chip for fabrication costs and low power consumption, and compatibility to current silicon fabrication technology. MOSFET are inherently more complex to fabricate and require more extensive control and measurement electronics. In addition, the MOSFET

configuration provides an amplification of electrical response. Therefore, the current flowing in a MOSFET is significantly higher than a typical chemiresistor structure.

Transducer	Response Signal	Receptor	Device (example)	Target
Resistor	Resistance	Oxides	Porous SnO_2, Sintered TiO_2	Air/fuel ratio (car engine)
Diode	Bias current	Oxides	Pd-TiO_2	H_2
MOSFET	Threshold voltage shift	Pd	Pd-gate FET	H_2, NH_3
		Oxides	WO_3-gate FET	NO_2
		Dielectrics	Cellulose-gate FET	Humidity
Oxygen cell concentration	Cell voltage	Oxides	Pt/zirconia/oxide/Pt	H_2, NH_3, NO_2
SAW	Frequency, Amplitude shift	Pd	OFC SAW device	H_2

Table 1.1. Classification of semiconductor gas sensor according to the transducer and receptor used [4-6].

Among the different types of gas sensors, SAW gas sensors are also very attractive because of their remarkable sensitivity to detect any perturbations of physical or chemical properties of a reactive layer placed along the direction of the traveling wave, introduced by the interaction with specific gas moles. SAW gas sensors have been widely explored for many applications in detecting chemical and biological components in a gas or liquid environment in a simple, direct and sensitive manner [7]. SAW sensors can be small sized, rugged, passive, wireless, and radiation hard with high sensitivity, fast real time response, and outstanding stability at low production cost. A SAW device could allow a more robust communication in harsh RF environments by adding orthogonal frequency coded (OFC) technology for ground testing, and aircraft applications [8-10]. OFC is represented as a one port SAW resonator with multi coded chip reflectors and a different resulting center frequency. The OFC SAW technology approach has been investigated for use in radio

frequency identification tag applications[10, 11], as well as hydrogen[6, 12], strain[13, 14], and temperature sensors[10, 15, 16]. Low-temperature integration of high-aspect ratio metal oxide nanostructures to the delay line of OFC SAW devices could potentially enhanced the electrical response and expand the range of capabilities of OFC SAW technology.

N-type semiconducting metal oxides such as: SnO_2, In_2O_3, WO_3, ZnO, TiO_2 and p-type semiconducting metal oxides such as CuO and Co_3O_4 are the main sensing materials for different gas sensor structures. Theses metal oxides changes its physical and electrical characteristics when are exposed to an inflammable or reducing gas (inorganic: H_2, CO, NH_3, H_2S, NO, etc; organic: CH_4, propane, alcohols, odorants, etc.), or when the sensor is exposed to oxidative gases (NO_2, ozone, N_2O, etc.) [17]. The prominent electronic, mechanical and chemical properties of nanostructured materials have emerged as attractive alternative to replace conventional bulk materials in semiconductor gas sensor technology.

The large band gap (3.37 eV), large exciton binding energy of 60 meV, transparency, ferroelectric and piezoelectric properties of zinc oxide (ZnO) have been used to develop functional nanostructures in a variety of device types, such as surface acoustic wave devices [18], photonic crystals [19], light emitting diodes [20], ChemFETs [21], solar cells [22], ferroelectric memories [23, 24], and piezoelectric nanogenerators [25]. ZnO nanostructures have been fabricated at low and high temperatures using vapor-liquid-solid (VLS) method, vapor-solid (VS) method, laser ablation-catalytic growth, oxide-assisted growth, template-induced growth, solution-liquid-solid growth in organic solvents, and metal-organic chemical vapor deposition (MOCVD) [26, 27]. High temperatures, pressure or the aggressive of the ambient required to grow one-dimensional nanostructures make

such methods problematic for direct device integration on the final transducer in a ChemFET. In some cases the nanostructures are grown at high temperatures separately and then transferred using drop coating [28], dielectrophoresis [29, 30] or roll transfer [31] which introduce issues with contact resistance at the interface between the metal oxide and the metal, which is problematic for chemical sensing applications [32]. Conventional low temperatures growth methods of ZnO nanowires have also been achieved [33-36] but to date are not in situ techniques readily integrated with microelectronic devices [37]. The advantage of the method presented here is the combination of low-temperature deposition and self-assembly techniques to allow easy integration of high surface to volume ratio nanostructures with microelectronic devices.

The remarkable physical and chemical properties of one-dimensional TiO_2 nanomaterials have also been extensively studied to develop the next generation of electronic devices and sensors. High dielectric constant (>50), excellent optical transmittance, high refractive index (2.6), high chemical stability, large work function (4.9 eV) and suitable energy bandgap (3.5 eV) have made titanium dioxide (TiO_2) a metal oxide semiconductor of prominent properties for applications in areas ranging from photovoltaics [38-41] and photocatalysis [42-44] to photo-/electrochromics [45-49] and sensors [50-55]. Fabrication of TiO_2 nanostructures for environmental applications have been receiving increased attention for enhancement of the electrical response during exposure to a reducing or oxidizing gas. TiO_2 nanostructures of different shapes for gas sensor applications have been synthesized at low and high temperatures using sol-gel [56], titanium substrate anodization [50, 57, 58], and citrate-nitrate auto combustion [59]. High temperatures, pressure or the aggressive of the ambient required to grow one-dimensional

nanostructures make such methods problematic for direct integration on to the delay of an OFC SAW device. There are other techniques to grow TiO_2 nanostructures separately using spraying precipitation [60], hydrolysis [61] and electrospinning [62]. The problem with these methods is that it adds contact resistance in the reactive area of the sensors [32]. Low temperature depositions of ultrathin films and nanocrystalline thin films by cathodic vacuum arc deposition [63], low-pressure chemical-vapor-deposition [64], supersonic cluster beam deposition [65], and DC magnetron sputtering deposition [66] have also been attained. However, growth of high-aspect ratio nanotubes using those deposition techniques has not been achieved for gas sensing applications. Furthermore, some of the high and low-temperature fabrication and deposition techniques are not suitable for mass production because they require complex, expensive equipment, and are time consuming. Here we present a low-temperature, manipulation free, fabrication technique of polycrystalline high-aspect ratio multiwall TiO_2 nanotubes compatible with standard SAW fabrication technology.

One approach that has been developed for the fabrication of one-dimensional nanostructures is the use the self-assembled nanoscale pores that develop when anodizing aluminum films under controlled conditions. Precisely controlled anodization of aluminum can result in the formation of a hexagonally close packed array of cylindrical nanopores with nanometer scale pore diameter and high aspect ratios [67]. One aspect of these fabrication processes that makes device integration challenging is that they are generally accomplished on a free-standing aluminum film. This is due to the fact that traditional methods of fabricating the AAO template generally rely on a thick (>100 μm) aluminum film as a starting substrate, which requires electropolishing to smooth the surface and make

it conducive to self-assembled hexagonally close-packed pore formation [68]. Additionally, Masuda *et al*. have shown that a multi-step aluminum anodization after electropolishing improves the uniformity of close-packed nanopore array [69]. However, the use of electropolishing to smooth the surface removes a substantial portion of the thickness, typically >20 μm. Although highly ordered and dense arrays of self-assembled nanopores can be fabricated by such methods, it is challenging to devise an integrated sensor process using a free standing AAO template. One challenge is devising a method to transfer the template to the solid substrate. The other challenge is the loss of tens of microns of film thickness in the electropolishing step, requiring an excessively thick starting film, which is not easily deposited with conventional aluminum deposition methods, such as evaporation or sputtering.

These anodic aluminum oxide (AAO) templates have been used to fabricate various types of nanowire structures by filling the pores with such techniques as electrochemical deposition, electroless deposition, soft gel-deposition, surface modification, template wetting, mask techniques, chemical vapor deposition and atomic layer deposition (ALD) [67]. Among the several deposition techniques, ALD appears to be one of the most promising for high-aspect ratio nanostructure fabrication due to its simplicity, reproductively and the high deposition conformality [70]. Gu *et al.* have expanded the potential applications of AAO templates by utilizing ALD to create highly ordered multiwall tube-in-tube nanostructures with up to five nested coaxial nanotubes within AAO templates [71]. A dramatic increase of the reactive surface area for sensor applications have resulted from the synthesis of such nanostructures on aluminum foils.

This work reports a low-temperature, manipulation-free, integrated fabrication process for the formation of high-density, high aspect ratio, ordered ZnO and TiO_2 nanostructure arrays using an integrated AAO template on the gate of MOSFETs and on the delay line of OFC SAW devices. As shown in Figs. 1.3(a)-(d), this a new low-temperature nanostructure fabrication process that allows high-aspect ratio nanowires and nanotubes to be readily integrated with microelectronic devices of four different configurations. Figs. 1.3(a)-(c) show ZnO and TiO_2 nanowires, and multiwall TiO_2 nanotubes on the gate of ChemFETs. Fig. 3(d) shows a OFC SAW device with multiwall TiO_2 nanotubes on the delay line. The ChemFETs structures consists of an e-beam evaporated aluminum film, a silicon dioxide dielectric layer and a standard <100> prime silicon substrate, whereas the OFC SAW device consists of e-beam evaporated aluminum film, and a 126ºYX $LiNbO_3$ substrate. As shown in Figs. 1.3(a)-(d), the result is freestanding metal oxide nanostructures attached to the top of an aluminum gate of the MOSFET, and the delay line of the SAW device to form integrated ChemFETs and OFC SAW gas sensors. The process is selective so that the aluminum film can be used for the source/drain contacts, reflectors or IDTs of the devices, since these regions are not anodized. While the process has been developed using ZnO and TiO_2 with a MOSFET and SAW structure, the selectively formed AAO template could be used to form other types of nanostructures, with a suitable deposition process, as well as being integrated with other microelectronic device structures that can incorporate an aluminum film deposition. The following section will explain basic concepts about the components of the sensor.

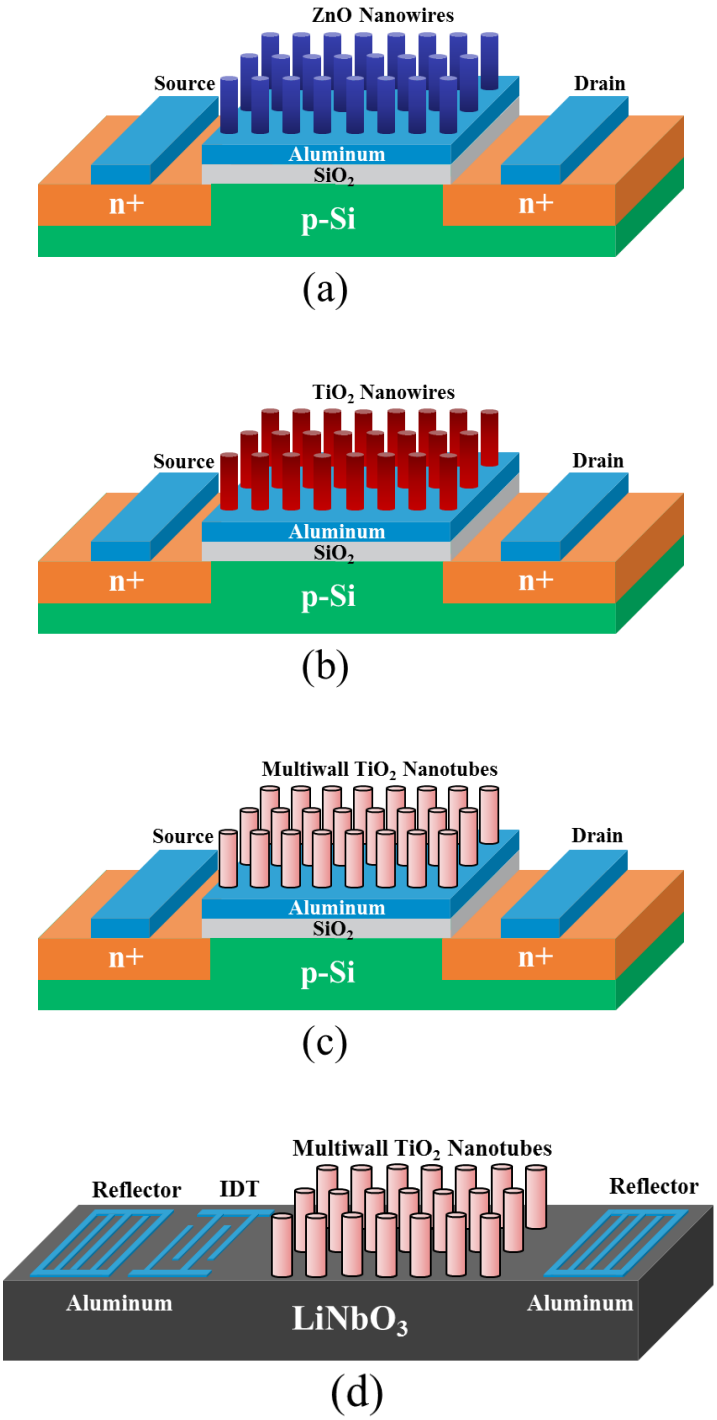

FIG. 1.3. ChemFET and OFC SAW gas sensor description. (a)(b) ZnO and TiO_2 nanowires on gate of a MOSFET device. (c) Multiwall TiO_2 nanotubes on gate of a MOSFET device. (d) Multiwall TiO_2 nanotubes on the delay line of SAW device.

Chapter 2 Theory and Background of MOSFET Type gas Sensors

ChemFET use the electronic characteristics of a MOSFET to detect a variety of gases. The MOSFET is responsible to covert gases variations into an electrical signal in a ChemFET sensor. The reaction between the metal oxide material and gas changes the electronic response of a MOSFET. The metal oxide material is the receptor material while the MOSFET is the transducer in a ChemFET sensor. This section will explain the theory and mathematic aim at describing the gas detection using the electronic characteristic of a MOSFET. First, some basic concepts about MOSFET must be understood.

2.1. Transducer Platform

The semiconductor field effect for a p-type bulk semiconductor states that if an electric field is applied to the surface of the semiconductor, a density of mobile charge carriers (holes) is enhanced and the surface is said to be accumulated. In that case, the excess charge appears at the surface and the electric field does not penetrate down to the bulk semiconductor. For the contrary, if the electric field forces the mobile holes away from the surface, a space charge region (ionized acceptor atoms) forms over a noticeable distance into the semiconductor. The strength of the electric field and the doping profile of the semiconductor determine the thickness of the space charge region. The surface will invert from n-type to p-type if the surface potential goes far from the bulk potential by containing an excess of mobile electrons. If the strength of the field increases even further, the surface potential will not change much but it will change the electron density in the n-type channel formed at inversion. If the surface is not inverted, the change in the surface electric field can be calculated by measuring the thickness of the surface depletion region.

If, on the other hand, the surface is inverted, the change in surface electric field can calculated by measuring the conductivity of the channel [72]. In the case of a ChemFET sensor, the surface field effect in the semiconductor can arise from a chemical effect on the gate materials. The density of mobile charge carriers at the surface inversion layer can change due to a modulation of the strength of the surface electric field. This change of the density of mobile charge carriers can be physically measured by looking at changes in current.

As shown in Fig. 2.1, a MOSFET is a four terminal (source, drain, gate, and base) semiconductor device which operates in the simplest form of a switch. The polarity and magnitude of a voltage applied to the gate (V_G) terminal determines the charge carrier density which can arise to an inversion layer under the gate. In case of an NMOS device (electron as carriers vs holes) in the off state (no gate voltage), the source and drain contacts are isolated from each other. If there is a voltage across the source and drain (V_{DS}) and no inversion layer, then the drain-to-substrate forms a p-n diode in reversed bias with no appreciable flow of current between source and drain. On the contrary, when the gate voltage above a threshold has enough strength to make an inversion layer at the surface of the semiconductor, an n-type conducting channel forms allowing flow of current between source and drain (I_D).

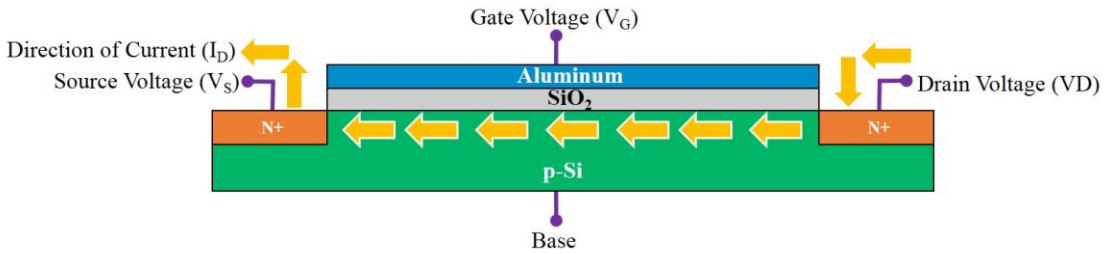

FIG. 2.1. Four-point terminal MOSFET structure.

The voltage can vary horizontally and gradually along the channel's length (L) from the source to drain. Vertically, it varies quickly from gate through the channel to the substrate. This approximation is useful for modeling and analysis of the I/V characteristics of a MOSFET. Fig. 2.2 shows a NMOS with the horizontal and vertical voltage variations across the metal-oxide-semiconductor interfaces when there is a conduction channel present [73]. As shown in Fig. 2.2, the channel at a point in y has a charge density $Q_n(y)$ per unit area of mobile electrons in the surface inversion layer and a charge density $Q_B(b)$ of ionized immobile dopant atoms in the space region.

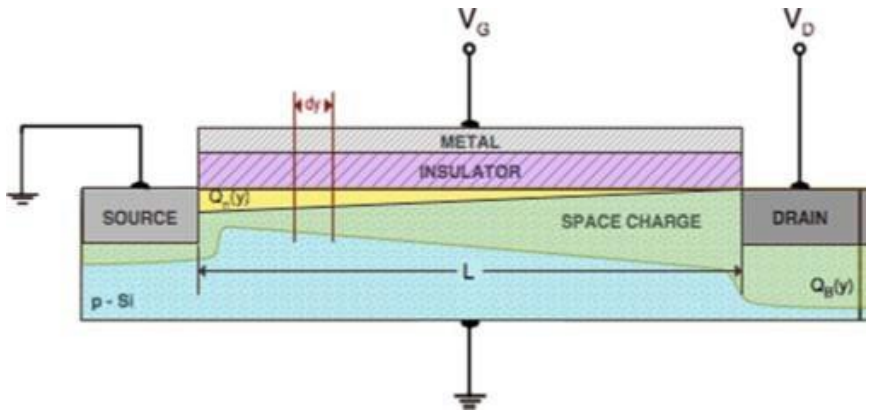

FIG. 2.2. Schematic of MOSFET in non-saturation mode [73].

The sum (Q_s) of $Q_n(y)$ and $Q_B(y)$ is equal and opposite to the charge per unit area on the metal plate that forms the other side of the metal gate.

$$Q_s = Q_n(y) + Q_B(y) \tag{2.1}$$

Where Q_s is related to V_G and the capacitance C_o of the gate insulator using

$$V_G - V_{FB} = -\frac{Q_s}{C_o} + \phi_S \tag{2.2}$$

Where the flat band voltage is defined as:

$$V_{FB} = \frac{\Phi_M - \Phi_{Si} + Q_{ss}}{C_o} \tag{2.3}$$

It accounts for the effects of the difference of work function of the metal gate (Φ_M), the work function of silicon (Φ_{Si}), and existed residual charge in the gate insulator (Q_{SS}). In case of an inversion layer, the mobile electron charge is given by:

$$Q_n(y) = -[V_G - V_{FB} - Q_s(y)]C_o - Q_B(y) \tag{2.4}$$

Assuming that the surface potential is given by the condition of strong inversion then

$$\Phi_S(y) = V(y) + 2\,\Phi_F \tag{2.5}$$

where Φ_s is the surface potential of the semiconductor and Φ_F is the Fermi potential. $V(y)$ accounts for the reverse bias, created by the n-type inversion layer and p-type substrate, applied in the perpendicular direction to the made field effect induced. If we assume that there is no mobile charges at all in the space charge region, then $Q_B(y)$ increases with $V(y)$ (voltage along y) at the expense of $Q_n(y)$ (mobile carriers) by:

$$Q_B(y) = -\sqrt{2\varepsilon_{Si}\varepsilon_o e N_A[V(y) + 2\Phi_F]} \tag{2.6}$$

where ε_{si} is the silicon permittivity, ε_o the is vacuum permittivity, e is the elementary charge, and N_A is the bulk doping concentration. Eq. 2.6 states that there is a weak dependence of $Q_B(y)$ on the voltage drop. In case to neglect that dependence then

$$Q_n(y) = -\sqrt{[-V_{FB} - Q_s(y)]C_O + 2(\varepsilon_{Si}\varepsilon_o e N_A \Phi_F)} \tag{2.7}$$

The voltage drop along y (dy) can be written as:

$$dV = I_D dR = I_D \frac{dy}{W \mu_n Q_n(y)} \tag{2.8}$$

where W is the width of the channel, and μ_n is the electron mobility in the channel. If we substitute $Q_n(y)$ into Eq. 2.8 and integrating over the channel length (L), it yields to I_D by:

$$I_D = \frac{\mu_n C_O W}{L} V_D(V_G - V_{th} - V_D/2) \tag{2.9}$$

where the threshold voltage (V_{th}) is defines as

$$V_{th} = V_{FB} + 2\Phi_F - Q_B/C_O \tag{2.10}$$

The derivation of Eq. 2.8 was made by assuming that inversion channel formed existed along all points. However, *V(y)* changes from 0 at the source to V_D, the conduction channel disappears near the end of the channel if V_D is large enough forming a pinch-off point in the drain region. At that stage the MOSFET becomes saturated as shown in Fig. 2.3. V_{DSAT} is defined as the drain voltage at which the conductive channel between source and drain disappears at the drain end.

$$V_{DSAT} = V_G - V_{th} \tag{2.11}$$

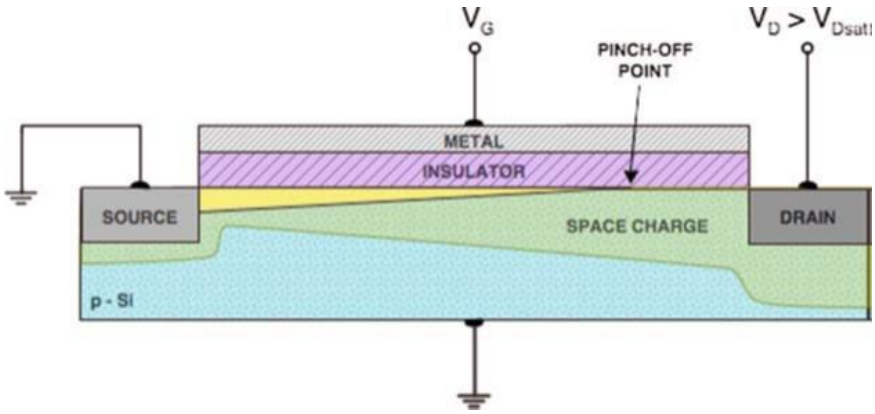

FIG. 2.3. Schematic of MOSFET in saturation mode [73].

A space between the channel and the drain region will occur if there is any further increment of V_D beyond V_{DSAT}. As shown in the I_D-V_D family of curves in Fig. 2.4, at that point I_D will still flow because electron do not see any potential barrier that restrict their flow from the channel across the space charge region to the drain. The number of electrons arriving at the drain region will be determined by the V_{DSAT}. Eq. 2.12 states I_D when V_{DS} is greater than V_{DSAT} provided the channel length (L) is not appreciably shortened by the space charge region the end of the channel and the drain.

$$I_D = \frac{\mu_n C_O W}{2L}(V_G - V_{th})^2 \tag{2.12}$$

Where V_{th} could be evaluated from the linear form of Eq. 2.12.

$$\sqrt{I_D} = (\frac{\mu_n C_O W}{2L})^{1/2}(V_G - V_{th}) \quad (2.13)$$

The I_D-V_D curves in Fig. 2.4 show the I/V characteristics of the different operation modes of a MOSFET (saturated and non-saturated) [72].

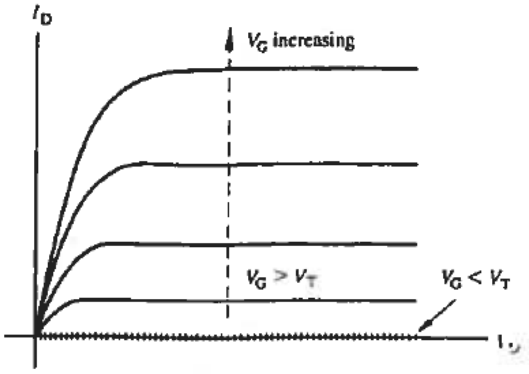

FIG. 2.4. I_D-V_D curves of a NMOS device [72].

2.2. Transducer Mechanisms

After fabrication of a MOSFET, the dimension, electron mobility, permittivity and doping concentration are fixed characteristics that will stay with the device. However, according to Eq. 2.9- Eq. 13, the I/V characteristic of the NMOS device can change if there are any adjustments to charges located in or at the surface of the insulator, the metal-to-semiconductor work function difference, and any internal gate voltage drop. The drain current of a NMOS in operation could change if the interaction between a target gas and the gate materials lead to the introduction of an internal gate voltage drop, a change in gate insulator charge, and/or change in the gate metal work function due to the injection of charge, charge separation at the gate contact/insulator interface or species capable of changing the metal work function. Fig. 2.5 shows an example of changes of the I/V characteristics of a ChemFET before and after exposure to NH_3. It is noted that V_{th} of the

ChemFET shifts during exposure to the reducing gas [5]. In this case the threshold voltage shift is attributed to a change in the potential gate due to the formation of a dipole layer when NH_3 is been dissolved into to the reactive gate material.

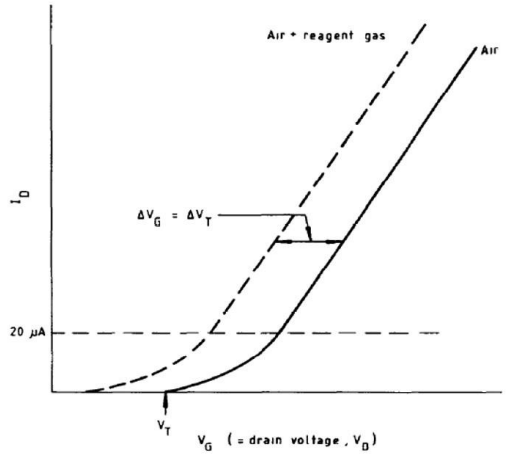

FIG. 2.5. Example of I_D vs. V_G characteristics of a ChemFET in atmospheric air (black solid line) and NH_3 exposure (dashed line) [5].

When a gas comes in contact with the gate materials surface, there is a charge transfer between adsorbates and the surface which leads to a separation of charge with a change in work function of the material. In the case of a ChemFET, the output signal is directly related to a change in the work function of the gate material upon exposure to a reducing or oxidative gas [74-76]. An overview of the surface process and examples of their influence on the device characteristics is shown in Fig. 2.6(a) – Fig. 2.6(d) where the figures on left correspond to a ChemFET structure under equilibrium, and on the right during exposure to oxidative and reducing gases. Fig. 2.6(a) and Fig. 2.6(c) show a cross sectional view of MOS structure under equilibrium where there is no change of work nor charge separation [77]. One the other hand, Fig. 2.6(b) shows the left side of MOS structure under exposure to reducing gases (H_2, NO, CO, NH_3 and O_2), while the right side shows the negative oxygen charges and gas by products after the chemisorption process. Fig.

2.6(b) shows that due to absorption of reducing gas molecules, there is an introduction of interface layers of dipoles at the interface between the reactive material and insulator. As shown in Fig. 2.6(d), due to the absorption on the gases molecules, there is an introduction of interface layers of dipoles at the metal/insulator interface. As a result there is a change in work function in the gate materials (band bending). This shows that the interaction between a reactive layer and a gas influences the characteristics of a MOS structure.

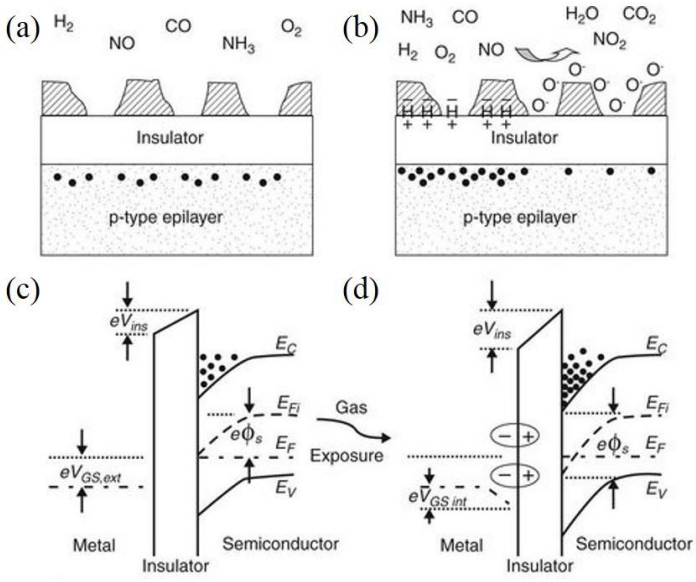

FIG. 2.6. Example of surface reaction and band diagram of metal-insulator-semiconductor structures. (a) and (c) Structures under equilibrium (atmospheric air). (b) and (d) structures under exposure to oxidative gases [77].

Upon adsorption of charge-accepting molecules, such as NO_2, at the vacancy sites, electrons are withdrawn and effectively depleted from the conduction band, leading in a change in surface potential of a ChemFET, hence changing its I/V characteristics. The sensing response to an oxidative gas can be represented using the following [78]:

$$NO - e^{-} \rightarrow NO^{-} \tag{2.14}$$

In the contrary, upon exposure in oxygen-rich environment, gas molecules such as CO, could react with the surface-absorbed oxygen and consequently release the captured electrons back to the depletion layer, resulting in change in the surface potential at the metal-oxide interface in a ChemFET. The sensing response to a reducing gas can be represented as:

$$CO + O \rightarrow CO_2 + e^- \tag{2.15}$$

In other words, CO gets oxidized to CO_2 consuming oxygen from the sensing material surface region. A rate between the rate of desorbing oxygen due to oxidation, and the rate of adsorbing oxygen of the ambient air is formed and the oxygen concentration on the sensor is reduced [79].

The separation of charge and change in work function does not provide much information of the composition of the gas. The selectivity and sensitivity depend on the specific interaction of absorption and desorption of molecules or atoms between the gate materials and the surrounding gas. The absorption of metal oxides and gas molecules depends on the ambient temperature, partial pressure of the substance, the desorption energy and the sticking coefficient. All of the specifics about the absorption will affect the equilibrium state of the molecules on the sensor surface [80]. More detailed information about the physical and chemical process between metal-oxide gas molecules will be explained in the next section.

2.3. Receptor Function and Transducer Function

Metal oxides materials, such as ZnO, TiO_2, SnO_2, exhibit unique interactions with reducing and oxidative gases. When a metal oxide comes in contact with an oxidative gas, such as O_2, the host semiconductor supplies electrons to the gas to allow it to be absorbed

as anionic species (ionosorption) such as O^-, O_2-. On the other hand, the gas donates electrons to the host semiconductor when it comes in contact with a reducing gas, such as NH_3. However, in this case the electron to be absorbed is in the form of a cationic species, like NO^+. The two way exchange of electrons between the host metal oxide and the gas comes from the bulk to the surface or vice versa [81]. This effect is accompanied with a change in energy band structure in the metal oxide. When a gas comes in contact with an n-type metal oxide, such as ZnO, the electron transfer with the gas and the bulk of the semiconductor results in the formation of an electron-depleted layer in the semiconductor.

In a case of porous uniform stack of grains of a n-type metal oxide semiconductor, each grain plays the role of receptor while each contact between grains plays the role of transducer. As shown in figure Fig. 2.7(a), the depletion layer (no charge carriers) thickness (*w*) in a grain increases as oxygen adsorption as anionic species increases [4]. Consequently as shown in Fig. 2.7(b), a double Schottky barrier is formed between grains. This barrier determines the change of surface potential and work function of the metal oxide. On the contrary, the depletion layer decreases as the adsorbed oxygen is consumed with an inflammable or reducing gas.

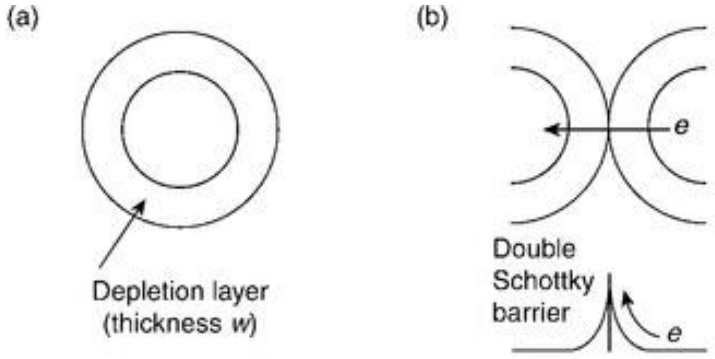

FIG. 2.7. N-type metal oxide grains under exposure to a oxidative gas. (a) Grain shows a depletion layer. (b) Formation of a double Schottky barrier between grains [4].

There are two main models of electron transfer between grains. First, in the double-schottky barrier model electrons move from grain to grain due to a mitigation of the potential barrier when the metal oxide grain is exposed to a reducing gas, as shown in Fig. 2.8(a) [82]. On the other hand, when grains are exposed to oxidative gas, the potential barrier increases its height resulting in an increment of surface potential and work function. Second, Fig. 2.8(b) shows that electrons can also be transported by tunneling when the space between oxide grains is very small and not necessarily in contact. In this case, change in electrical response of the sensing layer is still attenuated by the surface potential of oxide grains.

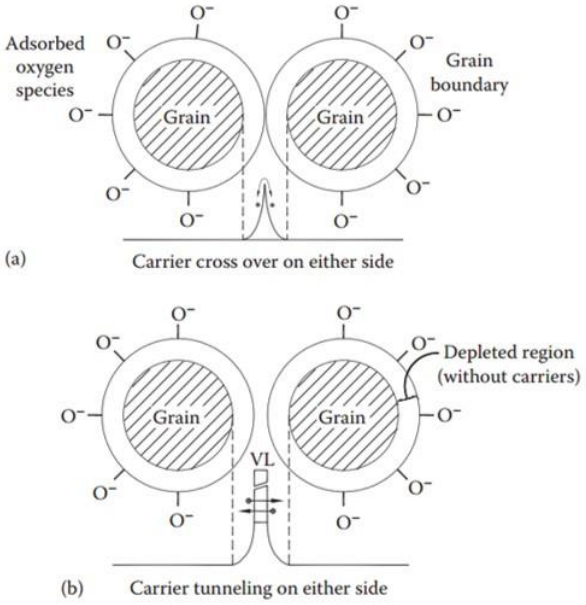

FIG. 2.8. Electron transfer models. (a) Electrons flow from grain to grain due to the mitigation of the potential barrier. (b) Electron transportation between grains by tunneling [82].

Surface reactions, corresponding charge transfer process, and their translation into variations of the electrical response occur during the exposure of a metal oxide to a gas. A diagram with physical and band models of the various elements involved during the

exposure of n-type metal oxide to a gas exposure is explain in Figs. 2.9(a)-(b) [83]. During exposure to atmospheric oxygen and/or oxidative gas, a depletion layer is formed on the surface of the grains in the metal oxide, as shown in the physical model in Fig. 2.9(a). On the contrary, when it is exposed to a reducing gas, such as NH_3, the negative charged trapped on the surface are reduced by the formation of NH_3 and H_2. This results on the reduction of the depletion layer in each grain and the reduction of the Double Schottky barrier between grains. The band model shown in Fig. 2.9(b) demonstrates that flow of conduction band electrons and the tunneling of charge carriers across the barriers of metal oxide grains is possible when grains are exposed to a reducing gas. The measurable result in a ChemFET is the change of work function in the metal-oxide interface, hence changing the I/V characteristic of the MOSFET. It is worth point out that the interaction in gas does not influence the entire grain. Grains have a space charger layer and an unaffected area.

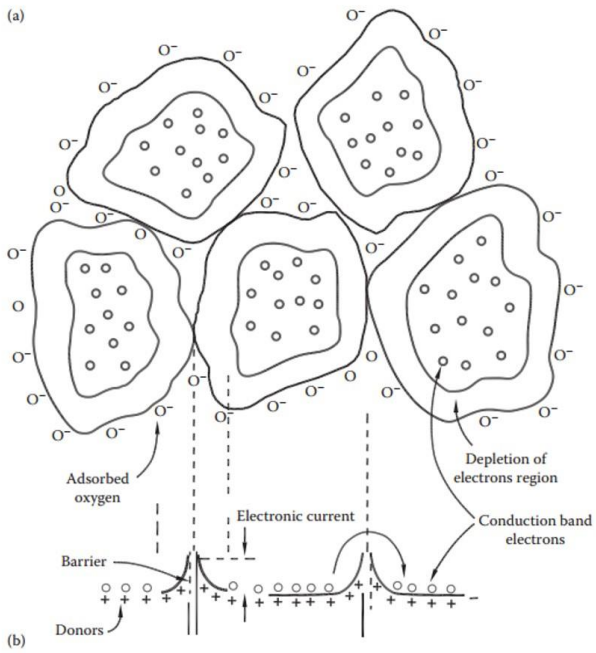

FIG. 2.9. Polycrystalline metal oxide structure. (a) Physical model. (b) The corresponding band model [83].

During exposure of an n-type metal oxide to atmospheric air, acceptor levels are created and electrons located in the conduction band are trap, as shown in Fig. 2.10(a) [84, 85]. This creates a depletion layer on the surface of the grains, bending of the upward band, making electrons to require more energy to reach the surface. Hence the dipole formation between metal oxide is control by the Schottky barriers formed between grains. As shown in Figs. 2.10(a)-(b), in the case of exposure to CO, the metal oxide reacts with the pre-absorbed oxygen, forming a dispersion of CO_2 to the atmosphere. These surface reactions of exchange of molecules are the basis of sensing as the receptor function. The charge transfer, during the surface chemical reaction, determines the result measure effect, I/V characteristics in case of ChemFET. As shown in Fig. 2.10(b), the reaction of CO with ionsorbed oxygen decreases the surface negative charge decreasing the energy barrier height between grains. This enables a progressively greater number of electrons to flow from grain to grain resulting in a change of work function of the interface between metal oxide and metal layer of ChemFET.

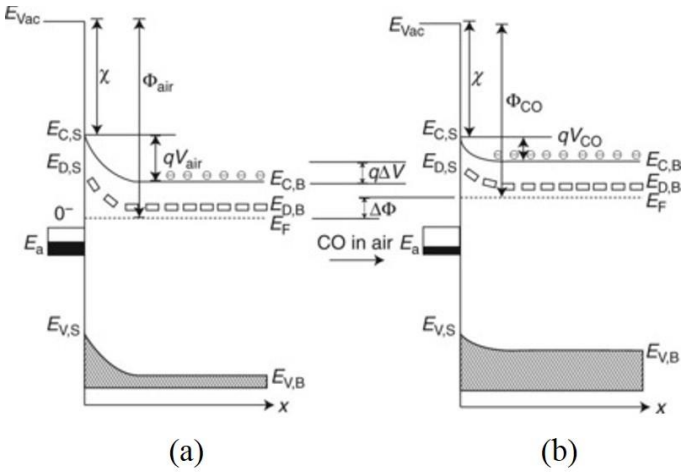

FIG. 2.10. Energy band representations of an n-type metal oxide. (a) Contributions to the work function in atmospheric air. (b) Contributions to the work function in CO [84, 85].

The magnitude of the change in surface band bending ($q\Delta V$) is a measure of surface reactivity and it controls the electrical response of the ChemFET. To measure its changes, one can measure the change in work function ($\Delta\Phi$) defined by

$$\Delta\Phi = q\Delta V + \Delta\chi + \Delta(E_{C,B} - E_F) \tag{2.16}$$

As describe in Eq. 2.16, the changes in the work function can be cause by changes in the band bending ($q\Delta V$), electron affinity ($\Delta\chi$) or the bulk position of the fermi level ($\Delta(E_{C,B} - E_F$) = electrochemical potential). This is also shown in Fig. 2.10(b) where it demonstrates the influence of CO reaction in air on the work function of metal oxide. One can measure the dependence of the change in electrical response of the ChemFET on the surface band bending in different conditions, and therefore the conduction mechanics can be identified.

2.4. Nanostructured Metal Oxide as Reactive Sensing Material

Assuming that the intrinsic characteristics of the metal oxide material remain constant, the relationship between the change of the surface charge and the change of the electrical response depends on the morphology of a thin film layer. Figs. 2.11(a)-(b) show a comparison of the accessibility to gases between a porous film and a compact layer [84]. In the case of Fig. 2.11(b), interaction between compact layer and gas happens only at the very surface and the flow of current is only influenced by the thickness of the depletion layer which is very small. Even though there is a depleted region on top of the metal oxide semiconductor, it will not be enough to produce a large change in work function at the metal-oxide interface. In contrast, as shown in Fig. 2.11(a), gas penetrates the entire porous layer making each individual grain to be affected to the gas composition. Consequently the current across the porous layer is determined by the barrier between all grains. Therefore, porous n-type semiconductor metal oxides are superlative for gas sensing applications

since the electric output response is influenced by the back to back Schottky barrier between grains.

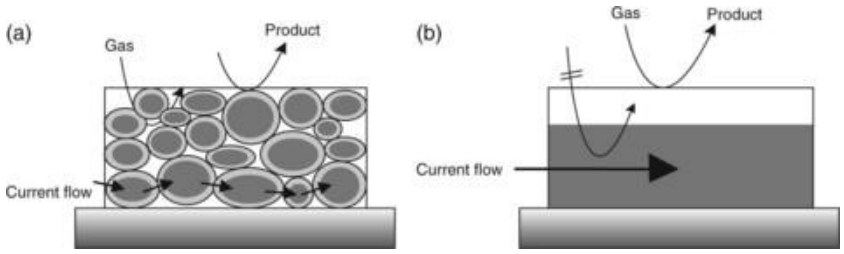

FIG. 2.11. Morphologies of metal oxide materials. (a) Porous layer. (b) Compact layer [84].

Metals oxides are the most common material used as reactive layer in chemical gas sensors. They were originally used in form of 2-D nanostructures (thin films). 1-D nanostructures, such as nanotubes and nanowires, have greater advantages than their 2-D nanostructures counterparts. 1-D nanostructures made of ZnO and TiO_2 have greater chemical sensitivity than thin film reactive layers due to the superlative surface-to-volume ratio. In addition, 1-D nanostructures have better crystallinity, higher purity, and their crystallinity orientation can be controlled better than 2-D nanostructures [86-88]. The integration of 1-D nanostructures to a variety of low cost and low power consumption electronics devices shows great prospective. This could potentially create new gas sensors with superior gas sensibility. However, large-scale integration of 1-D nanostructures has not been achieved yet [37].

In this work, high-aspect ratio polycrystalline ZnO nanowires, TiO_2 nanowires and multiwall TiO_2 nanotubes were fabricate at low temperature on top of an aluminum gated MOS transistor and on the delay line of a SAW device in order to produce a novel ChemFET and OFC SAW gas sensors. The low temperature fabrication process of high aspect ratio metal oxide nanostructures can be readily integrated with MOS and SAW

technology. This work demonstrates that the I/V characteristics of the ChemFETs with high aspect ratio metal oxide nanostructures change due to chemisorption of oxygen and ammonia gas. Fig. 2.12(a) shows a representation of the components and different terminals of the ChemFET sensor with high-aspect ratio metal oxide nanostructures on top of the gate of the MOSFET. Furthermore, this work also demonstrates that high aspect ratio multiwall TiO_2 nanotubes could serve as an active component in OFC SAW gas sensor. Fig. 2.12(b) shows a representation of the components of a OFC SAW gas sensor device with multiwall TiO_2 nanotubes on the delay line.

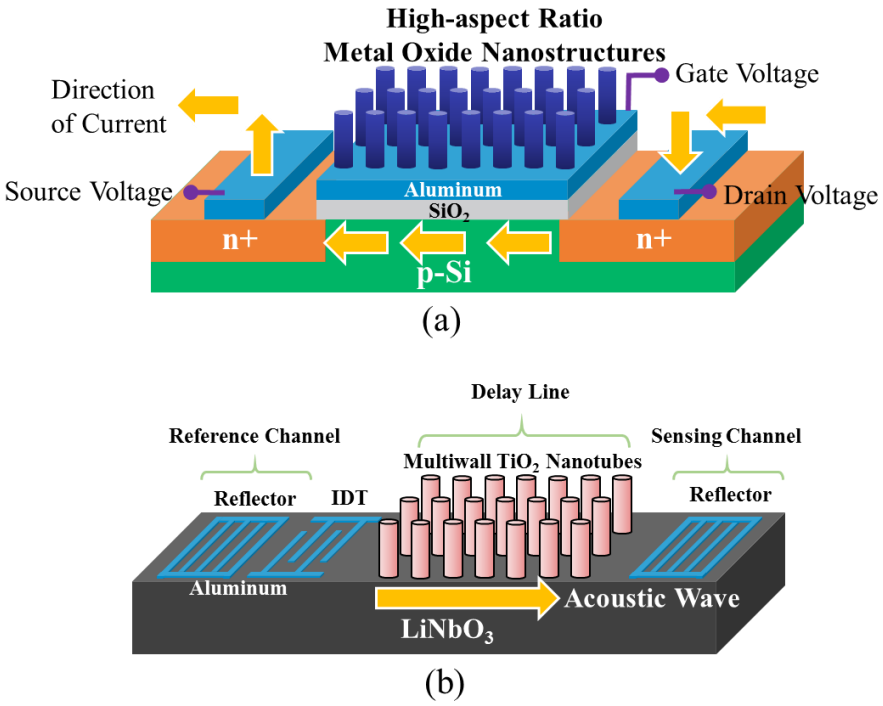

FIG. 2.12. Description of components of (a) ChemFET and (b) OFC SAW gas sensor.

The ultimate goal of our work is to demonstrate a versatile fabrication sensor technology that could be integrated with more complex CMOS and SAW technology devices for portable and mobile sensing applications. The following sections will explain the fabrication process development.

Chapter 3 Process Development & Sensor Fabrication

ZnO nanowires were fabricated on top of the gate of a MOSFET transistor. The temperature of the different fabrication steps ranged from 24°C to 200°C. Higher temperatures fabrication steps would change the diffusion profile in the transistor. Therefore, a low temperature nanowire assembly is ideal for the fabrication of the gas sensor. The fabrication of ZnO nanowires used a combination of aluminum deposition, aluminum anodization, chemical wet etching, dry etching, and ZnO atomic layer deposition. The overall fabrication process is outlined in Fig. 3.1(a) – Fig. 3.1(d), where each figure shows a schematic cross section of the process, as well as a scanning electron micrograph (SEM) of both the cross section and top view of the structures. The initial step is a unique and selective multistep anodization of the e-beam evaporated aluminum film (Fig. 3.1(a)), which shows the AAO template nanopores. This is followed by a low-temperature ZnO deposition using atomic layer deposition (ALD), which proceeds up and over the top of the nanopores, as shown in Fig. 3.1(b). Fig. 3.1(c) shows the filled nanopore structure after the ZnO over layer is removed. Fig. 3.1(d) shows the ZnO nanowires after the selective removal of the AAO template. The result is freestanding ZnO nanowires attached to the top of an aluminum gate of the MOSFET to form an integrated ChemFET sensor.

The process is selective so that the aluminum film can be used for the source and drain contacts of the transistor, since these regions are not anodized. While the process has been developed using ZnO and a MOSFET structure, the selectively formed AAO template could be used to form other types of nanowires, with a suitable deposition process, as well as being integrated with other microelectronic device structures that can incorporate an

aluminum film deposition. The following section will explain the most important fabrication steps to produce a high aspect ratio ZnO nanowires on a gate of a MOSFET.

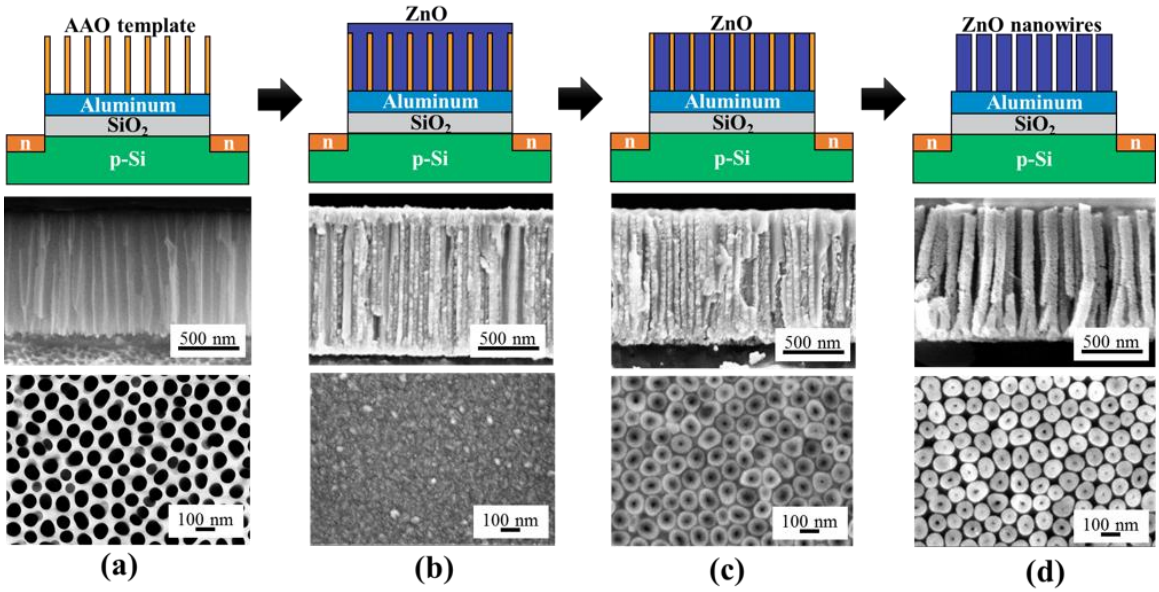

FIG. 3.1. Sketch, plan-views and cross-sectional SEM images of fabrication steps of free standing ZnO nanowires on a gate of MOSFET. a) Empty AAO template after barrier removal step anodization. b) AAO template filled with ZnO by ALD. c) ZnO over layer removed b by sputtering plasma etching. d) Nanowire release using a buffered NaOH pH 11 solution.

3.1. AAO Template Fabrication

Traditional AAO template fabrication on free-standing films requires electropolishing to form an ultra-smooth surface that is conducive to high-density, self-assembled pore formation. The low-temperature, integrated AAO template process therefore requires an ultra-smooth deposited aluminum film in order to eliminate the need for the electropolishing step. For the current process, the initial silicon substrate consisted of a standard <100> prime silicon wafer. The silicon wafer was then oxidized in an O_2 ambient to form a 900Å thick layer of SiO_2. An ultra-smooth 2.5 µm thick aluminum film was deposited onto the wafer using electron beam evaporator at a deposition rate of 2 Å

/sec. The average roughness of the aluminum layer was measured with the Wyko interferometer and was typically found to be in the range of r_a=1.4 – 1.5 nm.

The anodization of the aluminum film was conducted in 3% oxalic acid at 40V in a custom made flat cell using the aluminum coated silicon wafer as the anode and a platinum mesh as the cathode at room temperature, as shown in Fig. 3.2. After a single step anodization, the alumina membrane did not achieve high uniformity pores. Fig. 3.3(a) shows a SEM image of the aluminum film after a 3 minute single anodization step. Highly uniform surface was absolutely necessary in order to achieve a highly ordered nanowires on the gate of the MOSFET. Masuda *et al*, have proven that a multi-step aluminum anodization helps to obtain nanaporous alumina with high uniformity [69]. That fabrication process requires a three step anodization technique with subsequent alumina etch using a chromic/phosphoric acid solution (0.2 wt% H_2CrO_4 /0.4 wt.% H_3PO_4) after each anodization. The usual multistep anodization process is usually done on an aluminum foil that requires one 5-10min long first anodization process, then a second 10-12 hour anodization, and lastly a 10 minute anodization step. Nevertheless, in our case long anodization steps could not be achieved due to limited thickness of the aluminum film. An optimized multi-step anodization was developed specifically for an aluminum layer on a silicon wafer. It was calculated that the total anodization time could not exceed 10 minutes for a 2.5 μm aluminum film. After several experimental runs, it was concluded that 3 minutes for the first two anodization steps then a 5 minute anodization was enough to fabricate highly ordered porous templates, as shown in Fig. 3.3(b).

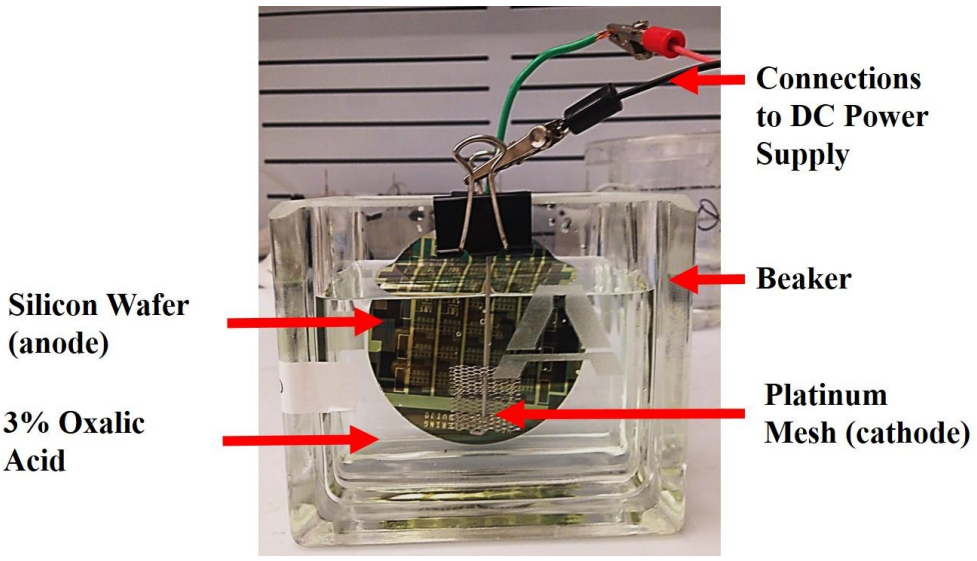

FIG. 3.2. Custom made flat cell for aluminum anodization of a silicon wafer.

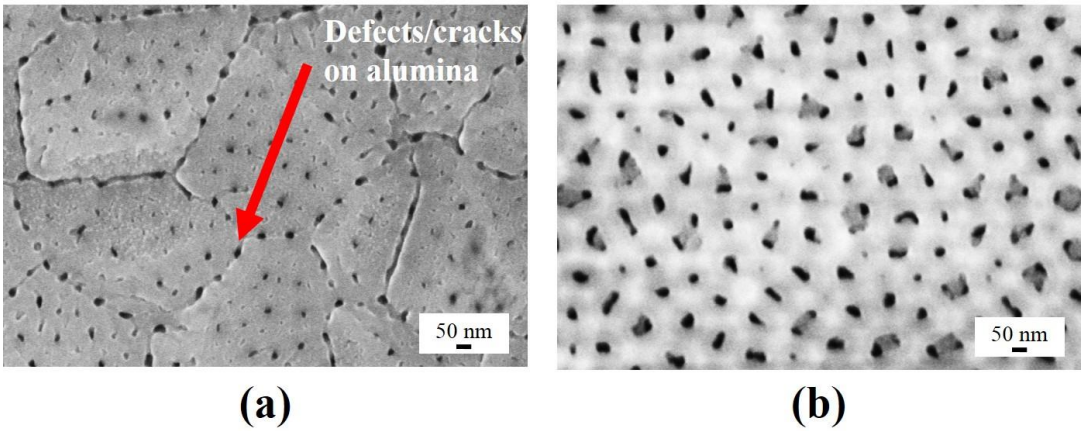

FIG. 3.3. Alumina top view SEM images. a) Single anodization with defects on alumina film. b) Defect free alumina film by multi-step aluminum anodization.

Etching of the barrier layer at the bottom of the pores is necessary to have direct contact between ZnO nanowire and metal gate of MOSFET. Fig. 3.4 (a) shows a thick barrier layer at the bottom of the pores after the multi step anodization. A multi-step barrier layer removal process, based on a process first develop by Ferdeux, *et. al.*[89], was optimized. This gradually voltage reduction process was adapted during the 3rd

anodization step. Fig. 3.4(b)-(d) show cross sectional SEM images of the process optimization. During the first stage of the process the majority of the alumina film growths. The second stage is a reduction of the anodization. This forms ramification at the bottom of the pores. The goal of this process is to leave a thin alumina layer that could be easily etch with 5% phosphoric acid.

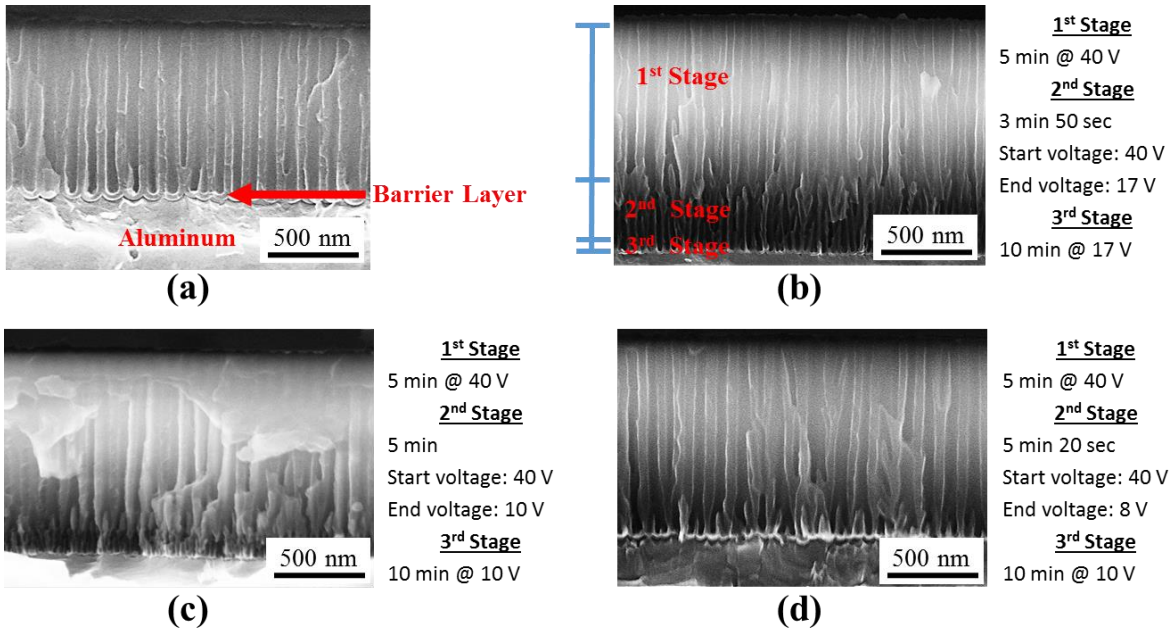

FIG. 3.4. Barrier layer removal by optimization of gradual voltage reduction process. (a) Alumina barrier layer at bottom of pores after 3rd anodization. (b)-(d) Optimization of reduction of ramification at bottom by changing anodization condition during 2nd stage.

The final anodization conditions and current characteristics are shown in Table 3.1 and Fig. 3.5 respectively. The constant voltage Stage 1 results in the self-assembled formation of a nanopore array of approximately 20-40 nm diameter in a dense array that proceeds nearly vertically for 1 µm (Fig 3.6(a)). Note that approximately 0.6 µm of the aluminum film is removed in this stage. This anodization step proceeds nearly vertically into the aluminum film, forming vertical alumina nanopores, but also leaves a layer of

anodized alumina at the bottom of the pores. For the present application in which it is desired to form ZnO nanowires in contact with the underlying aluminum gate of a standard silicon MOSFET, it is important to remove this underlying barrier layer.

Stage	Voltage	Time
1	40 V	5 min
2	40 V to 9V @ 0.1 V/sec	5 min, 10 sec
3	9 V	10 min

Table 3.1. Final anodization conditions.

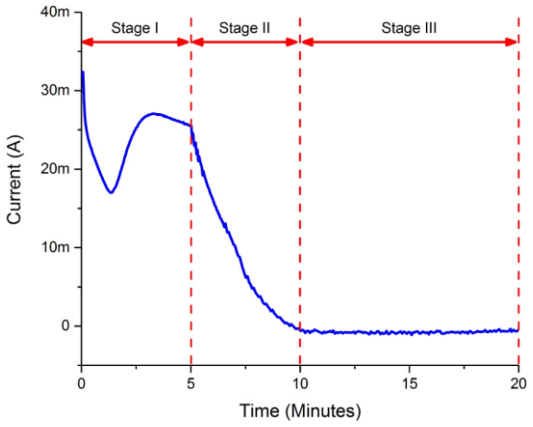

FIG. 3.5. Time Vs. current characteristics of final anodization conditions for barrier layer removal process.

In order to remove some of the irregularities and improve the overall uniformity after the barrier layer removal anodization, the nanopores were further subjected to a final 90 minute alumina wet etch in 5% phosphoric acid at room temperature. This process also increases the diameter of the nanopores from ~30 nm to ~90 nm and helps removing the very thin alumina barrier layer at the bottom of the pores created from the 3-stage anodization process, as can be seen in Fig. 3.6(b). Compared with Fig. 3.6(a), one can also see that the barrier layer has been removed at the bottom of the pores in Fig. 3.6(b). The resulting nanopores are ~90 nm in diameter and 1 μm in height (aspect ratio ~11). The close packed nanopore array has an aerial density of ~ 1.3×10^{10} nanopores/cm^2.

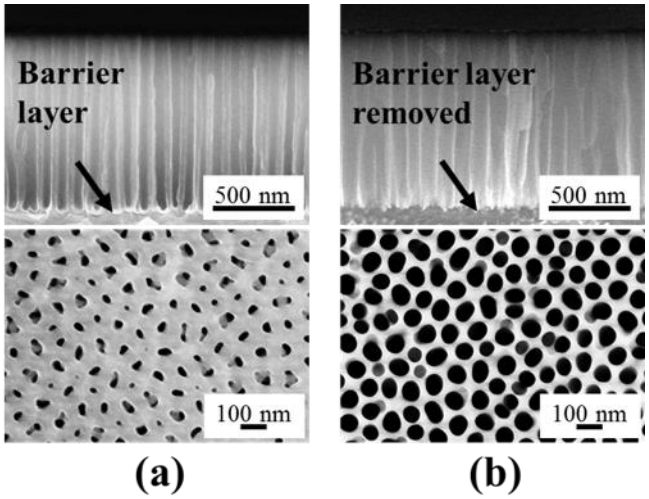

FIG. 3.6. Cross-sectional and top view SEM images of nanopore formation on integrated aluminum films (a) nanopores after the 3-stage anodization process, (b) after enlargement in phosphoric acid showing barrier layer removal at the bottom of the pores.

As shown in Fig. 3.7 (a) and Fig. 3.7 (b), successful DC electroplating of nickel and zinc was clear evidence that the alumina barrier layer at the bottom of the pores was etched a way completely. Even though Ni and Zn was successfully deposited inside the pores by DC electroplating, it just filled about 20% percent of the pores across the sample due to the random natural process of electroplating and there was not a good way to control the filling process.

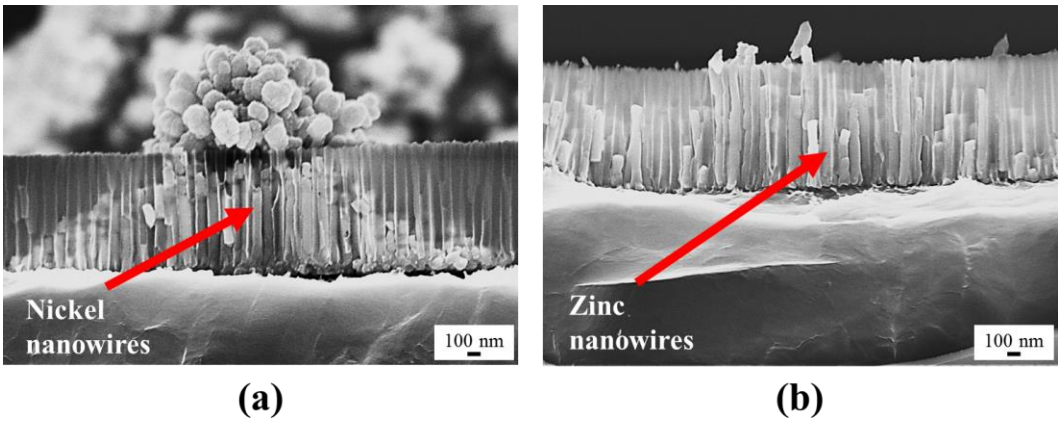

FIG. 3.7. Cross section SEM images of AAO templates without barrier layer. a) AAO template filled with nickel. b) AAO template filled with zinc.

3.2. ZnO Nanowire Fabrication

In order to demonstrate the utility of this novel selective and low-temperature nanowire fabrication process, the AAO template was used to form freestanding ZnO nanowires. The AAO template was filled with polycrystalline ZnO using a Savanna 100 Atomic layer deposition (ALD) machine using a precursor of diethylzinc (DEZ) and DI water. The duration of the DEZ and DI pulses were both 20 ms. Additionally, there was a 8 sec N2 purge after the DI water pulse and a 20 sec purge after the DEZ pulse. The temperature of the ALD chamber was set to 200ºC. Typical of the ALD process, the ZnO deposition was very conformal and entirely filled the nanopores. Notably, the deposition begins on the sidewalls and proceeds inward towards the center. An ALD deposition with 800 pulses resulted in completely filled pores and a 200 nm ZnO over layer on top of the AAO template as shown in Fig. 3.8(a)-(b). The fact that the deposition begins from the outside of the nanowire suggests the possibility that this technique can also be used to form ZnO nanotubes, by limiting the number of pulses to only partially fill the nanopores.

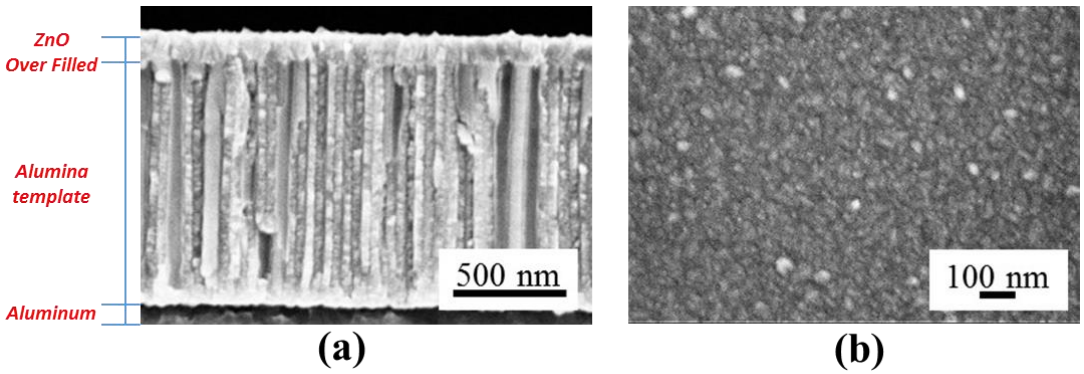

FIG. 3.8. SEM images of ZnO ALD. a) Cross section of AAO filled with ZnO with a 200 nm over layer. b)Top view of ZnO overlayer.

In order to create free standing ZnO nanowires for sensor applications, both the overlying ZnO layer and AAO template need to be removed. As shown in Fig. 3.8 (a) and Fig. 3.8 (b), an excess thin layer of ZnO was left out at the top of the AAO template. ZnO over layer etch was first necessary prior the removal of the AAO template. Fig. 3.9 (a) shows the ZnO sample etched with the HCl and DI water solution after 55 minutes. ZnO over layer wet etch was not conformal across the sample surface. As shown in Fig. 3.9 (a) the top of the pores were still slightly covered with ZnO. ZnO plasma sputtering etch was optimized to remove the ZnO overlayer. The 200 nm ZnO over layer was then removed by sputtering in an Ar plasma using Ar gas at 300 W for 25 minutes in a Plasmalab 80 Plus, with a ZnO etch rate of ~ 13 nm/min. This process reveals the top of the AAO template (Fig. 3.9(b)) allowing for the subsequent nanowire release step.

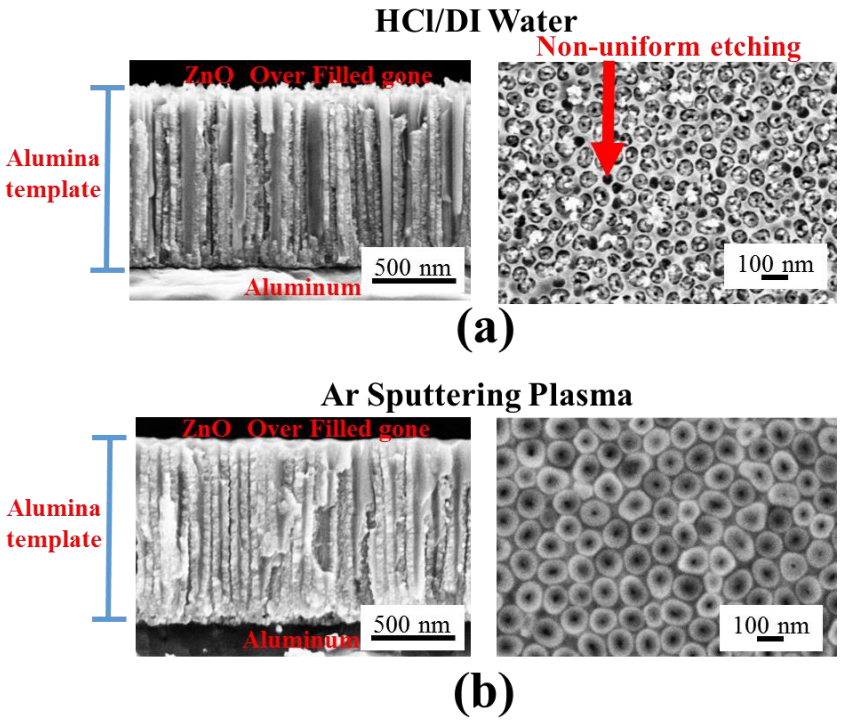

FIG. 3.9. Cross section and top view SEM images of ZnO over layer etch. (a) Wet ZnO over layer etch. (b) ZnO over layer etch by argon sputtering plasma etch

3.3. ZnO Nanowire Release

In order to release the ZnO nanowires, a selective etch is required that removes the AAO template without impacting the ZnO nanowires themselves. The chromic-phosphoric acid solution used previously to etch and enlarge the pores, standard buffered oxide etch (BOE), 2.4% sodium hydroxide, and 0.5% potassium hydroxide solution were tried but suffered from low selectivity between the alumina template and the ALD ZnO nanowires. Fig. 3.10(a) shows the alumina template completely etched way but none of the ZnO nanowires survived using 2.4% NaOH. Fig. 3.10(b) shows etching of the AAO template using 0.5% KOH. Even though the AAO template was successfully removed with 0.5% KOH, the nanowires suffered serious damaged due to low etch selectivity leaving spontaneous formation of ZnO crystals on top of the nanowires.

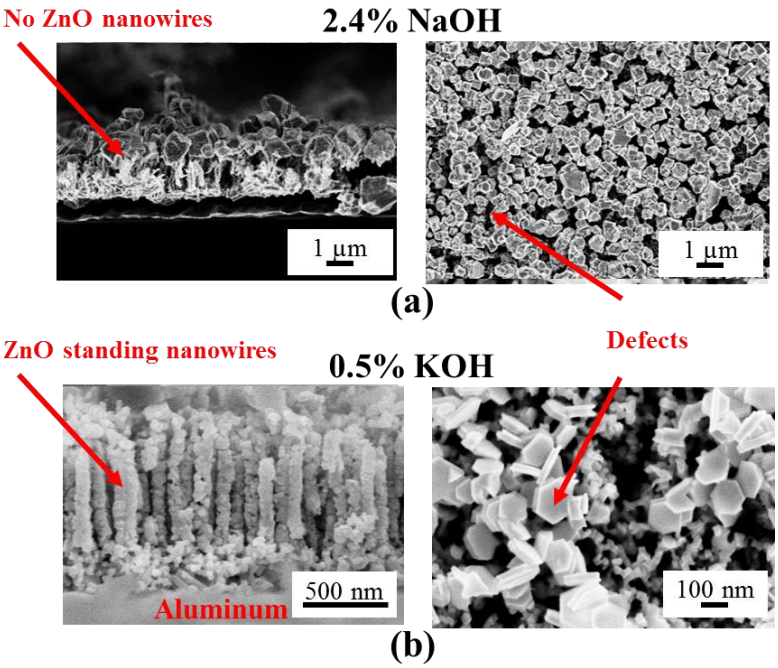

FIG. 3.10. Cross section and top view SEM images of low selectivity nanowire release wet etch. (a) AAO template etch with 2.4% NaOH. (b) AAO template etch with 0.5% KOH.

Thermodynamic modeling has shown previously that a buffered pH 11 NaOH solution will successfully remove AAO without degrading the ZnO surface of the nanowires [71]. This thermodynamic model shows that the maximum solubility of crystalline ZnO is at ph below 9.2 and above pH 11.5. In other words, chemical solutions that have pH level lower than 9.2 and higher than 11.5 will partially etch and degrade the ZnO surface. Using this approach, a buffered solution of pH 11 NaOH (50 ml of 0.05 M NaHCO3, 23 ml of 0.1 M NaOH, and 27 ml of DI water) was used to selectively remove the AAO template. After several experiments, it turned out that the buffer solution required constant stirring during the etching of the alumina template for optimum etching and to maintain a more constant pH. Fig. 3.11 (a) shows defect formation on top of the ZnO nanowires by etching the template with the pH 11 buffer solution for 4 days without magnetic stirring. To solve these challenges, a Teflon basket was used to rise the sample up in a beaker while using a magnetic stirring capsule at the bottom of the beaker. The resulting released nanowires are shown in Fig. 3.11(b), which shows high aspect ratio (~10:1) ZnO nanowires standing on the aluminum surface.

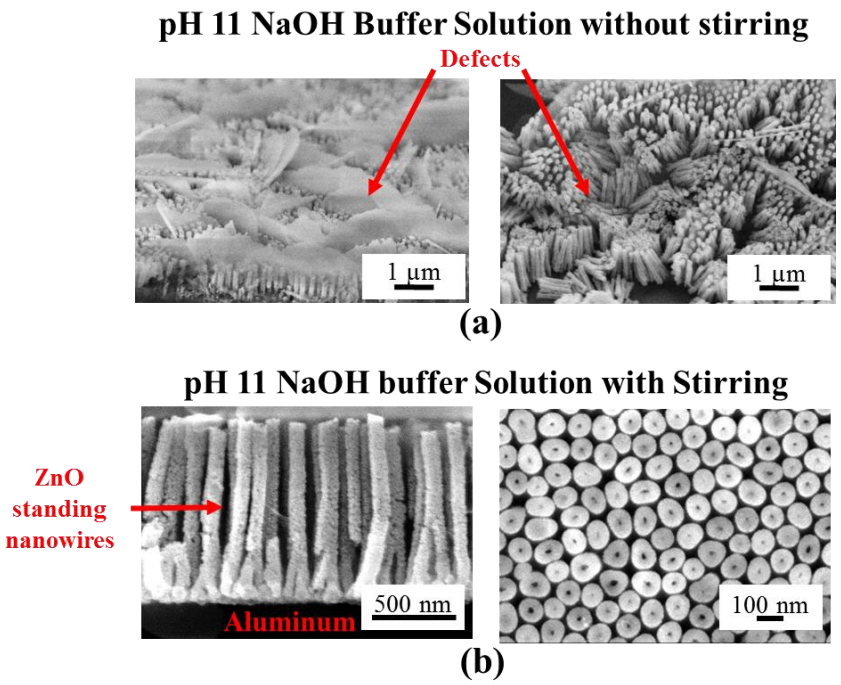

FIG. 3.11. Top and cross section SEM images of AAO template etch optimization. (a) Defects of top of ZnO nanowires using pH 11 NaOH buffer solution without magnetic stirring. (b) Resulting standing ZnO nanowires using pH 11 NaOH buffer solution with magnetic stirring

3.4. Characterization of ZnO Nanowires

The freestanding ZnO nanowires were analyzed using a Zeiss Auriga FIB-SEM equipped with an energy-dispersive X-ray spectroscopy (EDX) system to evaluate the chemical composition from a nanowire cross-section to make sure that the AAO template was completely etch away. Fig. 3.12 shows the EDX measurement that displays three main peaks coming from Carbon K_a = 0.277 keV, Oxygen K_a = 0.525 keV, and Zinc L_a= 1.012 keV. In the other hand, the EDX measurement also shows very small peaks coming from Silicon Ka=1.755 keV and Aluminum K_a=1.486 keV peaks due to the size of electron beam diameter. Elemental chemical quantification was also obtained showing main three atomic

percentages from Carbon 12.80%, Oxygen 42.35%, and Zinc 43.67% implying that the nanowires are made of highly pure ZnO with a ~1:1 Zn:O composition.

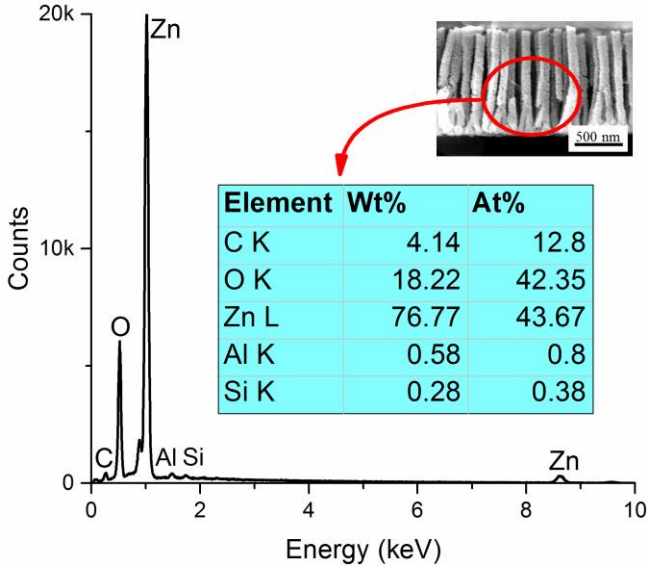

FIG. 3.12. EDX measurement of ZnO nanowires of 90 nm in diameter and 1 μm in height. The Spectra is taken from the indicated location on the inset cross-section SEM of the ZnO nanowires.

The nanowires were further investigated by TEM using Zeiss Libra 120. Fig. 3.13(a) shows a TEM cross section image of the AAO template filled with ZnO on a MOS structure prepared by FIB lift-out method. Fig. 3.13(a) shows the diameter of the nanowires to be ~89.56 nm which confirms the measurement from the SEM images. The nanowire also exhibit a small gap in the center of the nanopores with a diameter of ~ 3-7 nm. This is due to the fact that the highly conformal ALD deposition process fill the AAO template starting from the outside sidewall of the nanopores. The ALD process appears to close off the top of the nanopores just prior to some of them being completely filled in. Note that this is not an issue in the present sensor type applications and in fact, would only result in

additional surface area on the inside of the nanowires. With careful optimization, it appears that nanotubes could be fabricated with this technique to take advantage of this effect.

The image contrast in Fig. 3.13(a) also indicates that the different grain orientations, suggesting a polycrystalline structure nature of the ZnO nanowire. Fig. 3.13(b) shows the selected area electron diffraction pattern of region highlighted with the dotted circle in Fig. 3.13(a), which by indexing, corresponds to a wurtzite type ZnO structure. ZnO nanowires show diffraction generated from the (100), (002), (101), (102), (110), (103), and (200) planes as shown in Fig. 3.13(b). The ring patterns of the diffraction spectra revealed that the ZnO nanowires are indeed polycrystalline.

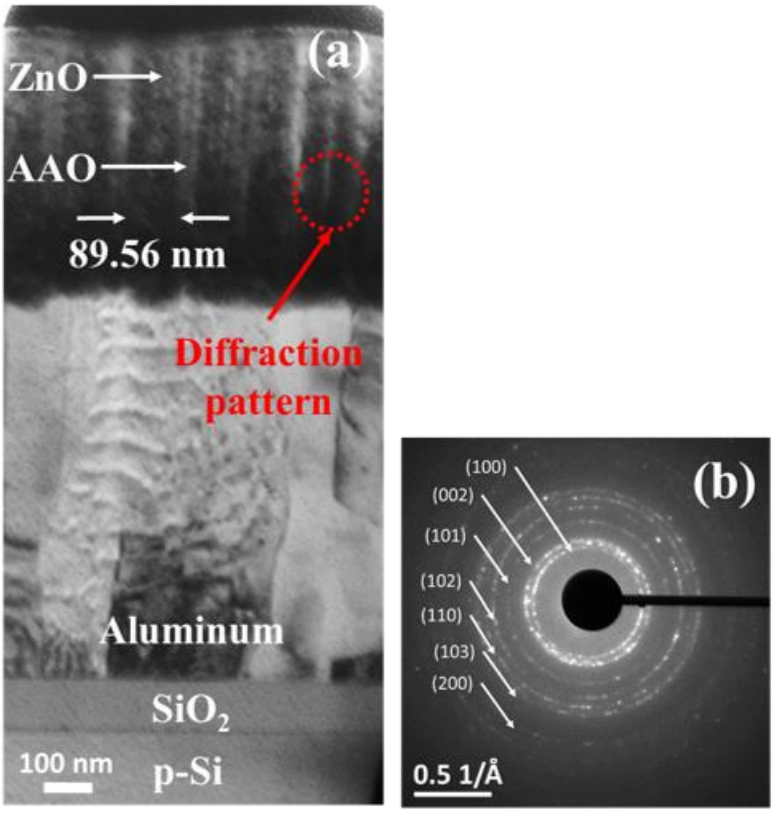

FIG. 3.13. (a) Cross-sectional TEM images of AAO template filled with ZnO. (b) Diffraction patterns of selected area in (a).

3.5. TiO_2 Nanowire Fabrication

Empty pores of about 1μm in height and 100 nm width were fabricated by the combination of the multistep anodization and barrier layer removal process on top the gate of a MOSFET described previously in Section 3.1. These pores could be filled by a variety of metal oxide materials through ALD. High aspect ratio, very conformal, and uniform deposition has been demonstrated with ALD. There are common ALD materials that could be used to fill the pores such as SnO_2, and TiO_2. We have optimized the same ZnO nanowire fabrication process to fabricate TiO_2 nanowires. The overall TiO_2 nanowire fabrication sequence is shown in Figs. 3.14(a)-(d).

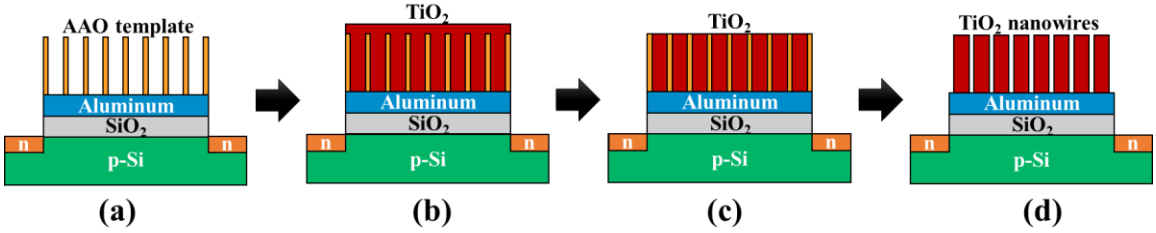

FIG. 3.14. Sketch of fabrication steps of free standing TiO_2 nanowires on a gate of MOSFET. a) Empty AAO template after barrier removal step anodization. b) AAO template filled with TiO_2 by ALD. c) TiO_2 over layer removed by sputtering plasma etching. d) Nanowire release using a chromic/phosphoric acid solution.

The AAO template was fabricated using the multistep aluminum anodization, barrier layer removal aluminum anodization, and 90 min pore enlargement in 5% H_3PO_4 (Figs. 3.15(a)-(b)). Compared with the ZnO nanowires fabrication process described in Sections 3.1-3.3, TiO_2 nanowire fabrication required a change of the ALD precursor from DEZ to TDMAT (Tetrakis (dimethylamido) titanium). The duration of the TDMAT pulse was 0.1 sec while the DI pulse was 0.015 sec. Additionally, there was a 10 sec N_2 purge after the DI water and TDMAT pulse. The temperature of the ALD chamber was set to

200ºC. Fig. 3.15(c)-(d) show the AAO template filled with TiO_2 leaving a 43 nm TiO_2 over filled layer on top after 1000 pulses.

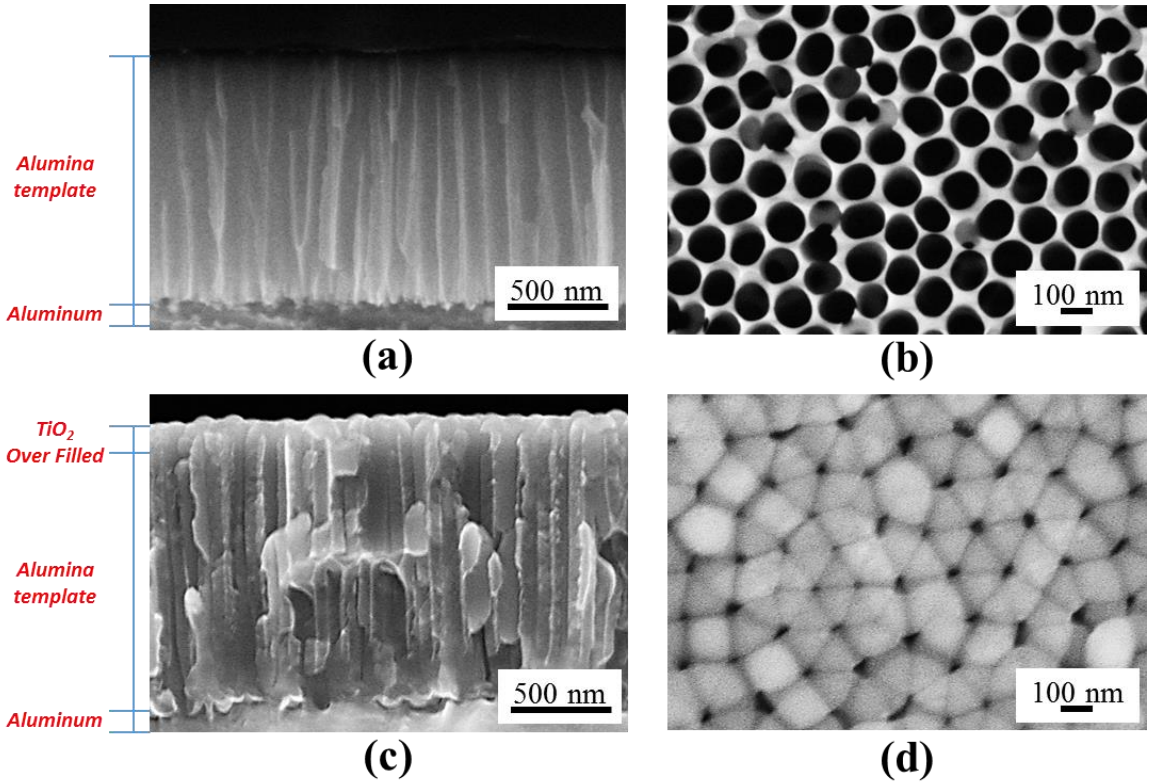

FIG. 3.15. Cross section and top view SEM Images of AAO template. (a) Empty alumina template. (b) Alumina template filled TiO_2 by ALD.

Etching of the 43 nm TiO_2 over layer was achieved using Ar sputtering plasma at 300 W for 22 minutes, with a TiO_2 etch rate of ~ 2 nm/min. As shown in Fig. 3.16 (a)-(b), this process reveals the top of the AAO template allowing the subsequent nanowire release step.

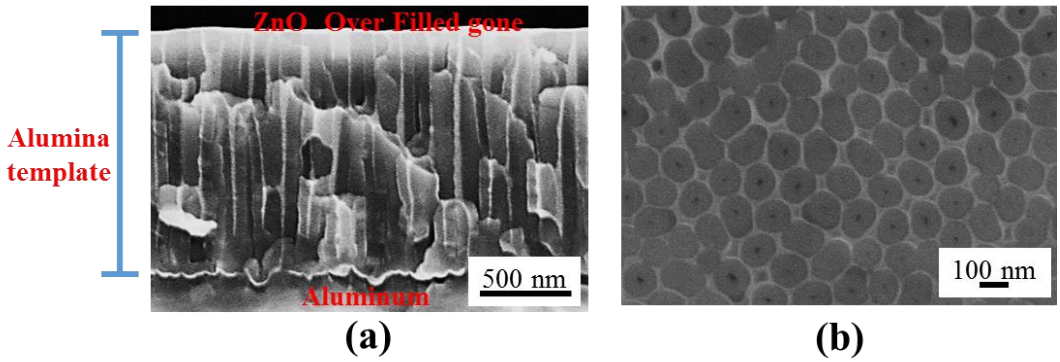

FIG. 3.16. Cross section and top view SEM images of ZnO over layer etch. (a) Wet ZnO over layer etch. (b) ZnO over layer etch by argon sputtering plasma etch

3.6. TiO_2 Nanowire Release

The AAO template was etched away using the chromic/phosphoric acid solution (0.2 wt% H_2CrO_4 /0.4 wt.% H_3PO_4) previously used during the multistep aluminum anodization process. Fig. 3.17(a)-(b) show complete etch of the AAO template using the chromic/phosphoric acid for 11 hours at 70°C. Note that this etching solution does not degrade the TiO_2 nanowire surface nor leaves defects on top of the nanowires. The resulting aerial TiO_2 nanowire density, same as the ZnO nanowires, was 13 billion nanowires/cm^2, incrementing the reactive surface area by 38X compared with a TiO_2 thin film.

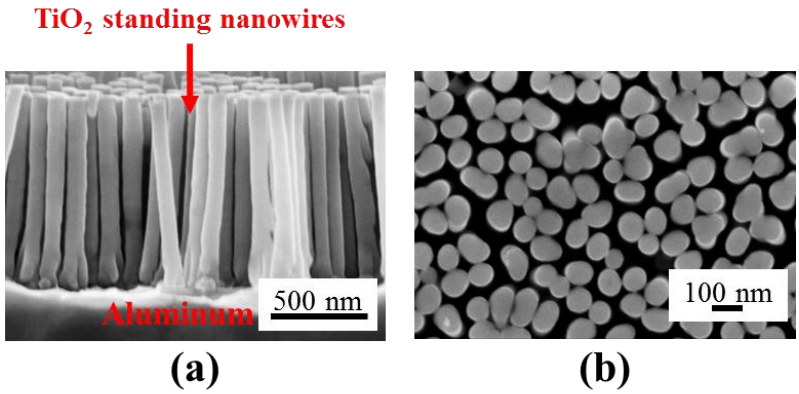

FIG. 3.17. SEM images of standing TiO2 nanowires on aluminum film. (a) Cross section view. (b) Top view.

3.7. Characterization of TiO_2 Nanowires

The TiO_2 nanowires were investigated by TEM. For sample preparation, silicon wafer samples with the TiO_2 nanowires were subject to 1M NaOH for 2 hours at room temperature for aluminum under layer etch (lift-off). Once TiO_2 nanowires were release freely from the aluminum layer, then TEM samples were prepared by drop casting method. Fig. 3.18(a) shows the diameter of the nanowires to be ~72.77 nm and a small gap in the center of the nanowire of ~5-10 nm. High deposition conformability fills the AAO template starting from the sidewall of the nanopores. The image contrast in Fig. 3.18(a) also indicates that the different grain orientations, suggesting a polycrystalline structure nature of the TiO_2 nanowire. Fig. 3.18(b) shows the selected area electron diffraction pattern of region highlighted with the dotted square in Fig. 3.18(a), which by indexing, corresponds to an anatase type TiO_2 structure. The TiO_2 nanowire shows diffraction generated from the (101), (103), (200), (211), (204), and (116) planes, as shown in Fig. 3.18(b). The ring patterns of the diffraction spectra revealed that the TiO_2 nanowires are indeed polycrystalline.

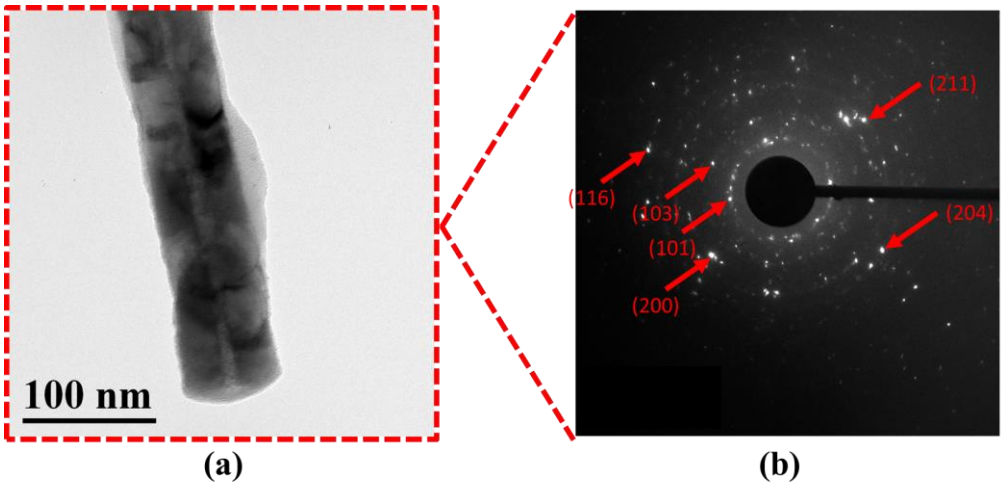

FIG. 3.18. (a) TEM image of TiO_2 nanowire. (b) Diffraction pattern of selected area in (a).

Hall measurements were used for electrical characterization of the ALD TiO_2 film using the van der Pauw method. The Hall Effect was measured using a Versalab system (Quantum Design) at room temperature, sweeping the magnetic field from -3 to 3 T to identify the type of majority carriers. The Hall measurement setup configuration is shown in the inset in Fig. 3.19 with the positive magnetic field direction as marked. From the setup configuration, the positive slope of Hall resistance (R_{Hall}) vs. magnetic field (B) in Fig. 3.19 indicates that holes are the majority of the carriers in the TiO_2 thin film. The DC conductivity was also measured to calculate sheet resistivity, carrier density, and mobility at room temperature using the van der Pauw method. The sheet resistivity of a 43 nm ALD TiO_2 film was found to be 0.1189 Ω cm. Drude's model was used, assuming a one band model as a first-order approximation, using the Hall coefficient equation: $R_{Hall} = 1/(p\,e)$ to calculate the carrier density yields the equation:

$$\frac{V_H}{I} = \frac{B}{d(pe)} \tag{3.1}$$

where I = excitation current, B = magnetic flux density directed perpendicular to the sample plane, V_H = Hall voltage, $e = 1.6 \times 10^{-19}$ coulomb, d = film thickness, 43 nm. In other words, from the R_{Hall} vs. B plot in Fig. 7, the carrier density p can be extracted from the slope: $1/(p\,e\,d)$. While the mobility:

$$\mu = \frac{\sigma}{pe} \tag{3.2}$$

was determined from known conductivity σ and carrier density p. From the measurements, the carrier density was found to be 4.170×10^{19} cm^{-3} with the mobility of 1.261 $cm^2/(Vs)$. The p-type nature of the TiO_2 film might be due to the nitrogen-doping which enhances the hole concentration and mobility of TiO_2.

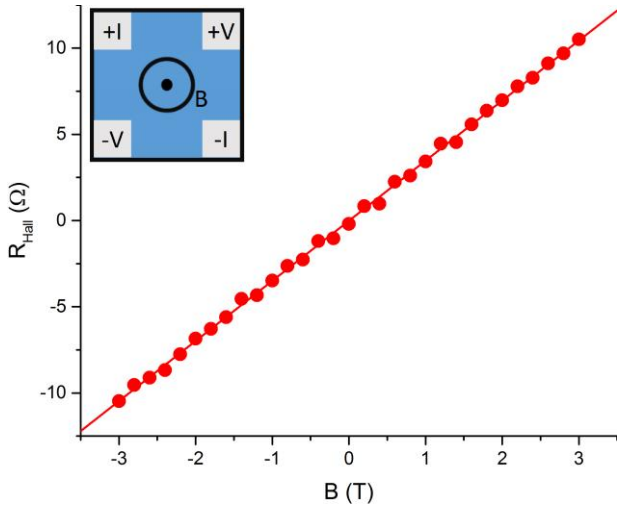

FIG. 3.19. Hall resistance (R_{Hall}) of the ALD TiO_2 film as function of the magnetic field (B) using van der Pauw method with the setup configuration shown in inset (a).

3.8. Multiwall TiO_2 Nanotube Fabrication

Current existing technology in AAO templates have produced single and double-walled nanowires, and nanotubes using other methods of deposition. The diameter of the nanotube, height, and spacing between nanotubes are parameters that are difficult to control with such growth methods. Conformal depositions by ALD can be optimized to produce multiwall nanotubes instead of nanowires. By making multiwall nanotubes the surface area can be expanded ever further. Gu, *et. al* have shown the synthesis of novel highly ordered multiple-walled tube-in-tube nanostructures with up to five nestted coaxial nanotubes embedded in AAO template [71]. Even though that method seems promising for drastic increment of reactive surface area, it has not been reported up to date a ChemFET that uses such method. This nanotube fabrication method has been accomplished on free-standing films. This is due to the fact that traditional methods of fabricating the AAO template generally rely on a thick (>100μm) aluminum film as a starting substrate which requires electropolishing to smooth the surface and make it conducive to self-assembled

hexagonally close-packed pore formation. During the electropolishing the aluminum film removes substantial portion of thickness, typically >20μm. By using conventional aluminum deposition method, such electron beam evaporation, 20 um thick aluminum deposition could be very puzzling.

Expanding the potential of AAO templates by utilizing ALD to create far more complex nanostructures that could increase the surface area in a reactive layer of a ChemFET. Multiwall nanotubes could increase the reactive surface area at least 3X more than nanowires. That improvement could be achieve by making hallow nanotubes instead of nanowires based on our previously reported growth method of ZnO and TiO_2 nanowires. This approach could dramatically improve the reactive surface area from 38x to 112X since the nanowire has only one single side exposed to the reactive gas while the multiwall nanotube has 4 sides. A ChemFET with a better sensibility and faster transient response could be attained with this approach.

The fabrication of multiwall TiO_2 nanotubes use a combination of aluminum deposition, aluminum anodization, TiO_2 and Al_2O_3 ALD, sputtering plasma etching, and wet etching. The schematic drawing of the fabrication of multiwall TiO_2 nanotubes is shown in Figs. 3.20(a)-(d), where each figure shows a schematic cross section of the process. The fabrication process is in sharp contrast with the ZnO nanowire and TiO_2 nanowire fabrication process. However in this case, the AAO template is filled with a sequential trimethylaluminum (TMA), and TDMAT ALD. Table 3.2 shows the ALD recipe used for multiwall TiO_2 nanotubes fabrication at 200°C. Note that the first and third nanotube wall correspond to 293 pulses of TDMAT while the second and fourth wall correspond to 93 TMA pulses each. The resulting structure is shown in Fig. 3.21(a)-(b). In

this case the ALD template is filled with 10 nm TiO_2, 10 nm Al_2O_3, 10 nm TiO_2 and 10 nm Al_2O_3 leaving a 40 nm over layer on top of the AAO template. By controlling the number of ALD pulses, one can choose the thickness of each wall material.

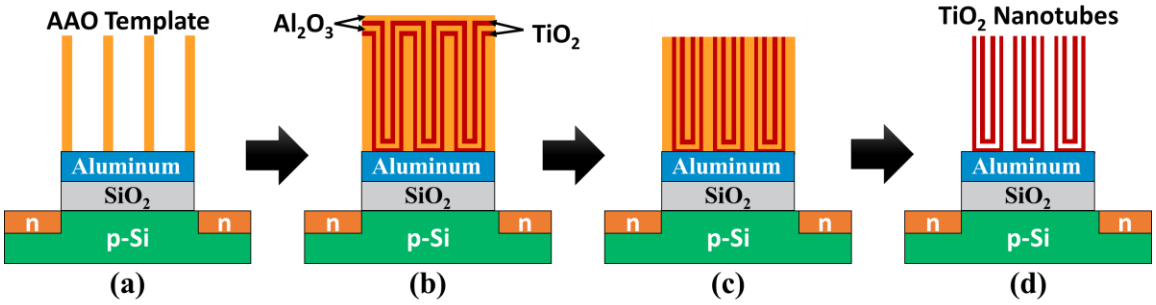

FIG. 3.20. Sketch of fabrication steps of free standing multiwall TiO_2 nanotubes on a gate of MOSFET. a) Empty AAO template after barrier removal step aluminum anodization. b) AAO template filled with TiO_2 and Al_2O_3 by ALD. c) TiO_2/Al_2O_3 over layer removed by sputtering plasma etching. d) Nanowire release using a chromic/phosphoric acid solution.

Wall #	Instruction	Number of Pulses	Resulting Thickness
1	TDMAT 0.1 sec pulse	293	10 nm
	DI water 0.015 sec pulse		
2	TMA 0.015 sec pulse	93	10 nm
	DI water 0.015 sec pulse		
3	TDMAT 0.1 sec pulse	293	10 nm
	DI water 0.015 sec pulse		
4	TMA 0.015 sec pulse	93	10 nm
	DI water 0.015 sec pulse		

Table 3.2. ALD recipe for multiwall TiO_2 nanotubes.

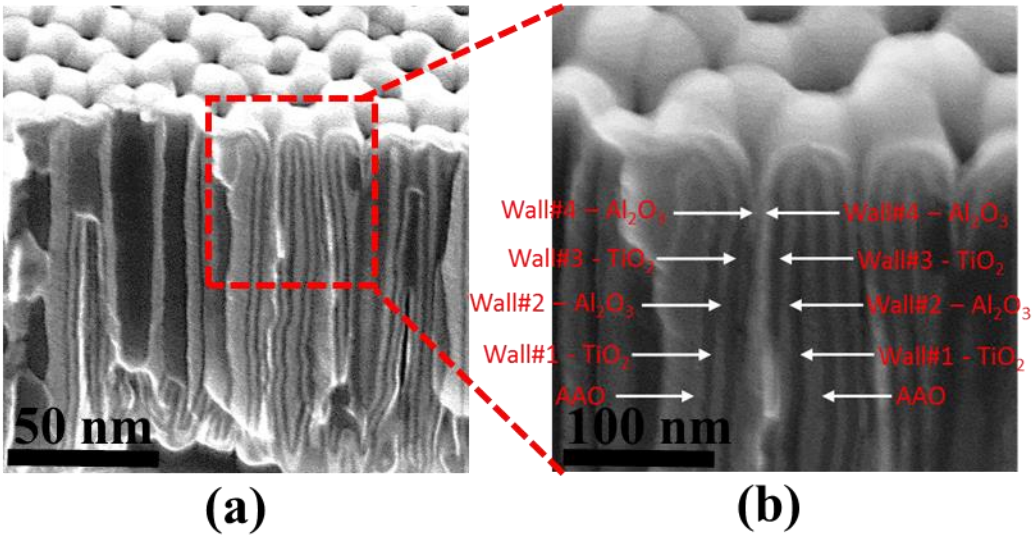

FIG. 3.21. SEM cross section image of AAO template filled with Al_2O_3 and TiO_2. (a) Zoom-out SEM view of AAO template. (b) Zoom-in SEM view of single tube of AAO template filled with 4 ALD walls

Etching of the 40 nm TiO_2/Al_2O_3 over layer was achieved using Ar sputtering plasma at 300 W for 19 minutes, with a TiO_2/Al_2O_3 conjunctional etch rate of ~ 2 nm/min. As shown in Fig. 3.22, this process reveals the top of the AAO template and sacrificial ALD Al_2O_3 walls allowing the subsequent nanotube release step.

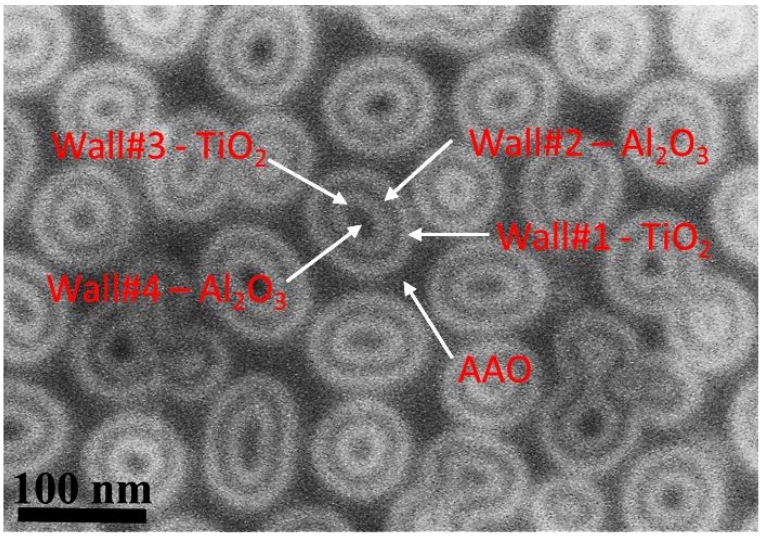

FIG. 3.22. SEM top view of AAO template filled TiO_2 and Al_2O_3 walls after 19 minutes in Ar sputtering plasma etch.

3.9. Multiwall TiO_2 Nanotube Release

Since the AAO template and Al_2O_3 walls are exactly the same material, the same chromic/phosphoric acid solution used in the TiO_2 nanowire release process was used again to release the nanotubes from the template and sacrificial layers. Figs. 3.23(a)-(c) show multiwall TiO_2 nanotubes after etching the AAO template and Al_2O_3 walls for 11 hours in the chromic/phosphoric acid solution at 70°C. Note that the etching solution does not degrade the TiO_2 surface. The resulting layer has 2X the areal density than the TiO_2 & ZnO nanowire film (26 billion nanotubes/cm^2) which results in a 112X increment in surface area compared with a TiO_2 thin film counterpart.

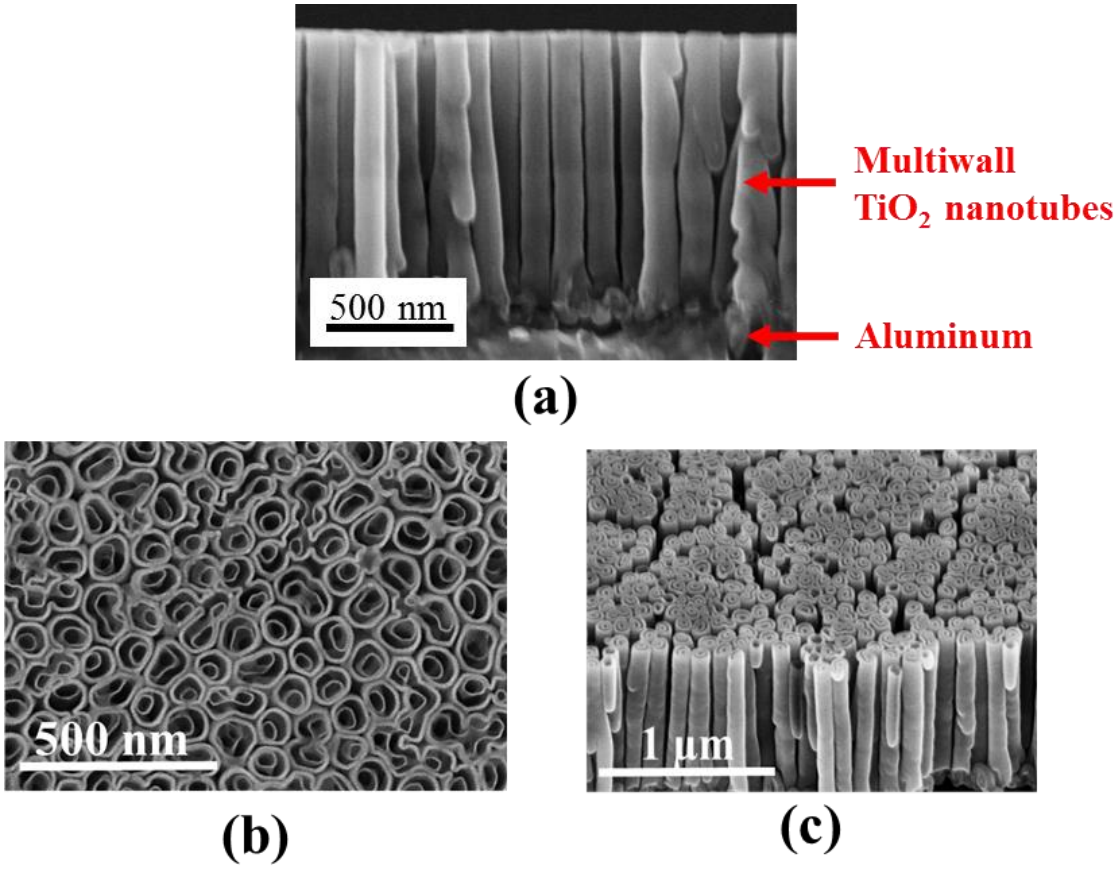

FIG. 3.23. SEM views of multiwall TiO2 nanotubes after AAO and Al_2O_3 etch release. (a) Cross section view. (b) Top view. (c) Tilted view.

3.10. Characterization of Multiwall TiO_2 Nanotubes.

The TiO_2 nanotubes were investigated by TEM using Zeiss Libra 120. For sample preparation, silicon wafer samples with multiwall TiO_2 nanotubes were subject to 1M NaOH for 2 hours at room temperature for aluminum under layer etch (lift-off). Once TiO_2 nanotubes were release freely from the aluminum layer, TEM samples were prepared by drop casting method. Fig. 3.24 shows a TEM image a portion of a multiwall TiO_2 nanotube. Fig. 3.24 shows the diameter of the multiwall nanotube to be ~99.96 nm, wall # 1 and wall # 2 to be ~9.57 nm which confirms the measurement from the SEM images. The multiwall nanotube also exhibits a small gap between nanotube wall #1 and wall #2 of ~10 nm, and a diameter of the inner nanotube of ~41nm. By taking advantage the highly conformal ALD deposition process, one can module the wall thicknesses by changing the ALD pulses of the sacrificial and/or TiO_2 material. With careful optimization, additional surface area could be implemented. The image contrast in Fig. 3.24 also indicates that the different grain orientations, suggesting a polycrystalline structure nature of the multiwall TiO_2 nanotube.

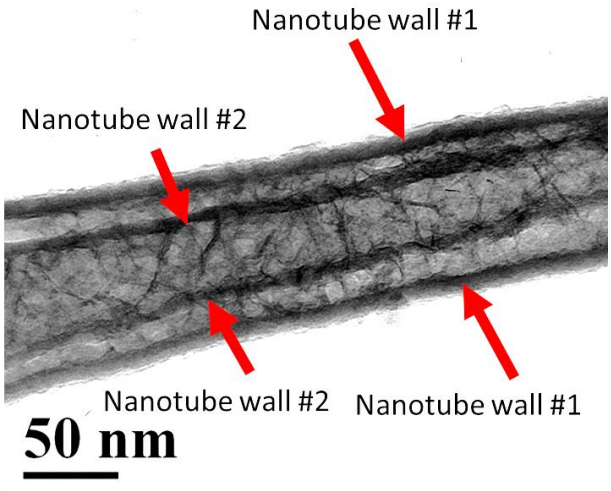

FIG. 3.24. TEM image of a portion of multiwall TiO2 nanotube.

Fig. 3.25(b) shows the selected area electron diffraction pattern of region highlighted with the dotted square in Fig. 3.25(a), which by indexing, corresponds to an anatase type TiO_2 structure. The multiwall TiO_2 nanotube shows diffraction generated from the (101), (004), (200), and (105) planes as shown in Fig. 3.25(b). The ring patterns of the diffraction spectra revealed that the multiwall TiO_2 nanotubes are indeed polycrystalline.

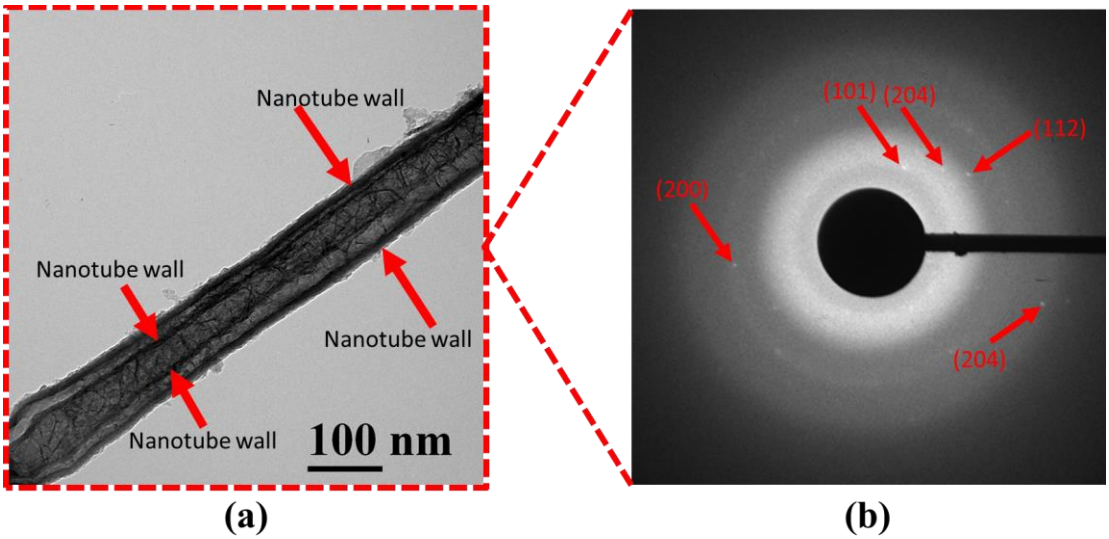

FIG. 3.25. (a) TEM image of a multiwall TiO_2 nanotube. (b) Diffraction pattern of selected area in (a).

3.11. Integration ZnO Nanowires, TiO_2 nanowires and Multiwall TiO_2 Nanotubes to MOSFET

For integration into a MOSFET or other microelectronic device, it is most useful to be able to form nanowires selectively, i.e. form them at the desired locations, but leaving the remaining aluminum film for device structures and interconnects. Because the anodization process requires an applied potential, it is straightforward to pattern the aluminum layer, forming contacts for anodizing only specific regions. As shown in Fig. 3.26, this selectivity can be further enhanced by the addition of a masking layer, such as photoresist, as a protective layer to allow anodization in the desired regions only.

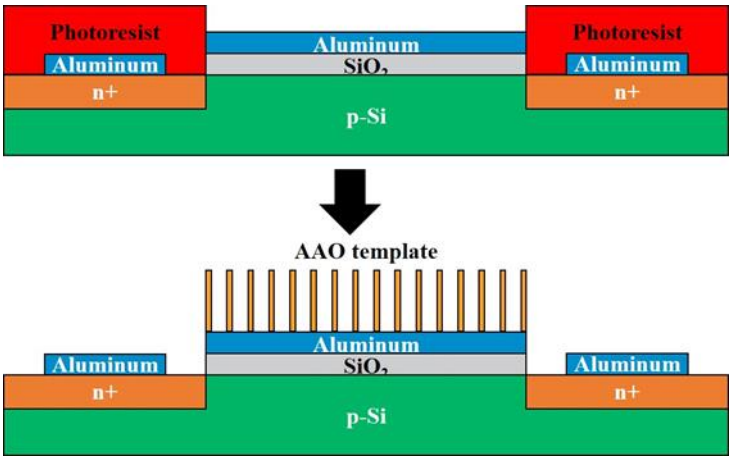

FIG. 3.26. Selective aluminum anodization using photoresist as masking layer leaving anodized and un-anodized regions.

This approach was used to selectively anodize the gates of aluminum gate MOS transistors as shown in Figs. 3.27(a)-(d). The gate regions of these aluminum gate MOSFET devices have been selectively anodized and used to form freestanding ZnO nanowires. One can readily see that only that gates of the transistors have the AAO template and high-aspect ratio ZnO formation, while the remaining aluminum is used for metallization and interconnects of the MOS transistors. Note that in this application the aluminum film is not completely anodized, leaving an underlying aluminum film. By removing the alumina barrier layer at the bottom of the pores, the resulting ZnO nanowires are then in contact with the underlying aluminum layer that acts as the gate of the MOS transistor. As shown in Figs. 3.28(a)-(b), the same fabrication approach was adapted for O_2 nanowire and multiwall TiO_2 nanotube integration to ChemFETs.

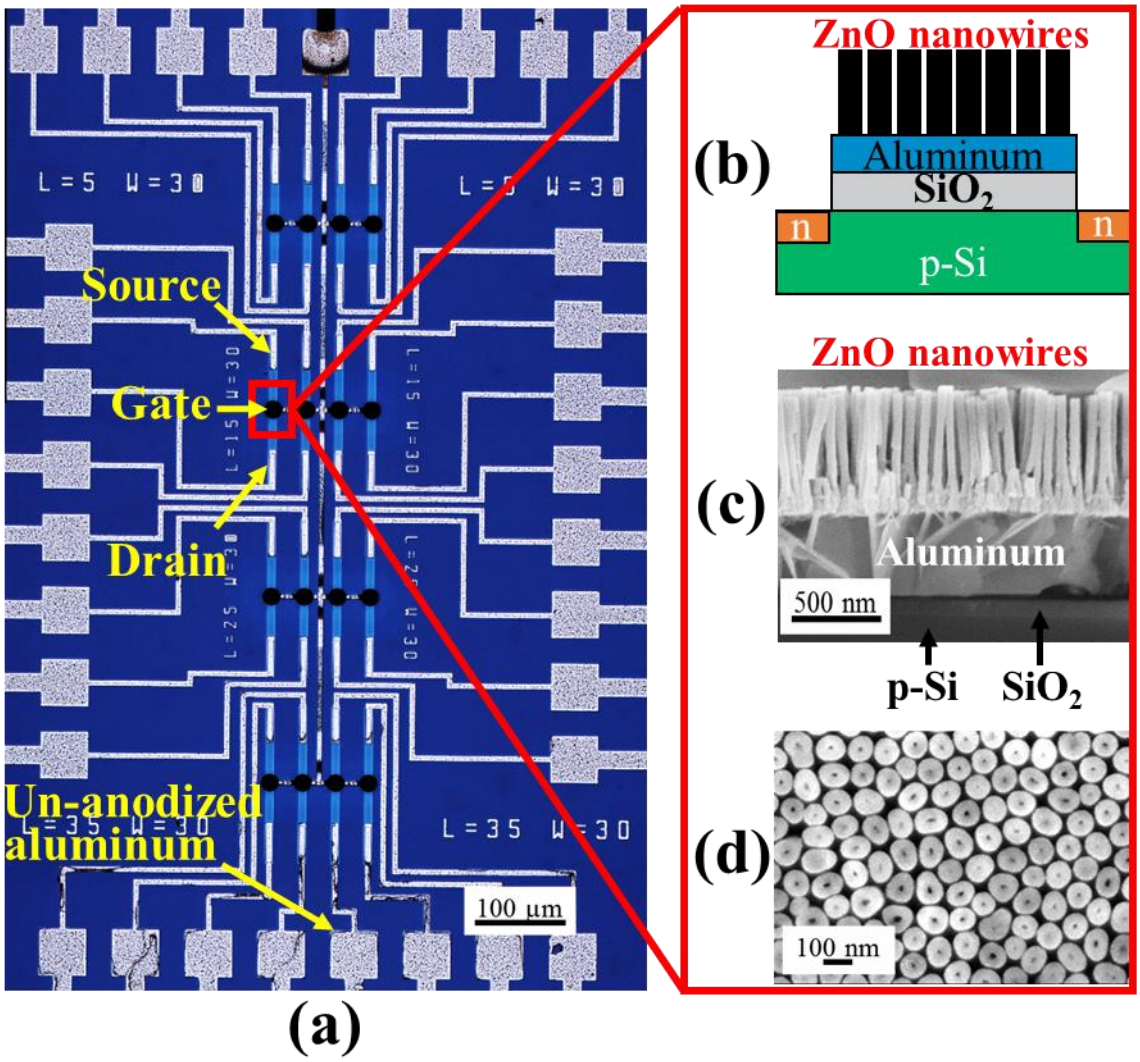

FIG. 3.27. MOSFET chip after ZnO nanowire release. (a) Large optical top-view of selective anodization of aluminum gates MOSFET (black dots). (b) Sketch of ZnO nanowires on gate of MOSFET. (c) Cross-section SEM view of standing ZnO nanowires on gate of MOSFET. (d) Top view of ZnO nanowires.

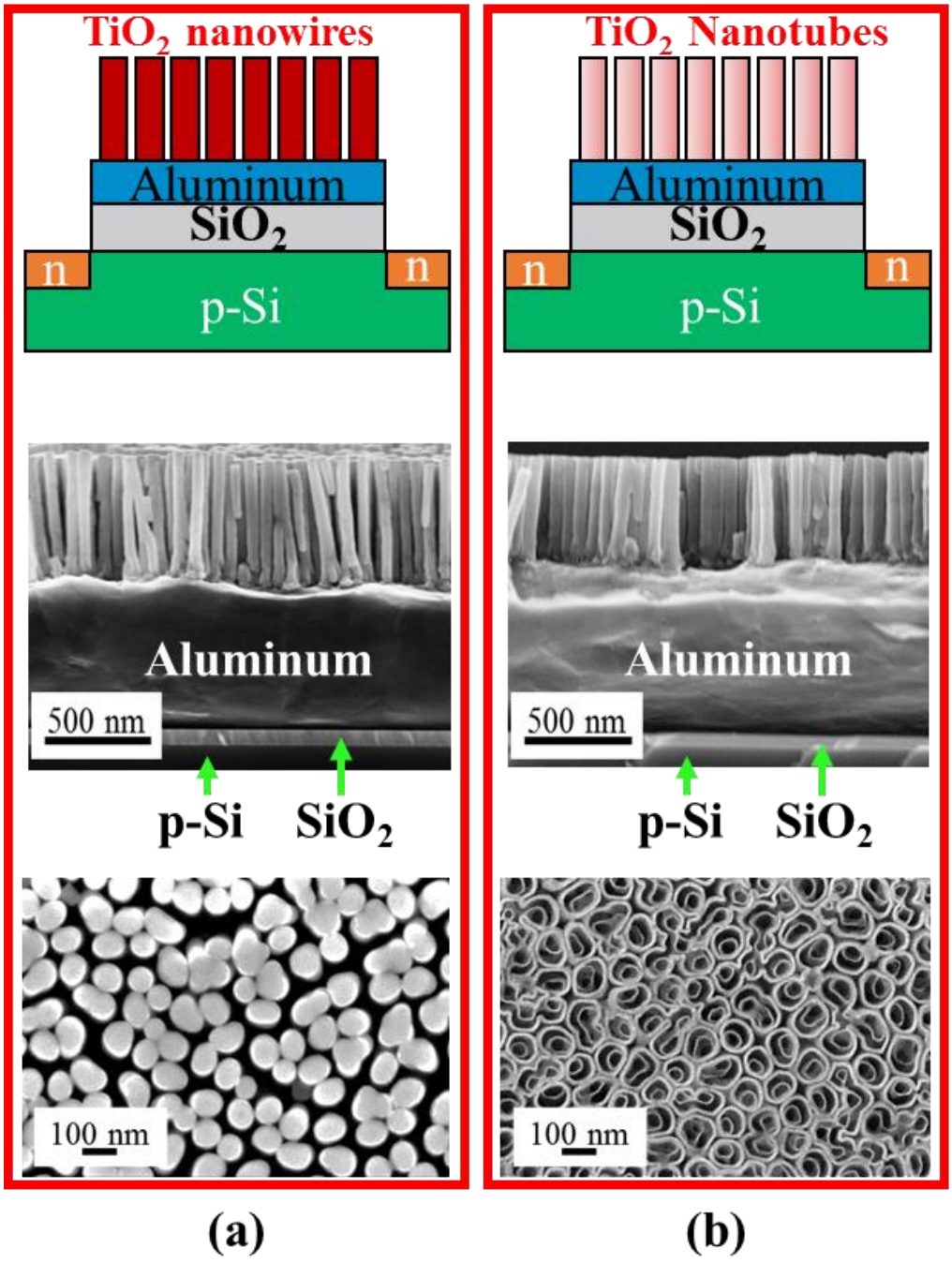

FIG. 3.28. Sketch, plan-views and cross-sectional SEM images of free standing high-aspect ratio metal oxide nanostructures on a gate of MOSFET by selective aluminum anodization. (a) TiO_2 nanowires. (b) Multiwall TiO_2 nanotubes.

Chapter 4 Experimental Setup and Sensor Testing

4.1. Experimental Design

The electrical response of the ChemFET with high-aspect ratio ZnO nanowires, TiO_2 nanowires and multiwall TiO_2 nanotubes on the gate were examined using ammonia gas with concentrations ranging from 25-200 ppm, diluted with synthetic air (20% oxygen and 80% nitrogen). A sketch of the concept of the test is shown in Fig. 4.1. The MOSFET layout was specially designed to be assembled and tested using a chip carrier. The gas sensor chip was wire bonded to a chip carrier as shown in Fig. 4.2. All experiments were conducted using an Agilent 5125B Semiconductor Analyzer and a Keithly 2600B Dual Channel Power source.

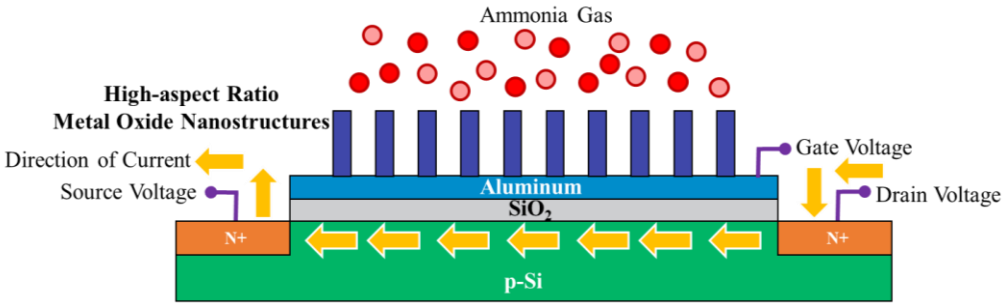

FIG. 4.1. Sketch of the concept of the test of the gas sensor.

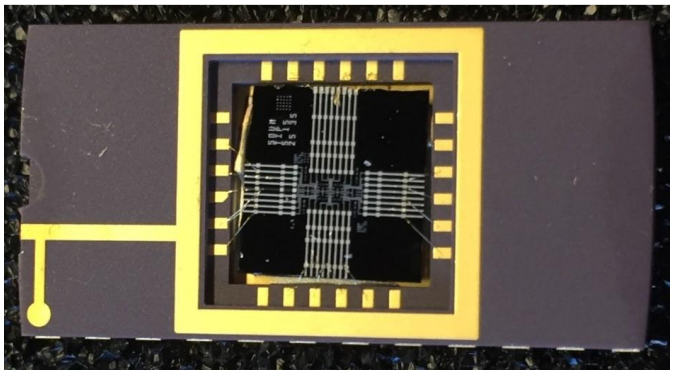

FIG. 4.2. Gas sensor chip assembly by wire bonding in a chip carrier.

Three mass flow controllers were used to adjust ammonia concentrations to test the electrical response during exposure of the ZnO nanowires, TiO_2 nanowires and multiwall TiO_2 nanotubes to various concentrations of ammonia. The device was installed in a 250 ml sealed chamber and all experiments were conducted at room temperature (20°C). The total flow was kept constant at 500 sccm throughout the experiment. A flow process diagram of the testing setup used in this work is shown in Fig. 4.3 and the actual setup-up instrumentation is shown in Fig. 4.4. The chip carrier was inserted inside the custom made gas air tight chamber during testing of sensor as shown in Fig. 4.5.

The change of the I/V characteristic of the ChemFET is directly related to the work function changes of the metal oxide material due to a creation of an internal voltage drop. In general, in certain temperature range, the chemisorption of oxygen molecules involves the trapping of electrons in from the metal oxide material. This chemisorption of oxygen results in a decrease of the free charge carrier concentration (electrons) in the case of n-type metal oxides(e.g. ZnO) or an increase of the free charge carriers concentration (holes) in the case of p-type semiconductors (e.g. TiO_2). The sensing mechanism includes direct charge transfer from the absorbed gas molecules to the ZnO (TiO_2) nanostructure, and modulation of the Ohmic (Schottky) contact at the ZnO/Al (TiO_2/Al) contacts. This chapter will be about the electrical response of the ChemFET with ZnO nanowires, TiO_2 nanowires, and multiwall TiO_2 nanotubes. The proposed sensing mechanism will be explained in the next chapter in full with a physical, chemical and band model which supports the results from gas testing.

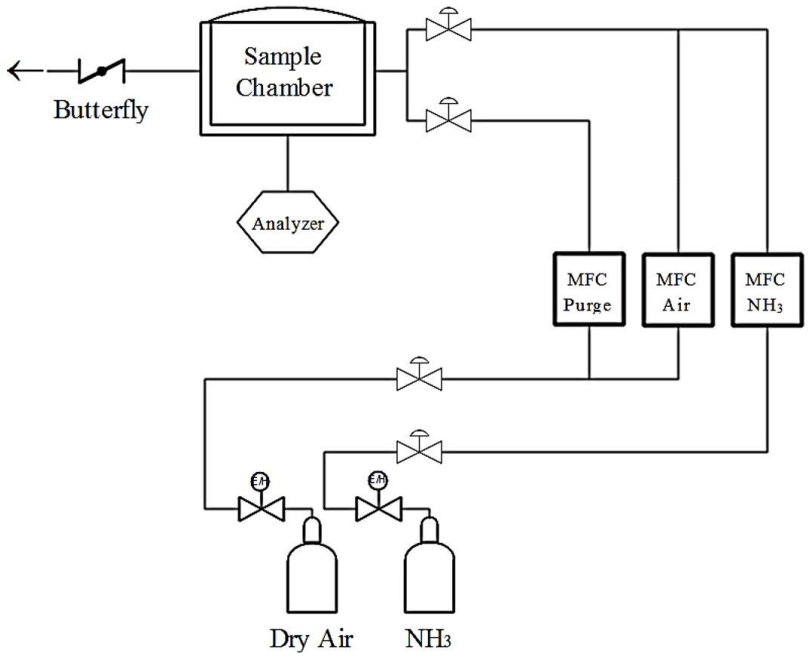

FIG. 4.3. Flow process diagram of gas testing setup.

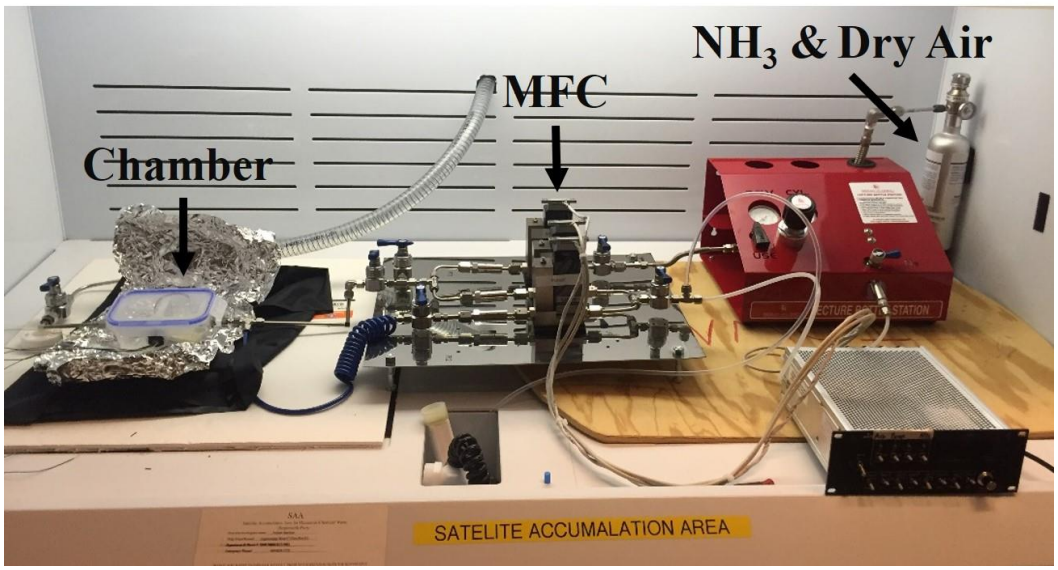

FIG. 4.4. Actual design for gas testing.

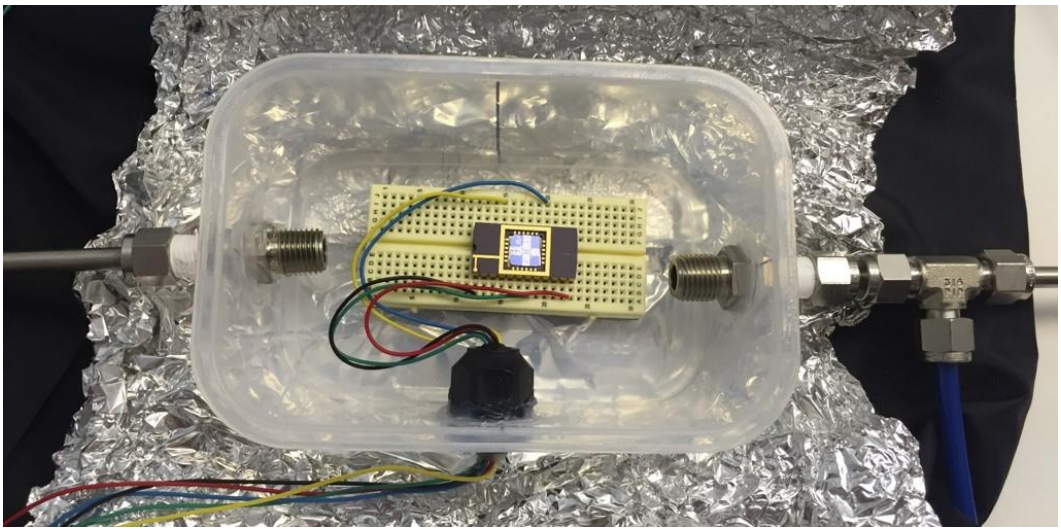

FIG. 4.5. Chip carrier inserted in a 250 ml gas testing chamber.

4.2. ZnO Nanowire ChemFET - MOSFET I-V Characteristics during Gas Exposure

Fig. 4.6 shows the curves of I_D (Drain Current)-V_{DS} (Drain-Source Voltage) characteristics of the device both under a pure air environment as well as under exposure to 25 ppm ammonia (the OSHA (Occupational Safety & Health Administration) TLV level of ammonia exposure) after 2 minutes of exposure (Note that measurements of the I-V characteristics before and after the anodization process itself did not show measurable changes). One can clearly see an upward shift in current due to the ammonia exposure. This shift is also apparent in the I_D-V_{GS} (Gate-Source Voltage) characteristic shown in Fig. 4.7, where the threshold voltage (V_{th}) can be seen to shift from 247 mV to 191 mV due to the ammonia exposure. The dominant sensing mechanism for V_{th} shift is due to the fact that there is a separation of charge at the ZnO/Al interface during chemisorption of oxygen or ammonia molecules which leads to a change of the carrier density in the inversion channel of the MOSFET. A full explanation of this phenomena will be covered in next chapter with a physical, chemical, and band diagram model.

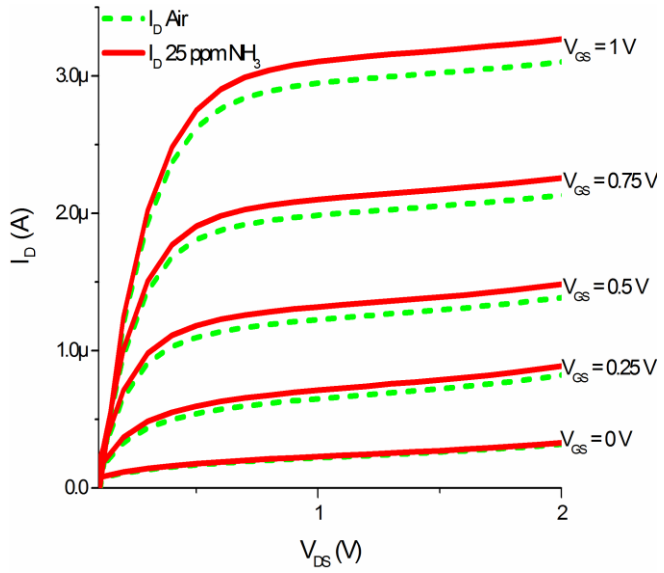

FIG. 4.6. I_D/V_{DS} characteristics of the MOSFET (L=30µm, W=30µm) gas sensor under exposure of air (dashed green line) and 25 ppm ammonia (solid red line) operating at room temperature.

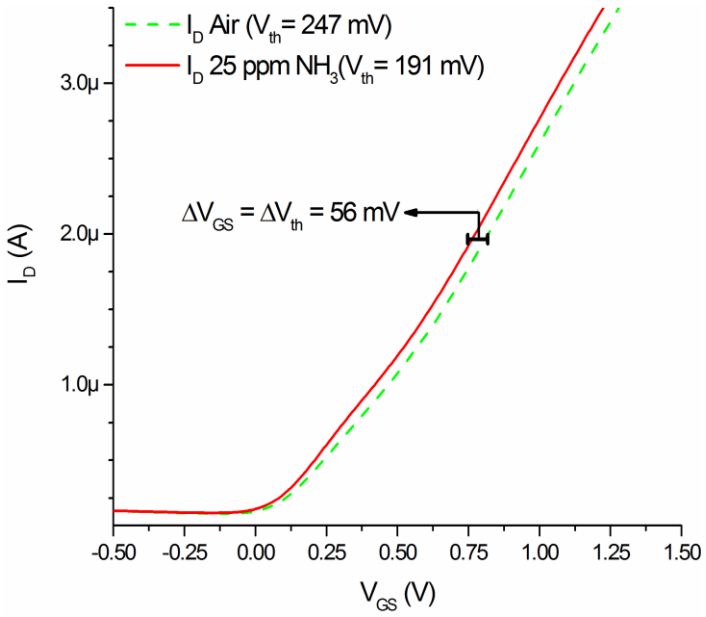

FIG. 4.7. I_D-V_{GS} output characteristics showing a shift in V_{th} after exposure for 2 minutes in 25 ppm ammonia at room temperature.

4.2.1 ZnO Nanowire ChemFET – Sensitivity

The sensitivity of the device was measured at 20 °C with a V_{DS} of 50 mV and a floating gate. The sensitivity (S_g) is defined as:

$$S_{g\text{-}N\text{-}type} = \frac{R_a - R_g}{R_a} * 100[\%] \quad (4.1)$$

where R_a is the channel resistance of the ChemFET under exposure to pure air, while R_g is the channel resistance in the presence of the ammonia gas. The channel resistance for ammonia exposure was measured after 60 seconds of exposure. Fig. 4.8 shows the ChemFET sensitivity for exposure to 25 ppm to 200 ppm ammonia in pure air. The sensor response shows a nonlinear, monotonic relationship between gas concentration and sensitivity, $S_{g\text{-}N\text{-}type}$.

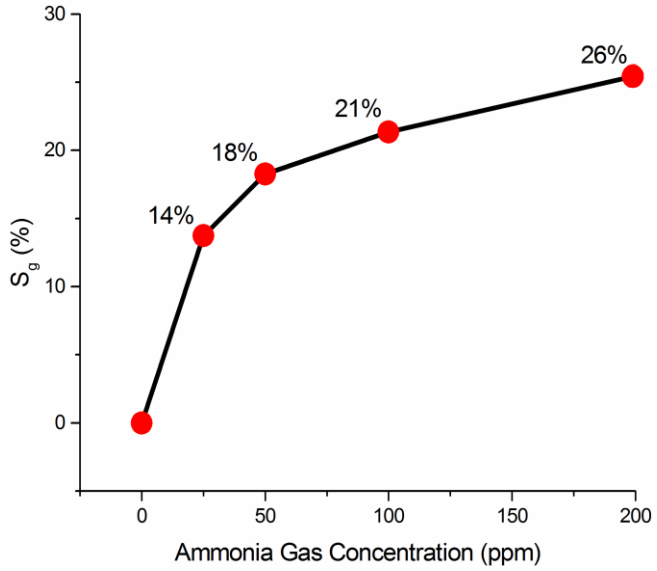

FIG. 4.8. Sensitivity of gas sensor after exposure for 1 minute in 25 ppm, 50 ppm, 100 ppm and 200 ppm ammonia.

4.2.2 ZnO Nanowire ChemFET - Transient Response

The transient response of the device was also analyzed in this configuration (V_{DS} = 50 mV, and a floating gate). The sensor was first subject to equilibrium stabilization in air for 1 minute and then to 25 ppm ammonia exposure until it reached a point of saturation. The ammonia source was then switched off and exposed to clean dry air to examine the recovery time. The resulting transient device response is shown in Fig. 4.9. The sensor response time (t_{90}), defined as the time that the sensor took to reach 90% of its saturation level response to the 25 ppm ammonia exposure, is approximately 8 minutes. The recovery time (t_{10}), taken as the time taken for the sensor to reach 10% of the saturation value in clean air, is approximately 27 minutes.

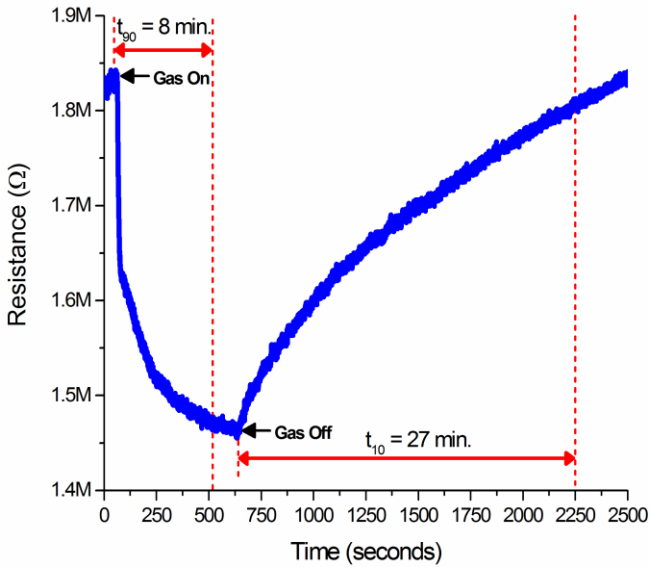

FIG. 4.9. Transient response of gas sensor in 25 ppm ammonia showing a response time of 8 minutes, and a recuperation time of 27 minutes.

The ZnO nanowire ChemFET was further investigated in order to verify reproducibly of output response and life time of the device. Fig. 4.10 shows the sensitivity for exposures to 5-100 ppm ammonia of a two year old ZnO ChemFET gas sensor. The

device was subjected to three 2-min exposures to different concentrations of ammonia. Each experiment was followed by 10 min in dry air and 15 min to room air. Compared with the ZnO nanowire ChemFET sensitivity in Fig. 4.8, Fig. 4.10 shows that the sensitivity decayed by ~2X after two years. Even though the sensitivity decayed, the device was able to detect low concentrations of ammonia after two years.

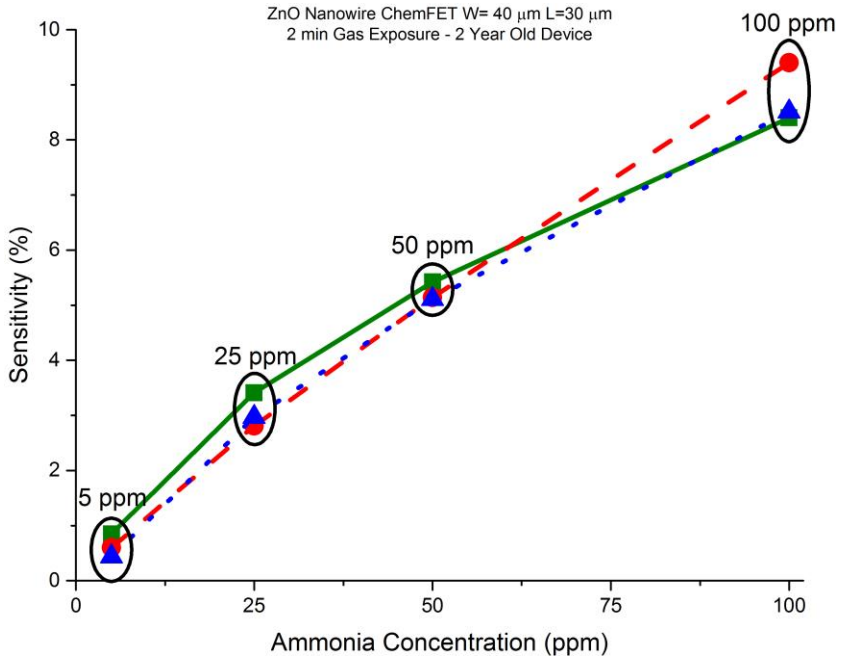

FIG. 4.10. Sensitivity of a two year old ZnO nanowire ChemFET gas sensor after multiple exposures for 2 minute in 5 ppm, 25 ppm, 50 ppm and 100 ppm ammonia.

4.3. TiO_2 Nanowire ChemFET – MOSFET I-V Characteristics during Gas Exposure.

Fig. 4.11 shows the I_D –V_{GS} characteristics of the device both under a pure air environment as well as under exposure to 200 ppm ammonia after 2 minutes of exposure. Fig. 4.11 shows a V_{th} in the positive bias from -1.05 V to -1 V due to the exposure to ammonia. The dominant sensing mechanism for V_{th} shift and change in channel resistance across the source and drain is due to the fact the change of work function of the TiO_2

surface is accompanied with a separation of charge at the TiO_2/Al interface during chemisorption of oxygen or ammonia molecules which leads to a change of the carrier density in the inversion channel of the MOSFET. This will be explained in detail in the next chapter.

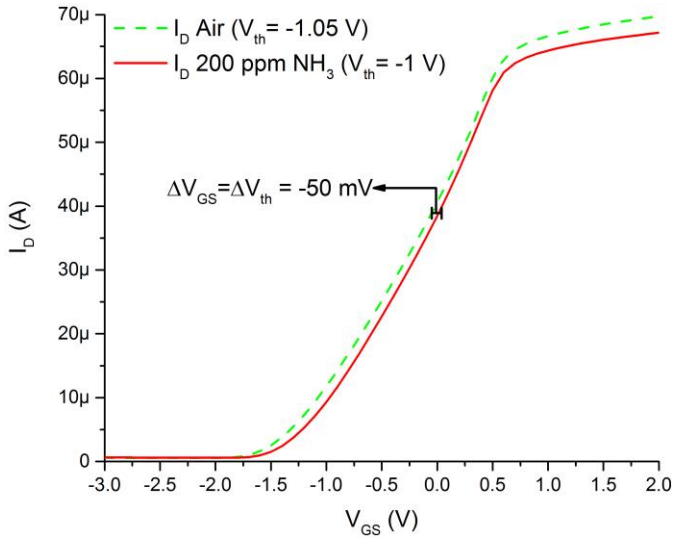

FIG. 4.11. I_D-V_{GS} output characteristics showing a negative shift in V_{th} after exposure for 2 minutes in 200 ppm ammonia at room temperature of a TiO_2 nanowire ChemFET gas sensor (L=20 µm, W=30 µm).

4.3.1 TiO_2 Nanowire ChemFET – Sensitivity

The sensitivity of the TiO_2 nanowire device was measured at 20 °C with a V_{DS} of 0.5 V and a floating gate. The sensitivity (S_g) is defined as:

$$S_{g\text{-}P\text{-}type} = \frac{R_g - R_a}{R_a} * 100[\%] \qquad (4.2)$$

where R_a is the channel resistance of the ChemFET under exposure to pure air, while R_g is the channel resistance in the presence of the ammonia gas. The channel resistance for ammonia exposure was measured after 8 minutes of exposure. Fig. 4.12 shows the TiO_2 nanowire ChemFET sensitivity for exposure to 25 ppm to 200 ppm ammonia in pure air.

The sensor response shows a nonlinear, monotonic relationship between gas concentration and sensitivity, S_g, with a detection limit of 50 ppm ammonia.

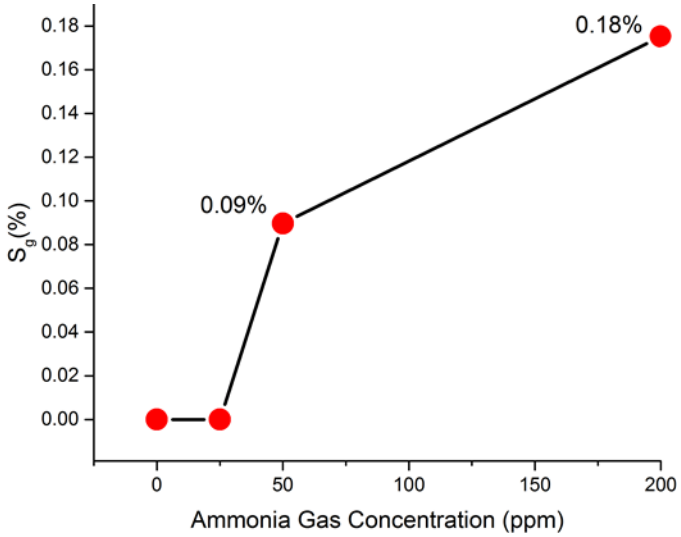

FIG. 4.12. Sensitivity of TiO_2 nanowire ChemFET gas sensor (L= 20µm, W=30 µm) after exposure for 8 minute in 25 ppm, 50 ppm, and 200 ppm ammonia.

4.3.2 TiO_2 Nanowire ChemFET – Transient Response

The transient response of the TiO_2 nanowire ChemFET gas sensor was analyzed in this configuration (V_{DS} = 0.5 V, and a floating gate). The sensor was first subject to equilibrium stabilization in air for 1.5 minute, then to 200 ppm ammonia for 8 min, and finally to a 50 min air purge. The resulting transient device response is shown in Figs. 4.13(a)-(b). In this case, the TiO_2 nanowire ChemFET gas sensor does not reach a saturation point nor a recuperation point. However, as shown in Fig. 4.13 (b), the device was able to detect ammonia with a sensibility of 0.18% by looking at the slope difference between the air stabilization (0-1.5min), and NH_3 & air stages (1.5-9.5min). It seems that TiO_2 nanowire ChemFET gas sensor is not suitable for this kind transient response configuration. Similar experiments were repeated 50 ppm NH_3 showing no saturation point

nor a recuperation time but with a 0.089% sensitivity after 8 minutes to exposure to gas. TiO_2 nanowire ChemFET was not able to the ammonia TLV of 25 ppm. After exposure to NH_3 & air, the nanowires seemed that reached a steady state, which is corresponds to general characteristics of gas absorption/reaction on a solid surface. According to the collision theory of the reaction rate, the higher the concentration of reactive molecules, the more frequently they collide with an adsorption site and are adsorbed. However, the TiO_2 nanowire configuration has a dense concentration of nanosized crystals of TiO_2 which doesn't allow a faster adsorption and desorption of the gases. The gas-absorption rate becomes close to the gas-desorption rate when the TiO_2 nanowires are exposed to ammonia gas. One way to improve this could be by rising the operation temperature. This transient response behavior is not the case with the TiO_2 nanotube ChemFET explained next.

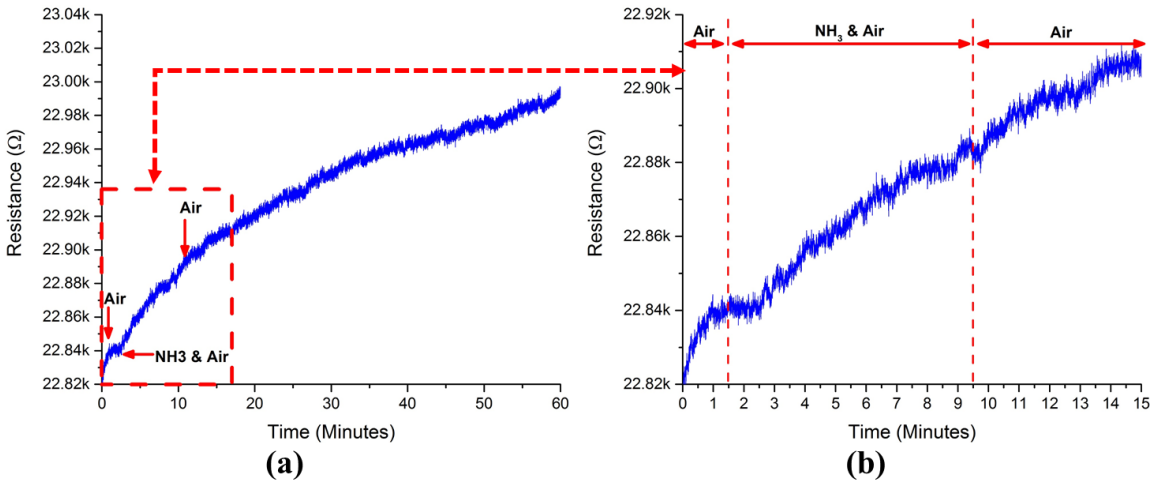

FIG. 4.13. Transient response TiO_2 nanowire ChemFET gas sensor (L= 20µm, W=300 µm) showing no saturation point after 8 min exposure to 200 ppm ammonia, and irreversible characteristics after 50 minutes in air purge.

4.4. Multiwall TiO_2 Nanotube ChemFET – MOSFET I-V Characteristics

Fig. 4.14 shows the curves of I_D –V_{GS} characteristics of the device both under a pure air environment as well as under exposure to 200 ppm ammonia after 2 minutes of exposure. One can clearly V_{th} shift in the positive bias from – 1.4V in air to -1.3V in ammonia. The threshold voltage shift can be attributed to a change in the potential gate due to the formation of a dipole layer when the ammonia is been dissolved into multiwall TiO_2 nanotubes and moves to the aluminum/SiO_2 interface. This change of potential at the gate is a reversible process after the sensor is exposed back to the equilibrium air level.

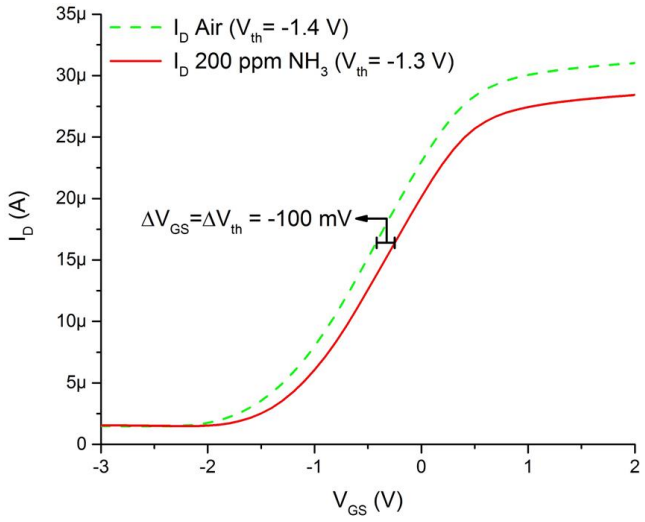

FIG. 4.14. I_D-V_{GS} output characteristics showing a negative shift in Vth after exposure for 2 minutes in 200 ppm ammonia at room temperature of a multiwall TiO_2 nanotube ChemFET gas sensor (L=20 μm, W=30 μm).

4.4.1 Multiwall TiO_2 Nanotube ChemFET – Sensitivity

The sensitivity of the TiO_2 nanowire device was measured at 20 °C with a V_{DS} of 0.5 V and a floating gate. The sensitivity ($S_{g\text{-}P\text{-}type}$) is defined as Equation 4.2. The channel resistance for ammonia exposure was measured after 8 minutes of exposure. Fig. 4.15

shows the multiwall TiO_2 nanotube ChemFET sensitivity for exposure to 25 ppm to 200 ppm ammonia in pure air. The sensor response shows a nonlinear, monotonic relationship between gas concentration and sensitivity, $S_{g\text{-}P\text{-}type}$. Metal oxide nanostructures are known to show non-linear behavior with respect to the test gas concentration when the particles have an average diameter larger than 20nm.

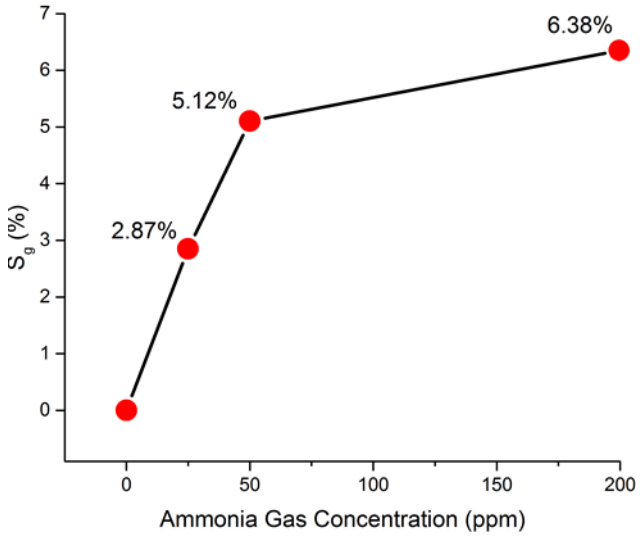

FIG. 4.15. Sensitivity of multiwall TiO_2 nanotube ChemFET gas sensor (L= 20µm, W=300 µm) after exposure for 8 minute in 25 ppm, 50 ppm, and 200 ppm ammonia.

Multiwall TiO_2 nanotube ChemFET gas sensor showed quick response during exposure to 200 ppm ammonia. For this reason, the sensitivity of different sensors across the same die was measured to compare the electrical output differentiation across transistors with different gate sizes. Fig. 4.16 shows sensitivity ratios of transistors of different sizes during the exposure to 200 ppm ammonia for 1 minute with a V_{DS}=0.5V and a floating gate. Fig. 4.16 indicates that the sensitivity of the transistor with a shorter gate length always outperforms the sensitivity with a longer gate length. For instance, the sensitivity of the 20 µm transistor was about 1.88X greater than the sensitivity of the 40

μm. This suggests that a transistor with a short gate length needs to be in consideration for an optimum multiwall TiO_2 nanotube ChemFET gas sensor.

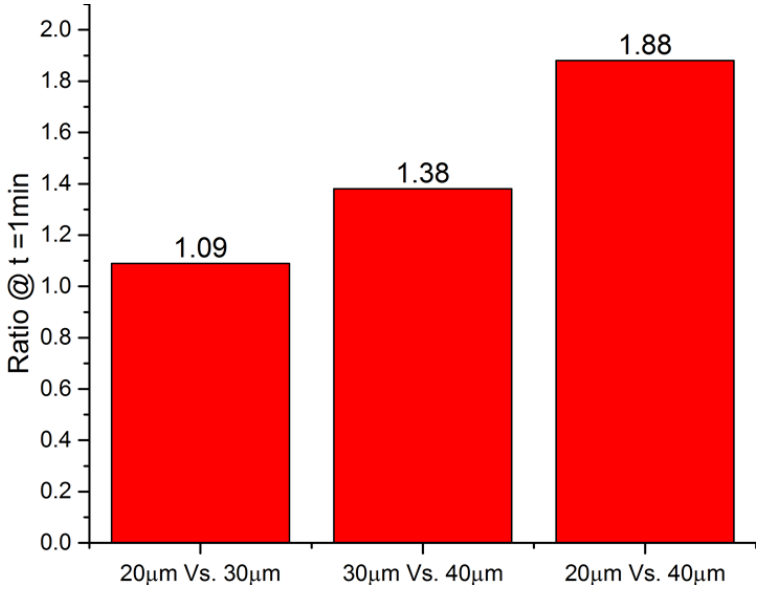

FIG. 4.16. Sensitivity comparison after 1 min of exposure to 200 ppm ammonia of transistors from same die with different gate lengths.

4.4.2 Multiwall TiO_2 Nanotube ChemFET – Transient Response

The transient response of a multiwall TiO_2 nanotube device was analyzed in this configuration (V_{DS} = 0.5 V, and a floating gate). The sensor was first subject to equilibrium stabilization in air for 1.5 minute and then to 200 ppm ammonia for 8 min. The ammonia source was then switched off and exposed to clean dry air to examine a recovery time. The resulting transient device response is shown in Fig. 4.17. The multiwall TiO_2 nanotube ChemFET did not reach a saturation point after 8 minutes and required over 2 hours to reach a recuperation point.

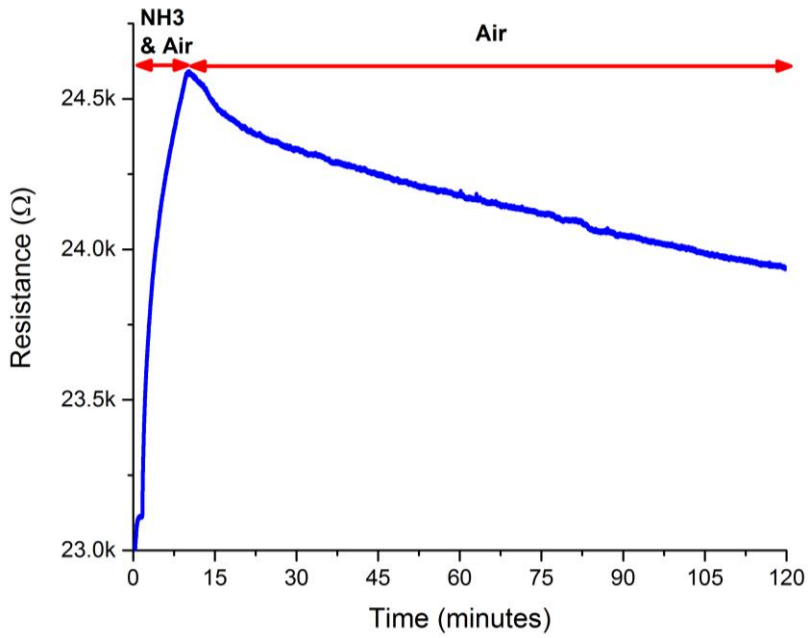

FIG. 4.17. Transient response of a multiwall TiO_2 nanotube ChemFET (L= 20µm, W=30 µm) gas sensor in 200 ppm ammonia showing no saturation point after 8 minutes and a recuperation point of over 2 hours.

Additionally, the multiwall TiO_2 nanotube ChemFET gas sensor was subjected to a multistep transient function analysis to verify sensitivity response over consecutive exposures steps of 200 ppm ammonia. Each etch step consisted of a 2 min air exposure, immediately followed by a 2 min exposure to 200 ppm ammonia. With a V_{DS} = 0.5 and a floating gate, the device shows a decay in sensitivity as is exposed multiple times to 200 ppm ammonia (Fig. 4.18). The first, second and third step sensitivities ($S_{g\text{-}P\text{-}type}$) were 4.97%, 0.98%, and 0.59% respectively. This experiment suggest that the p-type multiwall TiO_2 nanotube ChemFET gas sensor has a rapid response to 200 ppm ammonia oriented to single use application.

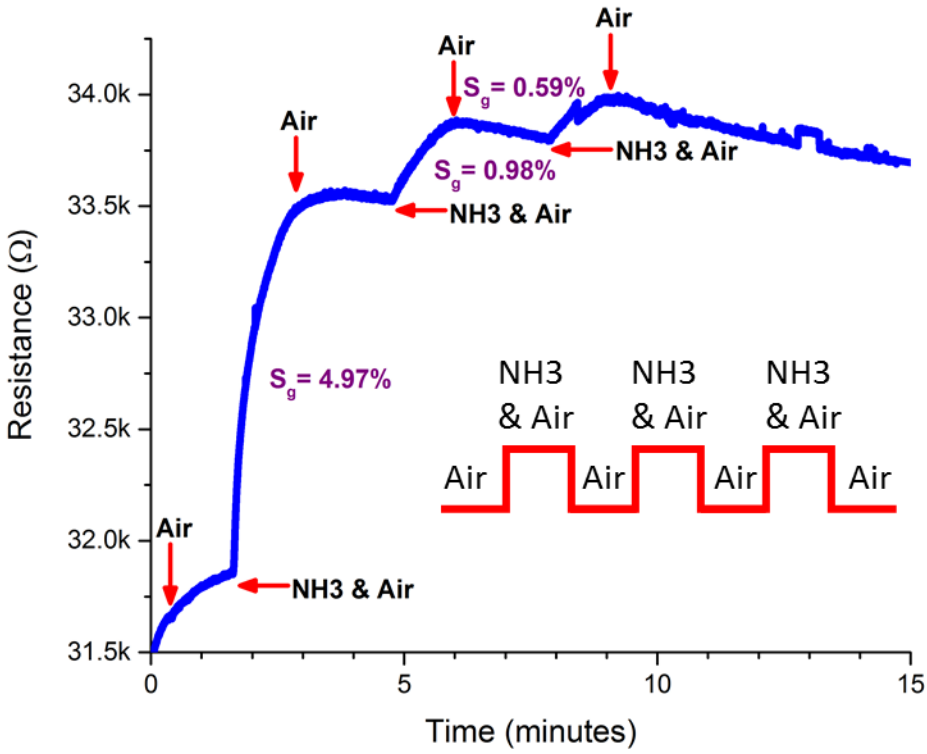

FIG. 4.18. Multistep transient function of a multiwall TiO2 nanotube ChemFET gas sensor (L= 20µm, W=30 µm) showing a sensitivity decay during multiple 2 min exposures steps of 200 ppm ammonia.

The multiwall TiO_2 nanotube ChemFET was further investigated in order to verify reproducibly of output response, and life time of the device. Figs. 4.19(a)-(b) show the sensitivity for exposures to 5-100 ppm ammonia of a two month old and a one year old multiwall TiO_2 ChemFET gas sensors. These devices were subjected to three 2-min exposures to different concentrations of ammonia. Each experiment was followed by 10 min in dry air and 15 min to room air. The sensitivity of the two month old device (Fig. 4.19(a)) showed in general a higher output response than the one year old device (Fig. 4.19(b)). Fig. 4.20 shows a condense version of Figs. 4.19(a)-(b) with error bars of different measurements.

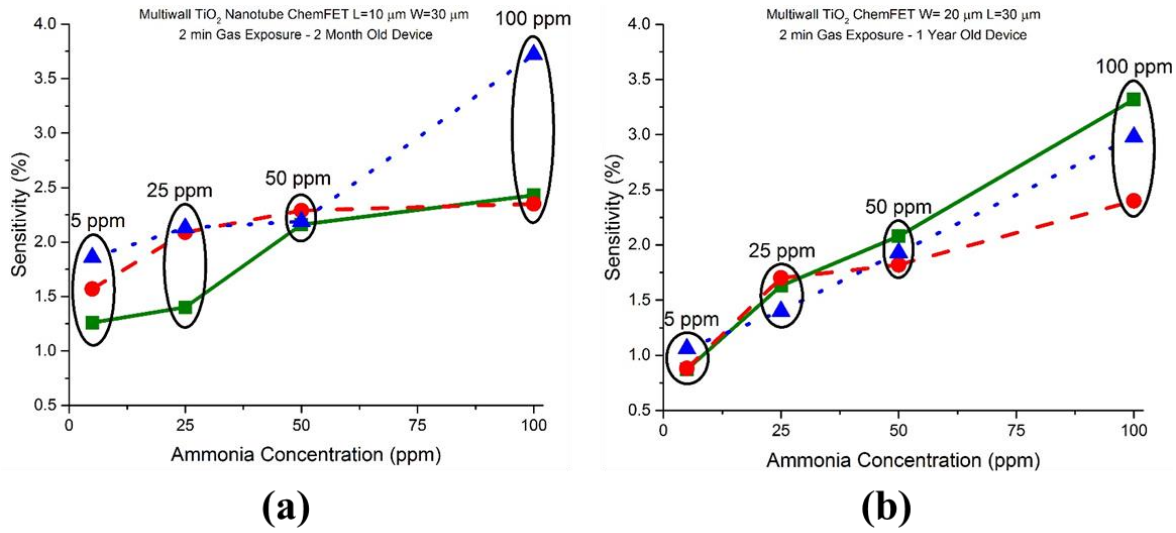

FIG. 4.19. Sensitivity of multiwall TiO_2 nanotube ChemFET gas sensors after exposure for 1 minute in 5 ppm, 25 ppm, 50 ppm, and 100 ppm ammonia. (a) Two month old ChemFET. (b) One year old ChemFET

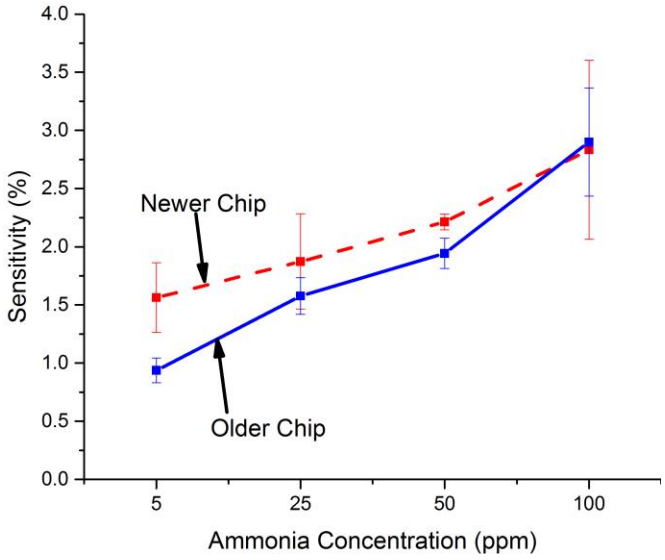

FIG. 4.20. Sensitivity of a two month and one year old multiwall TiO_2 nanotube ChemFET gas sensors after exposure for 1 minute in 5 ppm, 25 ppm, 50 ppm, and 100 ppm ammonia.

Chapter 5 Physical and Chemical Detection Mechanism of ChemFET

Chemical sensing in ChemFET sensors is achieved by oxidation reactions between chemical species and chemisorbed oxygen, causing a decrease in the surface barrier between metal oxide grains and change of electrostatic conditions at the metal-oxide/gate-metal interface. Transistor-based sensors devices are normally operated in saturation mode. The drain current versus voltage gate relationship for the saturation region can be describe by:

$$I_D = \frac{\mu_n \varepsilon_{ins} W}{2 L d_{ins}} (V_{GS} - V_{th})^2 \tag{5.1}$$

$$V_{th} = \frac{2 d_{ins} [e N_a \varepsilon_s \Phi_F]^{1/2}}{\varepsilon_{ins}} - \frac{Q_{ss} d_{ins}}{\varepsilon_{ins}} + \Phi_{ms} + 2\Phi_F \tag{5.2}$$

where W and L are the channel width and length, respectably; μ_n is the channel electron mobility; ε_{ins} and d_{ins} are the insulator permittivity and thickness respectively; e is the elementary charge; N_a the bulk doping concentration; Φ_{ms} the metal-to-semiconductor work function, ε_s the semiconductor permittivity; Q_{ss} the insulator charge density; and Φ_F the Fermi potential, which is the potential difference between the Fermi level and the intrinsic Fermi level. Device parameters such as device dimensions, electron mobility and doping concentration are inherent to the choice of materials, the design and the processing of the MOSFET. Those values are fixed once the MOSFET is fabricated. However, according to Eqs .5.1 and 5.2 in addition to the applied voltage, charges located in or at the SiO_2, the metal-to-semiconductor work function difference, and any internal gate voltage drop, can also influence the drain current during exposure to a gas changing the I/V characteristics of the device. This requires the injection of a charge species capable of a creation of a charge separation at the Al/SiO_2 interface. When a ZnO or TiO_2 surface

absorbs ammonia or air atoms, there is a charge transfer between the adsorbates and the surface of the metal oxide material. As consequence, the work function of the metal oxide material changes accompanied with a separation of charge. The change of the I/V characteristic of the ChemFET is directly related to the work function changes of the metal oxide material due to a creation of an internal voltage drop. In general, in certain temperature range, the chemisorption of oxygen molecules involves the trapping of electrons in from the metal oxide material. This chemisorption of oxygen results in a decrease of the free charge carrier concentration (electrons) in the case of n-type metal oxides(e.g. ZnO) or an increase of the free charge carriers concentration (holes) in the case of p-type semiconductors (e.g. TiO_2).

The proposed sensing mechanism includes direct charge transfer from the absorbed gas molecules to the ZnO (TiO_2) nanostructure, and modulation of the Ohmic (Schottky) contact at the ZnO/Al (TiO_2/Al) contacts. This proposed sensing mechanism will be explained in this section with a physical, chemical and band model which supports the results from gas testing.

5.1. ZnO Nanowire ChemFET Sensing Mechanism

As shown in Section 4.2, ChemFETs with ZnO nanowires of the gate of the MOSFET structure were tested by measuring the V_{th} shift and the channel resistance with a floating gate (V_{gs}=0) during the exposure to 25-200ppm ammonia. The dominant mechanism for V_{th} shift and change in channel resistance across the source and drain is due to the fact that there is a separation of charge at the ZnO/Al interface during chemisorption of oxygen or ammonia molecules which leads to a change of the carrier density in the inversion channel of the MOSFET. Figs. 5.1(a)-(b) show a physical and chemical model

of the proposed sensing mechanism of a ChemFET with ZnO gains. In air atmosphere, oxygen molecules are absorbed on the surface of the ZnO grain. The absorbed oxygen species capture free electrons from the conduction band of the ZnO surface to form oxygen ions. Sequentially, electron depletion layers on each of the ZnO nanograins are produced, as shown in Fig.5.1(a).

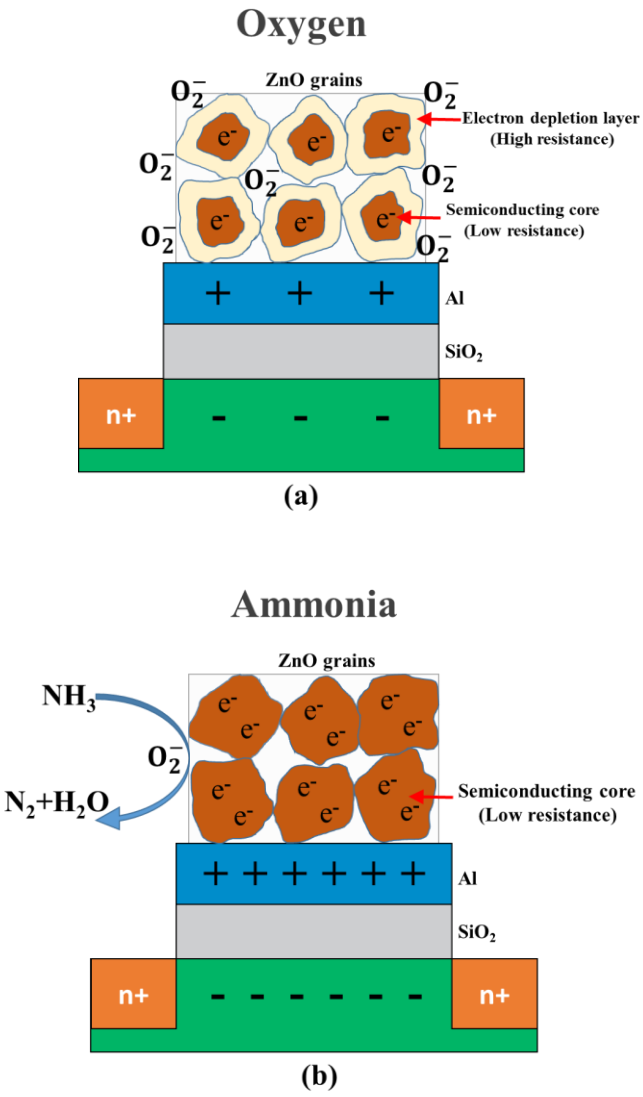

FIG. 5.1 Physical & chemical model of ZnO nanostructures on gate of a ChemFET. (a) During exposure to atmospheric air. (b) During exposure to ammonia.

The absorbed oxygen molecules could be transferred into oxygen ions (O^-, O_2^-, or O_2^-) by extracting free electrons from the ZnO surface which leads to a decrease in flow of free electrons from grain to grain. The chemical reaction in oxygen could be expressed as:

$$O_2(gas) \rightarrow O_2(ads) \tag{5.3}$$

$$O_2(ads) + e^- \rightarrow O_2^-(ads) \quad if\ temperature < 373K \tag{5.4}$$

$$O_2(ads) + 2e^- \rightarrow 2O^-(ads) \quad if\ temperature \quad 373K - 573K \tag{5.5}$$

$$O^-(ads) + e^- \rightarrow O^{2-}(ads) \quad if\ temperature < 373K \tag{5.6}$$

This interaction with oxygen results in increment of the electron depletion layer and a decrease of the semiconducting core in each of the ZnO grains. Since the interface between ZnO nanowire and aluminum gate forms an Ohmic contact due to the fact that the work function of ZnO (ϕ_{ZnO} = 7.30 eV) is larger than the work function of Al (ϕ_{Al} = 4.28 eV), the depletion layer formation on each ZnO grain affects in direct proportional to the fermi level of the aluminum gate. In oxygen environment, the decrease in free carrier concentration in the ZnO surface causes the aluminum gate film to become less positively charge, which makes the charge concentration on the inversion channel to decrease (Fig. 5.1(a)). This diminution of charges carriers in the inversion channel between source and drain results to an increase in channel resistance. As an example, this can be seen in Fig. 5.2(a) where the channel resistance was measured with a constant V_{ds} = 50mV and a floating gate (V_{gs}=0) of a ChemFET with ZnO nanowires under exposure to air and ammonia. Fig. 5.2(a) shows the channel resistance increases in the air region. The positive V_{th} shift bias is another indication that the charge concentrations in the inversion channel is decreasing when the device is exposed to air, as shown in Fig. 5.2(b).

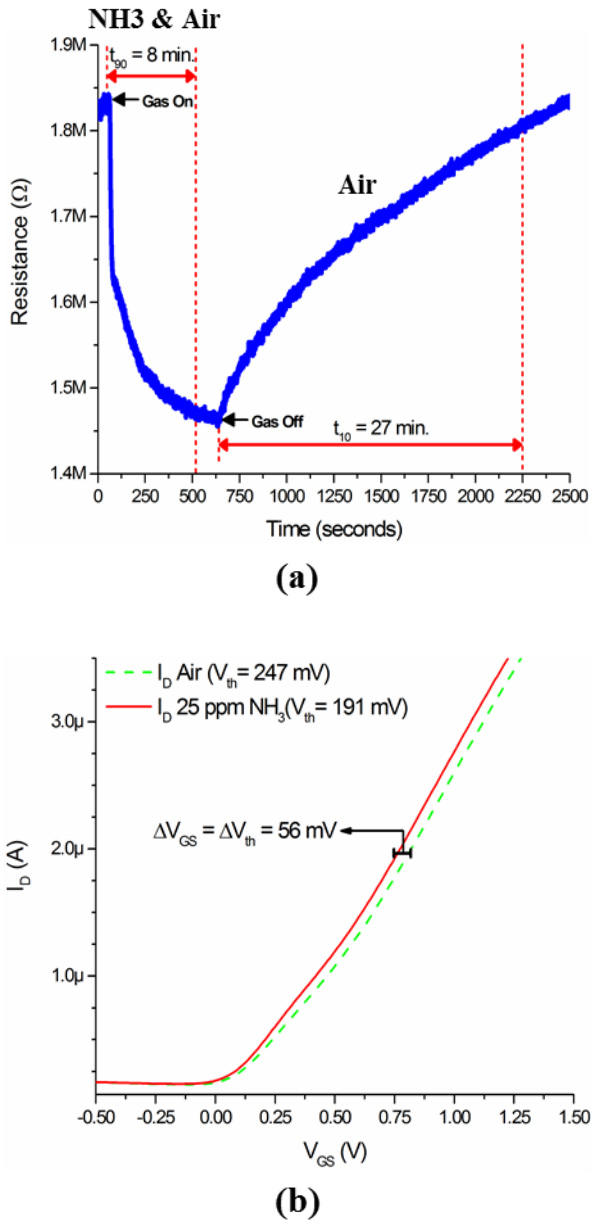

FIG. 5.2. Electrical output of ChemFET with ZnO nanowires. (a) Transient response under 25 ppm ammonia and air. (b) V_{GS}/I_D characteristics under exposure to air and 25 ppm ammonia.

On the other hand, when the ammonia gas is introduced, the absorbed ammonia molecules on the ZnO nanowire causes the following reaction:

$$NH_3 + O_2^- \rightarrow N_2 + H_2O + e^- \quad (5.7)$$

Captured electrons are released back to conduction band of the ZnO nanowire surface and lead to the reduction in the depletion layer between ZnO grains, as shown in Fig. 5.1(b). As expected from Eq. 5.7, chemisorption of ammonia molecules on the ZnO nanowires will produce an electron transfer from aluminum gate to the ZnO surface through the Ohmic contact inducing a charge separation at the ZnO/Al interface making the aluminum more positively charged. Fig. 5.1(b) shows that the more positively charge aluminum gate induces an increment of the charge carrier concentration at the inversion channel. The increase in charge carrier concentration in the channel between the source and drain of the MOSFET structure leads to a decrease of channel resistance. This can be seen in Fig. 5.2(a), where the channel resistance goes down when the ChemFET with ZnO nanowires is exposed to ammonia gas. Furthermore, the free electrons released from the ZnO nanowires acts as an extra voltage source connected in series with the externally applied voltage source V_{gs}. As shown in Fig. 5.2(b), V_{th} of the ChemFET device shift in the negative bias since the charge carriers in the inversion channel increased due to the chemisorption of ammonia molecules on the ZnO nanowire surface. In addition, by taking into account that the slopes of the V_{thAir} and V_{thNH3} are the same, it is evident that charge separation due to the chemisorption process of oxygen ions and ammonia molecules is located at the ZnO/Al interface rather than the charge density in the SiO_2/Si interface.

According to the proposed reaction kinetic in Eqs. 5.3-5.7, a schematic energy band diagram of the ZnO-Al-SiO2-Si structure before and after exposure to ammonia is shown in Figs. 5.3(a)-(b). During exposure to atmospheric oxygen or any oxidative gas, a depletion layer is formed on the ZnO surface. As shown in Fig. 5.3(a), acceptor levels are created and electrons located in the conduction band are trap. The depletion layer on the

surface of the grains makes bending of the upward band, making electrons to require more energy to reach the surface. In this case there is a mitigation of the free electron transport and charge separation at the ZnO/Al interface which makes the aluminum gate to become less positively charged. As shown in Fig. 5.2(a), the channel resistance across the source and drain increases during the exposure to oxygen due to the mitigation of electron transport and reduction of charge separation at the ZnO/Al interface.

On the contrary, when the ZnO surface is exposed to a reducing gas, such as ammonia, the negative charges trapped on the surface are reduced by the formation of N_2 and H_2O. This results in the mitigation of the depletion layer in each grain and the reduction of the double Schottky barrier between ZnO grains. This enables a progressively greater number of electrons to flow from grain to grain. As shown in Fig. 5.3(b), the further bending of the conduction band of the ZnO makes free electrons to accumulate at the ZnO/Al interface which will induce electron transport from aluminum gate to the ZnO surface through the ZnO/Al Ohmic contact. The charge separation due to free electron transportation from the aluminum gate to the ZnO surface will make the fermi level of the aluminum layer to reach down since it becomes more positively charged. This will induce a greater amount of charge carriers in the inversion channel (ΔQ_{inv}), as shown in Fig. 5.3(b). The chemisorption process on the ZnO nanowires lead to a change in work function of metal oxide and a modulation of the Ohmic contact at the ZnO/Al and charge polarization at the ZnO/Al interface, thus directly shifting V_{th} due to the change of carriers in the inversion layer. This band model agrees with experimental results and explains the direction of negative V_{th} shift when the ChemFET with ZnO nanowires is exposed to ammonia gas, as shown in Fig. 5.2(b).

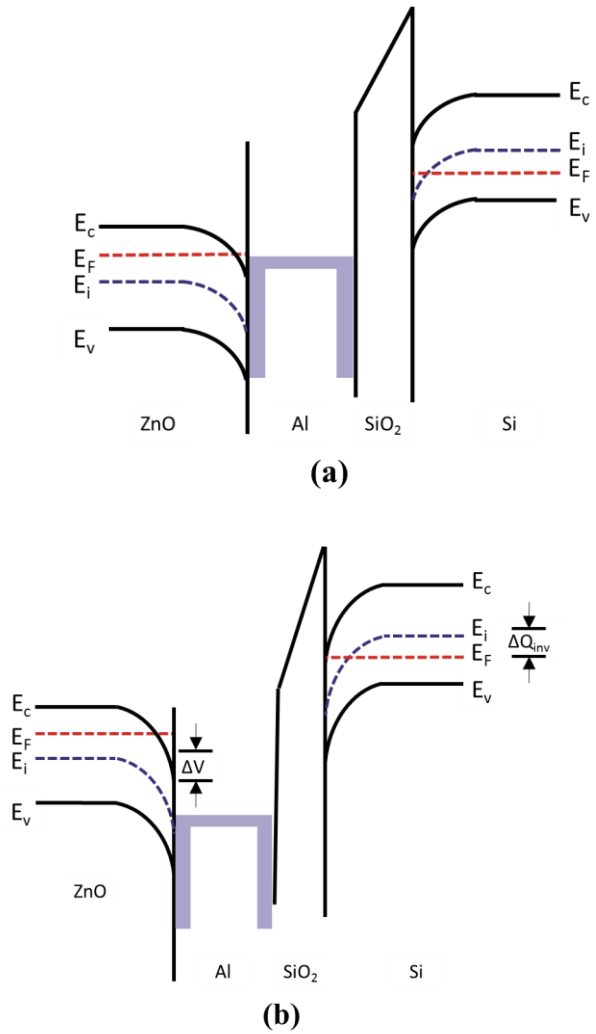

FIG. 5.3. Schematic energy diagram of the ZnO-Al-SiO_2 -Si structure when $V_{gs} > V_{th}$. (a) Under exposure to air. (b) Under exposure to NH_3.

Gas molecules absorbed by the ZnO surface give arise to a charge separation that corresponds to a voltage drop which acts as external gate voltage added in series to V_{gs}. This induces a change in charge carrier concentration in the inversion channel. As a first order approximation, the magnitude of the electron change in the inversion channel in air and ammonia can be defined as:

$$Q_{ZnO-Air} = C_{ox}WL(V_{gs} - V_{thAir}) \tag{5.8}$$

$$Q_{ZnO-NH3} = C_{ox}WL(V_{gs} - V_{thNH3}) \quad (5.9)$$

Where C_{ox} = Total channel capacitance, W = width of gate, L = Length of channel, V_{gs} = Applied gate voltage, V_{thAir} = Threshold voltage in air, V_{thNH3} = Threshold voltage in ammonia. The above equation can be further simplified using $\Delta V_{th\text{-}ZnO}$ as the voltage difference between air and ammonia to calculate charge contribution in the inversion channel due to the chemisorption of ammonia molecules in the ZnO surface as:

$$|\Delta Q_{inv}| = C_{ox}WL(\Delta V_{th-ZnO}) \quad (5.10)$$

For ChemFETs with ZnO nanowires in this work, W = 30µm, L = 45µm (otherwise specified), and C_{ox} = 3.45x10^{-4} F/m^2 (t_{ox} = 100nm). Using V_{thNH3} = 191 mV and V_{thAir} = 247 mV shown in Fig. 5.2(b), Eq. 5.10 leads to $|\Delta Q_{inv}|$ = 2.6x10^{-14} C ~ 163013 electrons in the inversion channel due to chemisorption of 25 ppm ammonia. This in an indication that the charge carrier density changes in the inversion channel.

The chemisorption process of ammonia molecules on ZnO surface of the nanowires leads to transportation of free electrons from aluminum gate layer to the ZnO surface through the ZnO/Al Ohmic contact under exposure to air and ammonia. As described in Eq. 5.10, the change in charge carrier density in the inversion channel ($|\Delta Q_{inv}|$) is directly proportional to the change in threshold voltage (ΔV_{th}). The charge transfer due to the chemisorption process could be explained with the following Eq:

$$f_{ZnO} = \frac{\Delta Q}{\pi r_{AlGate} D_{NW}} \quad (5.11)$$

where r_{AlGate} = radius of coverage of aluminum gate with ZnO nanowires, and D_{ZnO} = The ZnO nanowire density. For the current device, the aluminum gate pattering consist of a circumference with r = 37.5 µm which contains about 131 nanowires per µm^2. Assuming that there is a uniform charge across the ZnO nanowire, the electron transfer rate

due to chemisorption of ammonia, f_{ZnO}, is 0.28 electron per nanowire. This value is close to other transfer rates of ammonia on ZnO surface reported by Yuan *et. al.* (0.184 electron)[90]. The value obtained in this work is slightly higher due to the fact that we are taking into account the entire ZnO nanowire surface area instead of a single ZnO surface. Furthermore, the calculated charge transfer rate was using values when the device was exposed to 25 ppm ammonia. The value reported in literature is an indication that minimum charge transfer value could be obtained with lower concentration of ammonia which can be explored with further investigation of the ChemFET with ZnO nanowires.

5.2. TiO_2 Nanowire and Multiwall TiO_2 Nanotube ChemFET Sensing Mechanism

The sensing mechanism for a ChemFET with TiO_2 nanowires and multiwall TiO_2 nanotubes on the gate is similar than the ChemFET with ZnO nanowires with two main distinctions. (1) Due to the positive slope of the Hall resistance vs. magnetic field measurements described in Section 3.7, the TiO_2 film deposited using ALD corresponds to p-type semiconductor. Since the majority carriers in the TiO_2 film are holes, the chemisorption of oxygen with negative charge and ammonia is different than the n-type ZnO described in the previous section. (2) Rather than an Ohmic contact, the TiO_2/Al interface forms a Schottky contact since the work function of p-type nanocrystalline TiO_2 (ϕ_{TiO2} = 5.23 eV) is larger than the work function of aluminum (ϕ_{Al} = 4.28 eV). By taking into account these two distinctions between the n-type ZnO and p-type TiO_2, the chemisorption of oxygen and ammonia molecules in a p-type metal oxide semiconductor is expected to be much less intense which implies that the effects of charge transfer from TiO_2 nanostructures to the inversion channel will be reduced due to a Schottky contact at

the TiO_2/Al interface. This section will describe a physical, chemical, and band diagram model of the ChemFET with p-type TiO_2 nanowires and multiwall nanotubes.

As shown in Sections 4.3-4.4, ChemFETs with TiO_2 nanowires and multiwall TiO_2 nanotubes on the gate of the MOSFET structure were tested by measuring the V_{th} shift and the channel resistance with a floating gate (V_{gs}=0) during the exposure to 25-200ppm ammonia. The dominant sensing mechanism for V_{th} shift and change in channel resistance across the source and drain is due to the fact the change of work function of the TiO_2 surface is accompanied with a separation of charge at the TiO_2/Al interface during chemisorption of oxygen or ammonia molecules which leads to a change of the carrier density in the inversion channel of the MOSFET. Figs. 5.4(a)-(b) show a physical and chemical model of the proposed sensing mechanism of ChemFET with p-type nanocrystalline TiO_2 grains. In air atmosphere, oxygen molecules are absorbed on the surface of the TiO_2 nanograins. The absorbed oxygen species capture holes from the valence band of the TiO_2 surface to form oxygen ions. Sequentially, a hole accumulation layer on each of the TiO_2 nanograins is produced, as shown in Fig. 5.4(a). This hole accumulation layer can be considered as low resistance shell which once in contact with other TiO_2 grains allows a flow of valance electron from grain to grain.

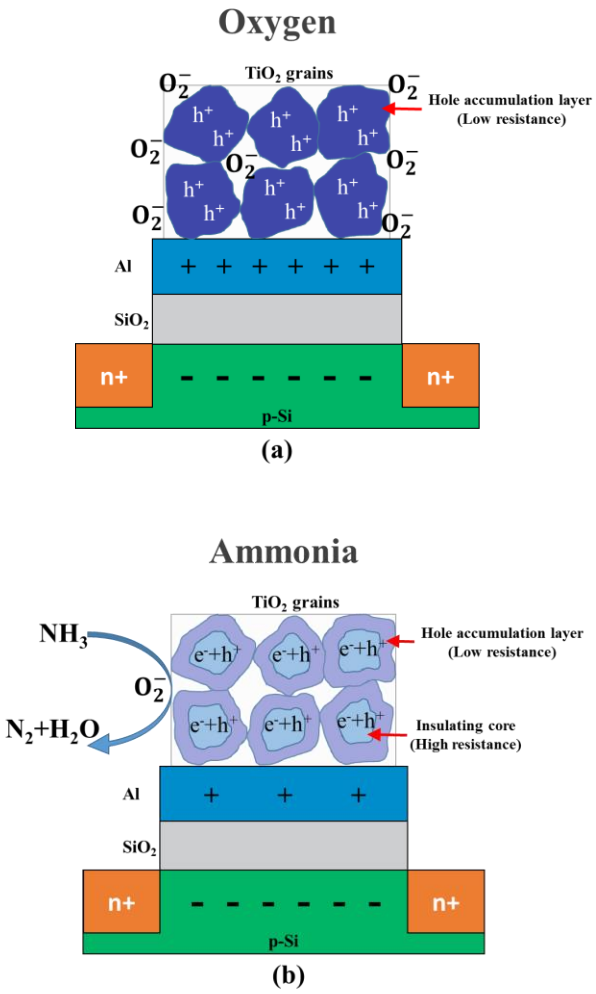

FIG. 5.4. Physical & chemical model of p-type TiO_2 nanostructures on gate of a ChemFET. (a) During exposure to atmospheric air. (b) During exposure to ammonia.

The absorbed oxygen molecules could be transferred into oxygen ions (O^-, O_2^-, or O_2^-) by extracting holes from the TiO_2 surface which leads to an increase in flow valence band electron from grain to grain. The chemical reaction in oxygen could be expressed as:

$$O_2(gas) \rightarrow O_2(ads) \tag{5.12}$$

$$O_2(ads) + h^+ \rightarrow O_2^-(ads) \quad if\ temperature < 373K \tag{5.13}$$

$$O_2(ads) + 2h^+ \rightarrow 2O^-(ads) \quad if\ temperature \quad 373K - 573K \tag{5.14}$$

$$O^-(ads) + h^+ \rightarrow O^{2-}(ads) \quad if\ temperature < 373K \tag{5.15}$$

The absorption of oxygen anions in the p-type TiO_2 surface forms hole accumulation layers near the surface of the material because of the electrostatic interaction between the oppositely charges species (Figs. 5.4(a)-(b)), which stablishes an electronic-core-shell configuration. This electronic-core-shell configuration consist of an insulating region at the cores of the particles, and semiconducting hole accumulation layer near the surface of the particles. The interaction with oxygen molecules with the p-type TiO_2 material results in increment of hole concentration in the hole accumulation layer shell and a decrease in carriers in the insulating core in each of the TiO_2 grains. Since the interface between the TiO_2 surface and aluminum gate forms an Schottky contact, the hole accumulation layer formation on each of TiO_2 grains affects in direct proportionally the fermi level of the aluminum gate. In oxygen environment, an increase of hole concentration in the TiO_2 surface cause the aluminum gate to become more positively charged, which creates an increase of charge separation in the TiO_2/Al interface making the charge concentration in the inversion channel to increase (Fig. 5.4(a)). This addition of charge carriers in the inversion channel between source and drain of the MOSFET results to a decrease in channel resistance. As an example, this can be seen on Fig. 5.5(a) where the channel resistance was measured with a constant V_{ds} = 500mV and a floating gate (V_{gs}=0) of a ChemFET with multiwall TiO_2 nanotubes under exposure to air and ammonia. Fig. 5.5(a) shows the channel resistance decreases in the air region due to the chemisorption of oxygen ions and increase of the hole concentration in the hole accumulation shell. The negative V_{th} shift bias is another indication that the charge concentrations in the inversion channel is increasing when the device is exposed to air, as shown in Fig. 5.5(b).

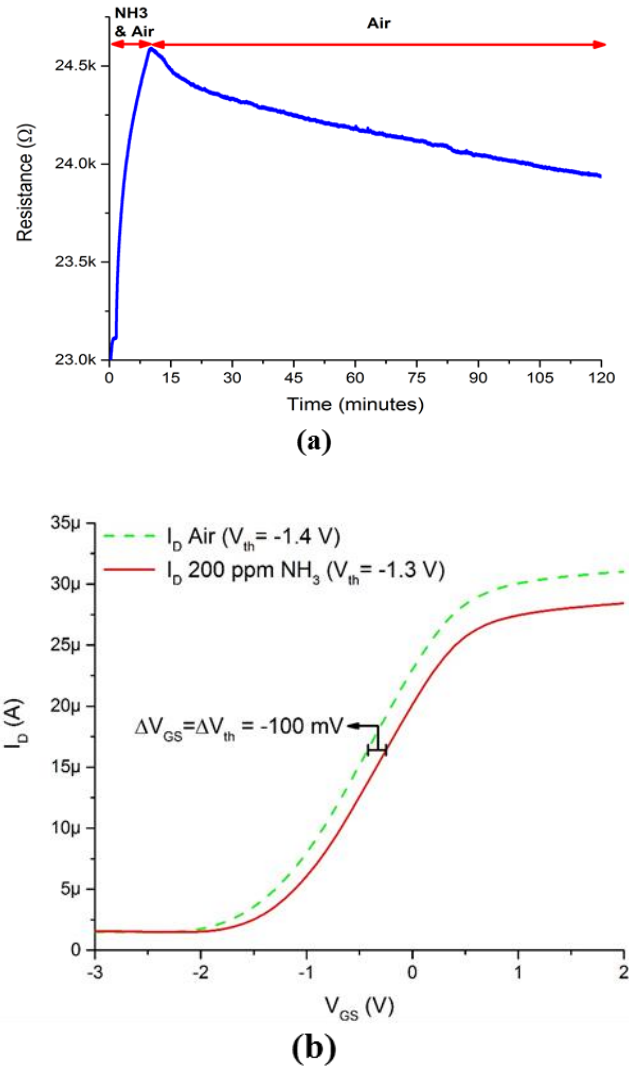

FIG. 5.5 Electrical output of ChemFET with multiwall TiO_2 nanotubes (W= 30 μm, L=20μm). (a)Transient response under 200 ppm ammonia and air. (b)V_{GS}/I_D characteristics under exposure to air and 200 ppm ammonia.

On the other hand, when the ammonia gas is introduced, the absorbed ammonia molecules on the TiO_2 surface causes the following reaction:

$$NH_3 + O_2^- \rightarrow N_2 + H_2O + e^- + h^+ \quad (5.16)$$

Free electrons are captured from the insulating core which leads to the reduction of the hole concentration, as shown in Fig. 5.4(b). As expected from Eq. 5.16, chemisorption of

ammonia molecules on the TiO_2 surface will produce a mitigation of the hole accumulation layer which reduces the charge separation at the TiO_2/Al interface. In addition, free electrons coming from the aluminum layer are expected to have low energy during the chemisorption process and are not expected to penetrate the Schottky barrier at the TiO_2/Al interface. However, the Schottky barrier will modify its characteristics due to the modulation of the work function of the TiO_2 surface during exposure to ammonia and air. Fig. 5.4(b) shows that diminution of hole concentration layer in TiO_2 surface implies that the aluminum gate becomes less positively charged than when it was exposed to air. Because of the less positively charged aluminum gate, the charge carrier concentration at the channel between source and drain decreases. The mitigation of charge carrier concentration in the channel between the source and drain of the MOSFET structure leads to an increase of channel resistance. This can be seen in Fig. 5.5(a), where the channel resistance goes up when the ChemFET with multiwall TiO_2 nanotubes is exposed to ammonia gas. Furthermore, the free electrons released from insulating core of the surface, and the mitigation of the hole concentration at the TiO_2 surface act as an extra voltage source connected in series with the externally applied voltage source V_{gs}; however, this time, it will be a less positively charge extra voltage source than when it the device was exposed to air. Another indication of the chemisorption process is shown in Fig. 5.5.(b) where the V_{th} of ChemFET with multiwall TiO_2 nanotube shifts in the positive bias due to the fact that the charge carriers in the inversion channel decreased due to the chemisorption of ammonia molecules on the TiO_2 nanotube surface. In addition, by taking into account that the slopes of the V_{thAir} and V_{thNH3} are the same, it is evident that charge separation due

to the chemisorption process of oxygen ions and ammonia molecules is located at the TiO_2/Al interface rather than the charge density in the SiO_2/Si interface.

According to the proposed reaction kinetic in Eqs. 5.12-5.16, a schematic energy band diagram of the TiO_2-Al-SiO_2-Si structure before and after exposure to ammonia is shown in Figs. 5.6(a)-(b). During exposure to atmospheric oxygen or any oxidative gas, a hole accumulation layer is formed on the TiO_2 surface. Donor levels are created and electrons located in the valence band accumulate in the surface of the TiO_2. Fig. 5.6(a) shows electrons in the valance band are captured due to the chemisorption of oxygen ions. Here, there is an increase of concentration of holes in the surface of TiO_2 material (building up of an accumulation layer). The building up of the accumulation layer is represented as an upward band bending in Fig. 5.6(a). This will induce great number of valence band electrons to flow to the valence band of the grain right next to it. When p-type TiO_2 grains are exposed to air, a greater number of valence band electrons in the TiO_2 surface induces a charge separation at the TiO_2/Al interface which makes the aluminum gate to become more positively charged. This change in charges in the aluminum gate is shown in Fig. 5.5(a) where the channel resistance across the source and drain contacts decreases during the exposure to oxygen due the increment of the hole density at the surface of the TiO_2 surface and a increment of charge separation at the TiO_2/Al interface.

On the contrary, when the TiO_2 surface is exposed to ammonia, the hole accumulation layer is reduced by the formation of N_2 and H_2O reducing the concentration of oxygen ions. This results in the mitigation of the hole accumulation layer in each grain and the increase of the double Schottky barrier between TiO_2 grains. This diminution of oxygen ions on the surface of the TiO_2 material is represented as a downward band bending

(ΔQ_{inv}). As shown in Fig. 5.4(b), the decrease of the oxygen negative charges determines a decrease of the hole concentration resulting in the increase of the insulating core. This enables the reduction of valence band electron flow from grain to grain. As shown in Fig. 5.6(b), the decrease of bending of the valence band of the TiO_2 surface makes hole accumulation to decrease at the TiO_2/Al interface which makes the aluminum gate to become less positively charge. This will induce a reduction of the charge carries in the inversion channel, as shown in Fig. 5.6(b). As shown in Fig. 5.5(b), the chemisorption process on the TiO_2 surface leads to change in the work function of the TiO_2 surface and a modulation of the Schottky contact at the TiO_2/Al interface, thus directly shifting V_{th} due to the change in carrier density in the inversion layer. This band model agrees with experimental results and explains the positive threshold shift during ammonia exposure, as shown in Fig. 5.5(b).

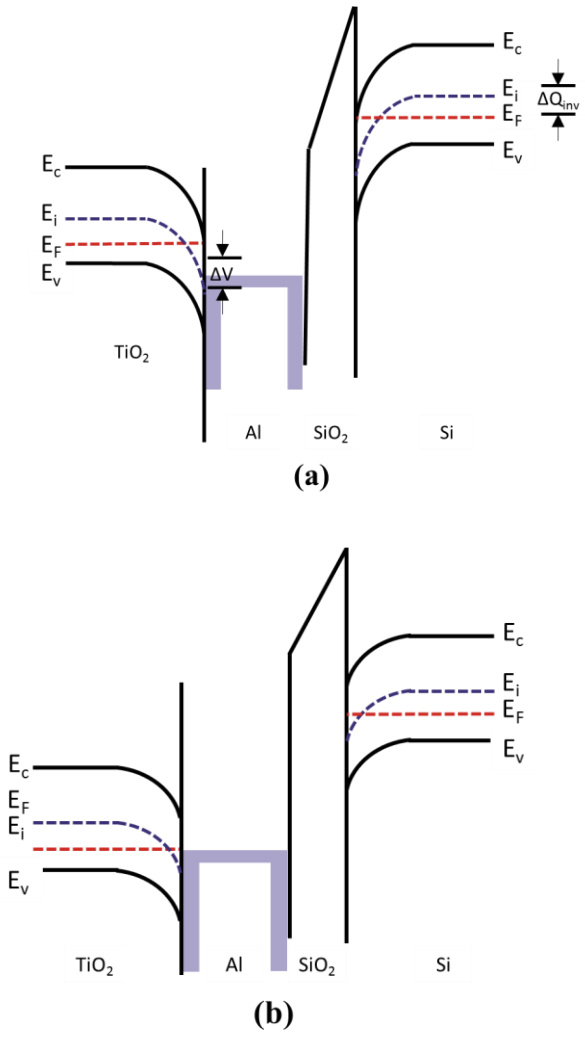

FIG. 5.6. Schematic energy diagram of the TiO_2-Al-SiO_2 -Si structure when $V_{gs} > V_{th}$. (a) Under exposure to air. (b) Under exposure to NH_3.

Gas molecules absorbed by the TiO_2 surface give arise to a change of the work function of the TiO_2 material which induces a change in carrier concentration in the inversion channel. As a first order approximation, the magnitude of the electron change in the inversion channel in air and ammonia can be defined as:

$$\Delta Q_{TiO_2-air} = C_{ox}WL(V_{gs} - V_{thAir}) \tag{5.15}$$

$$\Delta Q_{TiO_2-NH3} = C_{ox}WL(V_{gs} - V_{thNH3}) \tag{5.16}$$

where C_{ox} = Total channel capacitance, W = width of gate, L = Length of channel, V_{gs} = Applied gate voltage, V_{thAir} = Threshold voltage in air, V_{thNH3} = Threshold voltage in ammonia. The above equation can be further simplified using $\Delta V_{th\text{-}TiO2}$ as the voltage difference between air and ammonia to calculate charge contribution in the inversion channel due to the chemisorption of ammonia molecules in the TiO_2 surface as:

$$|\Delta Q_{inv}| = C_{ox} W L (\Delta V_{th-TiO2}) \tag{5.17}$$

For ChemFETs with multiwall TiO_2 nanotubes in this work, W = 30µm, L = 20µm (otherwise specified), and C_{ox} = 3.45x10^{-4} F/m^2 (t_{ox} = 100nm). Using V_{thNH3} and V_{thAir} shown in Fig. 5.5(b), Eq. 5.17 leads to $|\Delta Q_{inv}|$ = 2.07x10^{-14} C ~ 129375 electrons under 200 ppm ammonia. This in an indication that the charge carrier density changes in the inversion channel during the chemisorption of ammonia particle on the TiO_2 surface.

The chemisorption process of ammonia molecules on the TiO_2 surface of the nanowires leads to a change in the charge carrier density in the inversion channel. As described in Eq. 5.17, the change in charge carrier density in the inversion channel (ΔQ_{inv}) is directly proportional to the change in threshold voltage ($\Delta V_{th\text{-}TiO2}$). The charge transfer due to the chemisorption process could be explained with the following Eq:

$$f_{TiO_2} = \frac{\Delta Q}{\pi r_{AlGate} D_{TiO_2}} \tag{5.18}$$

where r_{AlGate} = radius of coverage of aluminum gate with TiO_2 nanowires, and D_{TiO2} = The TiO_2 nanostructure (nanowires or multiwall nanotube) density. For the current device, the aluminum gate pattering consist of a circumference with r = 25 µm which contains about 131 nanowires per µm^2. Assuming that there is a uniform charge across the TiO_2 nanowire, the electron transfer rate due to chemisorption of ammonia, f_{TiO2}, is 0.5 electron per multiwall TiO_2 nanotube.

The ChemFET with TiO_2 nanowires shown in Section-4.4 has the same *W*, *L*, and C_{ox} values as the ChemFET with multiwall TiO_2 nanotubes. However, the ChemFET with TiO_2 nanowires has a V_{thAir} = -1.05 V and V_{thNH3} = -1V (Fig. 4.10) in 200 ppm ammonia. This leads to $|\Delta Q_{inv}| = 1.04 \times 10^{-14}$ C ~ 64688 electrons and f_{TiO2} = 0.25 electron per TiO_2 nanowire. This an indication that by having multiwall TiO_2 nanotube configuration the electron transfer is 2x higher than a TiO_2 nanowire in the chemisorption process due to a higher surface area.

Chapter 6 OFC SAW Gas Sensor

The low-temperature (< 200 °C) nature of this nanostructure fabrication process allows it to be integrated with a variety of microelectronic materials and device types, including silicon based microelectronics, III-V semiconductors, flexible or smart material substrates, particularly for the fabrication of high-sensitivity sensors. While demonstrated using ZnO and TiO_2 as high-aspect ratio nanostructures sensing material as an active component of ChemFET gas sensors, the integrated thin film AAO template developed here can potentially be used to grow high aspect metal oxide nanostructures on SAW devices. This chapter is about the integration of multiwall TiO_2 nanotubes to an OFC SAW gas sensor devices.

6.1. Theory and Background of SAW Gas Sensors

Acoustic wave devices is a type of semiconductor sensors that could be used for probing the chemical and physical properties of materials in a simple, direct, and sensitive manner by using piezoelectric material as substrates to generate acoustic waves. The material type of substrate, crystal cut and the structure of electrodes determines the type of acoustic wave in the sensor. This type of sensor has been widely explored for many application in detecting chemical and biological components in a gas or liquid environment [7]. Acoustic wave chemical sensors usually rely on a reactive sensitive layer. Acoustic wave sensors are able to measure electrical and mechanical perturbations when the sensitive layer makes contact with a reacting agent. These changes could be detected by measuring the components of the acoustic wave: such as amplitude, velocity, and resonance frequency. Well stablished fabrication process, chemical inertness of the

substrate material, and high structural rigidity are the advantages that acoustic wave sensors have compared with other solid-state sensors. However, they also suffer from limitations in meeting requirements for all sensing applications with a single sensor design [91].

Thickness shear mode, Reyleigh and shear horizontal surface acoustic wave, acoustic plate mode, Love wave mode, and flexural plate wave are mayor classes of acoustic wave sensors. Nevertheless, Rayleigh-mode SAW-based devices have unique distinct acoustic and electrical properties that make them very promising for gas sensor applications. The major advantages of Reyleigh-mode SAW sensor are the simplicity of their construction and operation, low weight and low power requirements. In addition, this type of sensor relies mostly in a frequency shift which is highly reliable and very accurate phenomena [92].

Fig. 6.1 shows the simplest schematic of a SAW sensor with two terminals. It consists of a transmission (delay) line in which the acoustic (mechanical) wave is piezoelectrically launched from the oscillator, called the transmitter (T) [92]. This acoustic wave travels along the surface of the substrate and then it is transformed back into an electrical signal by the reverse piezoelectric effect at the receiving oscillator (R). In case of a chemical SAW sensor, the active reactive layer (selective layer) is located on the delay line region [93]. The interaction that the reactive layer has with the wave traveling along the delay line could be measured and related as attenuated amplitude (ΔA_v), as phase difference (delay) ($\Delta \Phi$), or as frequency shift (ΔF). In case of 126°YX $LiNbO_3$ wafers, the wave velocity is 3988 m/s and typical frequencies are in the range of 30-500 MHz. It worth pointing out that the traveling wave has mechanical and electrical character. This makes the selective layer change the properties of the traveling wave.

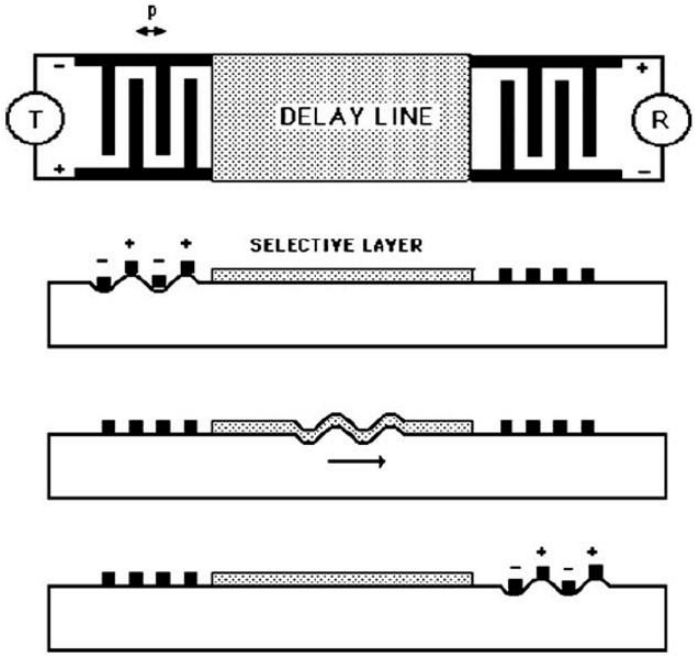

FIG. 6.1. Schematic diagram of a SAW oscillator [92].

The potential of SAW devices as chemical sensor is considerable. Integration of the low temperature fabrication process of high aspect ratio ZnO and TiO_2 nanostructures to a chemical SAW sensor has a considerable potential. Compared with a thin film, nanowires and nanotubes offer a superior increment in the reactive surface area. As seen on Chapter 4, growing nanowires and nanotubes of 1.7 μm in height and 40-90 nm in diameter results in an aerial density of $2.6x10^{10}$ nanotubes/cm^2 and a 220X increment in surface area compared with a standard flat film. In consequence, nanowires and nanotubes could be able to absorb more gas molecules than a thin film creating a SAW gas sensor with much better sensibility. As proof of concept, high aspect ratio multiwall TiO_2 nanotubes were integrated to the delay line of an OFC SAW device. Fig. 6.2 shows a schematic diagram of the integration of multiwall TiO_2 nanotubes to a SAW oscillator sensor using $LiNbO_3$ as a substrate. The next section will go over about the optimization of the fabrication process of the integration of multiwall TiO_2 nanotubes to the delay line of OFC SAW gas sensors.

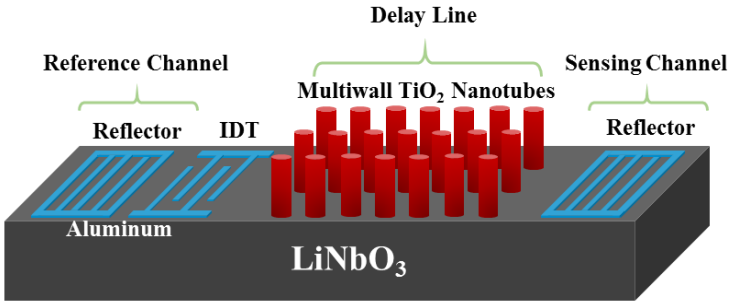

FIG. 6.2. Schematic of proposed SAW chemical sensor using integration of multiwall TiO_2 nanotubes as reactive layer.

6.2. Process Development & SAW Sensor Fabrication

While the fabrication process has been developed using ZnO, TiO_2 and a MOSFET structure, the selectively formed AAO template could be integrated with other microelectronic device structures that can incorporate an aluminum film deposition such SAW devices on $LiNbO_3$ substrate. Empty pores of about 1μm in height and 100 nm width were fabricated on a silicon substrate by a combination of the multistep anodization and barrier layer removal process on top the gate of a MOSFET described previously in Chapter 3. We have optimized the same high-aspect ratio metal oxide nanostructure fabrication process to integrate multiwall TiO_2 nanotubes to the delay of an OFC SAW gas sensor on a $LiNbO_3$ substrate. The overall multiwall TiO_2 nanotube fabrication sequence is shown in Figs. 6.3(a)-(d), where each figure shows a schematic cross section of the process. The fabrication of multiwall TiO_2 nanotubes use a combination of aluminum deposition, aluminum anodization, TiO_2 and Al_2O_3 ALD, sputtering plasma etching, and wet etching. The fabrication process is in sharp contrast with the ZnO nanowire, TiO_2 nanowire and multiwall TiO_2 nanotube fabrication process for ChemFETs. However in this case, the aluminum layer on the bottom of the AAO template was totally consumed by the optimization of the barrier layer aluminum anodization step.

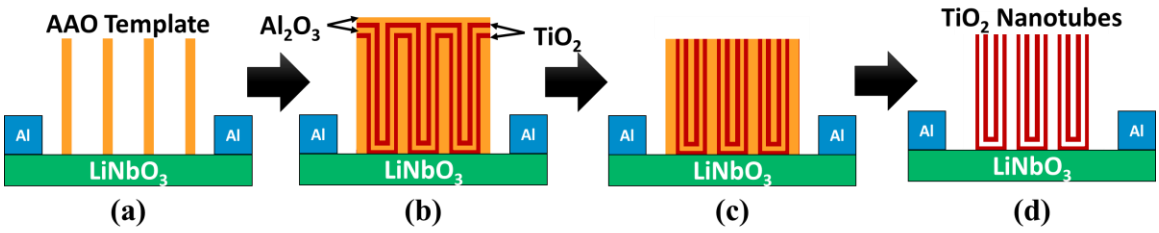

FIG. 6.3. Sketch of fabrication steps of free standing multiwall TiO_2 nanotubes on delay line of an OFC SAW gas sensor. (a) Empty AAO template after the multistep anodization process. (b) AAO filled with TiO_2 and Al_2O_3 by ALD. (c) AAO template exposed after sputtering plasma etch of Al_2O_3/TiO_2 overlaying. (d) Free standing TiO_2 nanotubes in direct contact with $LiNbO_3$ substrate after wet etching of AAO template and ALD Al_2O_3.

6.2.1 Template Fabrication Optimization for SAW devices

Direct contact between nanowires and bulk substrate using the previously reported high-aspect metal oxide nanostructure fabrication process could be challenging. Chemisorption of air and ammonia molecules of the multiwall TiO_2 nanotubes during gas exposure will be the same with an aluminum layer underneath the nanotubes, but it might add an energy loss to the propagating acoustic wave. For optimum propagation of the acoustic wave, the bottom of nanotubes should be in direct contact with the substrate since most of the SAW propagation energy is located right on the top surface of the $LiNbO_3$ substrate.

There are two possible ways to remove the aluminum underneath the nanotubes: (1) Doing a long 3rd anodization, and (2) Optimization of Stage 1 of the barrier layer removal aluminum anodization process. A long 3rd aluminum anodization approach converts the entire aluminum layer left from previous anodizations into an AAO template. Table 6.1 describes the anodization steps of a 2.5 µm aluminum film on a $LiNbO_3$ substrate in 3% oxalic acid at 40 V. Anodizations I and II were followed by an alumina wet etch

with chromic/phosphoric acid for 12 hours at 70°C. The final aluminum thickness after anodizations I and II was measured about 1.4µm. Fig. 6.4 (a) shows the current/time characteristics of the long anodization the final 1.4 µm aluminum layer of the 3rd anodization. Experiments have shown that aluminum anodization has a rate of aluminum consumption rate of ~120 nm/min. However, as shown in Fig. 6.4, after the first 11 minutes current level was still high as an indication that a thin aluminum film was still present at the bottom of the template. For that reason, we added an over anodization step to make sure the aluminum consumption was completed. Fig. 6.4 shows a clear indication that the current reaches down after around 16 minutes. We have added extra 8 minutes for a complete consumption of the aluminum layer underneath the AAO template.

Anodization	Voltage	Time
I	40 V	8 min
II	40 V	8 min
III	40 V	16 min w/ 8 min over anodization

Table 6.1. Anodization conditions of a 2.5 µm starting aluminum film.

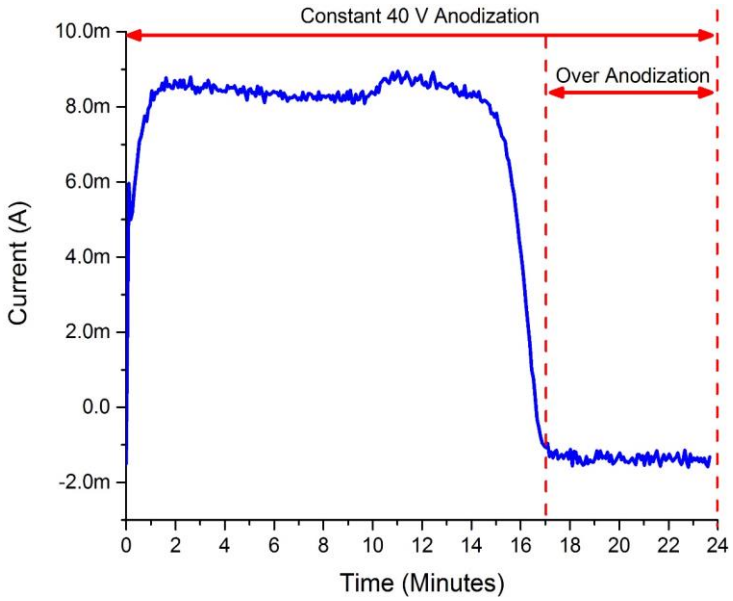

FIG. 6.4. Current vs. time characteristics of long aluminum anodization at 40V in 3% oxalic acid adapted in anodization III.

The barrier layer removal anodization process (Section 3.1) leaves an aluminum layer underneath the AAO template after the tree stage process. Another way to remove the underlying aluminum layer for direct contact of TiO_2 nanotubes with $LiNbO_3$ substrate is by the optimization of Stage 1 of the barrier layer removal anodization process. Stage 1 optimization could be possible by taking into consideration the aluminum consumption during an anodization process (~120 nm aluminum/min.). For the present work, anodizations I and II were conducted in 3% oxalic acid at 40V for 8 minutes each with a subsequent 12 hours 70°C alumina wet etch using the chromic/phosphoric acid solution after each anodization. The starting aluminum film was about 2.4 μm while the end thickness after anodization I and II was about 1.4 μm. By taking into consideration the final thickness after the first two anodizations, one can calculate the anodization time of each of the stages of barrier layer removal aluminum anodization process. The goal with this process is to leave a very thin layer (10nm) alumina barrier layer at the bottom of the pores that could be easily etch with 5% phosphoric acid. However, optimization the duration of Stage 1 was very puzzling due to the fact that the thickness is not uniform across each sample. The thickness could vary about 100 nm across samples due to the nature of e-beam evaporation process. Each sample required a different time for Stage 1. This is a disadvantage over the 3rd long anodization process where a simple long anodization takes care of the consumption of the entire aluminum film. Table 6.2 describes the anodization conditions of the barrier layer removal aluminum anodization of a 1.4 μm final aluminum thickness. Stage 1 corresponds to a 15 minute anodization at 40 V, while Stage 2 corresponds to gradual voltage decrease at a 0.1V/sec rate until a 9 V reach point. Stage 3 is a 9V 45 minute anodization step. Fig. 6.5 shows the current vs. time characteristics of a

barrier layer removal aluminum anodization process of a 1.4 µm aluminum layer with an optimized Stages 1-3. Stage 1 is where most of the aluminum film gets consumed at the bottom of the pores. Stage 2 was started 1 minute before the current reach all the zero amps and it was ended once the voltage step reached 9 V. The low voltage anodization of Stage 3 lasted 45 minutes to make sure that any aluminum layer at the bottom of the pores gets consumed.

Stage	Voltage	Time
1	40 V	15 min
2	40 V to 9V @ 0.1 V/sec	5 min, 10 sec
3	9 V	45 min

Table 6.2. Barrier layer removal aluminum anodization conditions

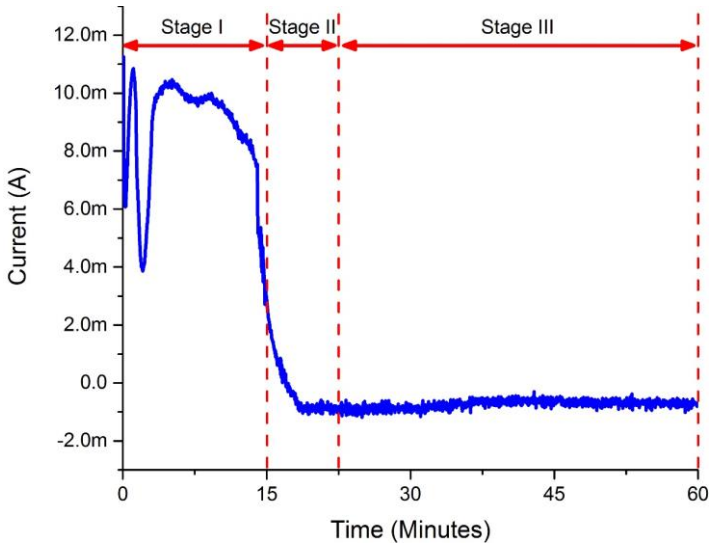

FIG. 6.5. Current vs. time characteristics of barrier layer removal aluminum anodization.

The final thickness after the anodization I and II, and the condition of the electrolyte are critical anodization conditions for optimum consumption of the aluminum layer at the bottom of the AAO template using the barrier layer removal aluminum anodization approach. These conditions are not critical for the long 3rd anodization approach since the

over anodization of a sample does not have any penalty. After template fabrication with complete consumption of the aluminum layer, samples were subject to a 90 min bath in 5% H_3PO_4 for 40nm to 100 nm pore enlargement and etching of thin barrier layer on bottom of the pores.

6.2.2 Multiwall TiO_2 Nanotube Fabrication for SAW devices

AAO templates fabricated by the barrier layer removal step anodization and the 3rd long anodization processes were filled with a sequential TMA, and TDMAT ALD. Table 6.3 shows the ALD recipe used for multiwall TiO_2 nanotubes fabrication on $LiNbO_3$ at 200°C. Note that the first and third nanotube wall correspond to 293 pulses of TDMAT while the second and fourth walls correspond to 93 TMA pulses each. In this case the AAO template is filled with 10 nm TiO_2, 10 nm Al_2O_3, 10 nm TiO_2 and 10 nm Al_2O_3 leaving a 40 nm over layer on top of the AAO template. By controlling the number of ALD pulses, one can further choose the thickness of each wall material.

Wall #	Instruction	Number of Pulses	Resulting Thickness
1	TDMAT 0.1 sec pulse	293	10 nm
	DI water 0.015 sec pulse		
2	TMA 0.015 sec pulse	93	10 nm
	DI water 0.015 sec pulse		
3	TDMAT 0.1 sec pulse	293	10 nm
	DI water 0.015 sec pulse		
4	TMA 0.015 sec pulse	93	10 nm
	DI water 0.015 sec pulse		

Table 6.3. ALD recipe of multiwall Tio2 nanotubes for SAW gas sensors.

Etching of the 40 nm TiO_2/Al_2O_3 over layer was achieved using argon sputtering plasma at 300 W for 19 minutes, with a TiO_2/Al_2O_3 conjunctional etch rate of ~ 2 nm/min.

Figs. 6.6(a)-(d) show the AAO templates fabricated by the long 3rd anodization and the barrier layer removal step anodization approaches filled with TiO_2/Al_2O_3 ALD after 19 minutes of argon sputtering plasma over layer etch. Figs. 6.6(a)-(d) show no visible aluminum layer at the bottom of the pores suggesting that total consumption of the aluminum layer was successfully achieved using either the long 3rd anodization approach and the barrier layer removal step anodization approach. Argon sputtering plasma over layer etch reveals the top of the AAO template and sacrificial ALD Al_2O_3 walls allowing the subsequent nanotube release step.

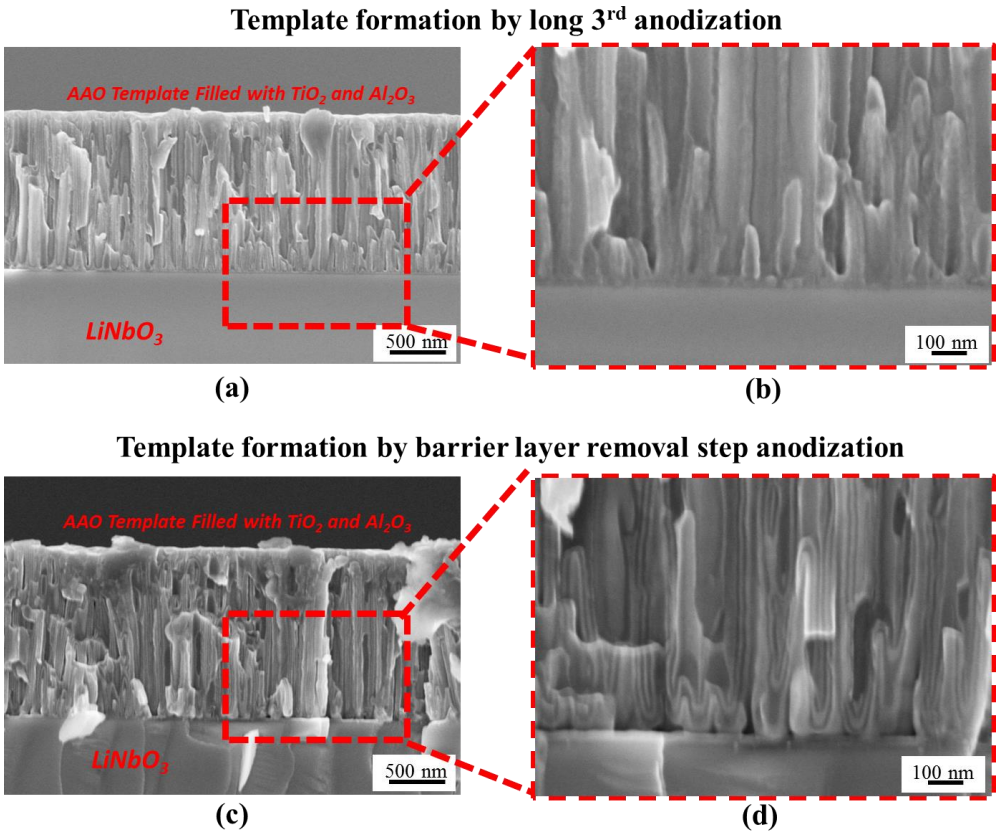

FIG. 6.6. Cross section SEM images of AAO templates filled with TiO_2 and Al_2O_3 ALD. (a) AAO template fabricated using the long 3rd anodization approach (b) Zoomed in image of selected area in (a). (c) AAO template fabricated using the barrier layer removal step anodization approach. (d) Zoomed in image of selected area in (b).

6.2.3 Multiwall TiO_2 Nanotube Release for SAW Gas Sensors

Since the AAO template and Al_2O_3 walls are exactly the same material, the same chromic/phosphoric acid solution (0.2 wt% H_2CrO_4 & 0.4 wt.% H_3PO_4) used in the TiO_2 nanowire release process was used again to release the nanotubes from the template and sacrificial layers. AAO templates filled with TiO_2 and Al_2O_3 fabricated using the 3rd long anodization approach, and the barrier layer removal step anodization approach were subject to a 16 hour alumina etch at 70 °C in the chromic/phosphoric acid solution. The multiwall TiO_2 nanotubes released from the AAO template fabricated by the barrier layer removal multistep anodization approach are shown in Figs. 6.7(a)-(c). Fig. 6.7(a) shows defects at the bottom of the nanotubes. This is an indication that the optimization of Stages 1, 2, and 3 of the barrier layer removal step anodization process was not optimal for direct contact between TiO_2 nanotubes and $LiNbO_3$ substrate. Figs. 6.7(b)-(c) also shows defects on top of the nanotubes. This indicates that Stage 3 creates deformities on top of the pores due to the nature of the anodization process. This is not optimal for high nanotube formation uniformity. Note that the chromic/phosphoric acid solution did not degrade the TiO_2 surface.

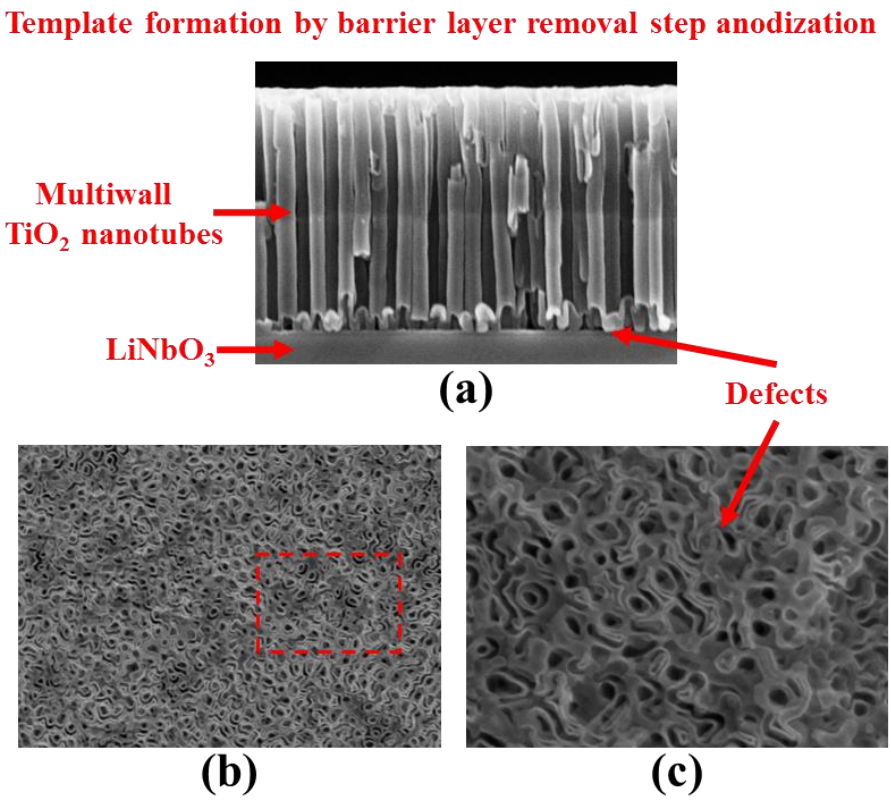

FIG. 6.7. SEM images of multiwall TiO_2 nanotubes released from an AAO template fabricated by the barrier layer removal multistep anodization approach after 16 hours in the chromic/phosphoric acid solution. (a) Cross section view showing defect formation at the bottom of the nanotubes. (b) Top-view of the nanotubes with random uniformity formation of defects. (c) Zoomed-in image of selected area in (b).

In contrast, the nanotubes released from the AAO template fabricated using the 3rd long anodization approach are shown in Figs. 6.8(a)-(d). The nanotubes were release using the chromic/phosphoric acid at 70 °C for 16 hours. Figs. 6.8(a)-(b) show no evidence of defects at the bottom of the pore, and direct contact between TiO_2 nanotubes and $LiNbO_3$ substrate. Figs. 6.8(a)-(b) also show that the TiO_2 nanotubes have a diameter of 100 nm and a height of 1.8 µm as expected from long 3rd anodization process. High nanotube uniformity formation is also shown in Fig. 6.8(c)-(d). It also shows that the inner nanotube

has a diameter of 40-50 nm across the layer. The resulting TiO_2 nanotube layer has 2X the areal density than the TiO_2 & ZnO nanowire film (26 billion nanotubes/cm^2) which results in a 202X increment in surface area compared with a TiO_2 thin film counterpart.

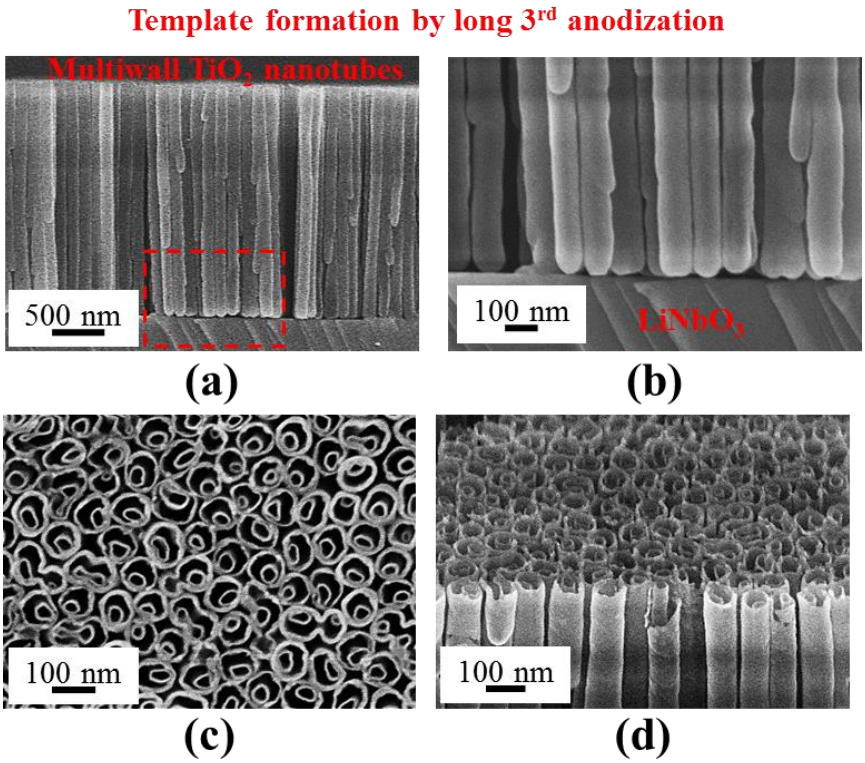

FIG. 6.8. SEM images of multiwall TiO_2 nanotubes released from an AAO template fabricated by the long 3rd anodization approach. (a) Cross section view of TiO_2 nanotubes with 1.8 μm in height and 100 nm in diameter. (b) Zoomed in image of selected area in (a). (c) Top-view. (d) Tilted-view

Defects at the bottom and top of the nanotubes indicate that the template fabrication using the barrier layer removal multistep anodization process is not ideal for applications where a direct contact between nanowire/nanotube and substrate is needed. In contrast, high uniformity TiO_2 nanotubes in direct contact with the substrate were successfully achieved by the fabrication of AAO templates using the 3rd long anodization approach.

6.2.4 Characterization of Multiwall TiO_2 Nanotubes on $LiNbO_3$

AAO templates filled with TiO_2 and Al_2O_3 after 19 minutes in argon sputtering overlaying etch were analyzed using a Hitachi SU-70 equipped with an EDX system to evaluate the chemical composition from a top view of an AAO template fabricated with the 3rd long anodization approach. Fig. 6.9 shows the EDX measurement that displays peaks coming from Carbon K_a = 0.27 keV, Titanium L_a = 0.52 keV, Oxygen K_a = 0.53 keV, Aluminum K_a = 1.49 ke, Titanium K_a = 4.52 keV and Titanium K_b = 4.93 keV. Elemental chemical quantification was also obtained showing atomic percentages from Carbon 2.75%, Oxygen 54.41%, Aluminum 27.48%, and Titanium 30.66% implying that the AAO template was successfully filled with a dense composition of TiO_2.

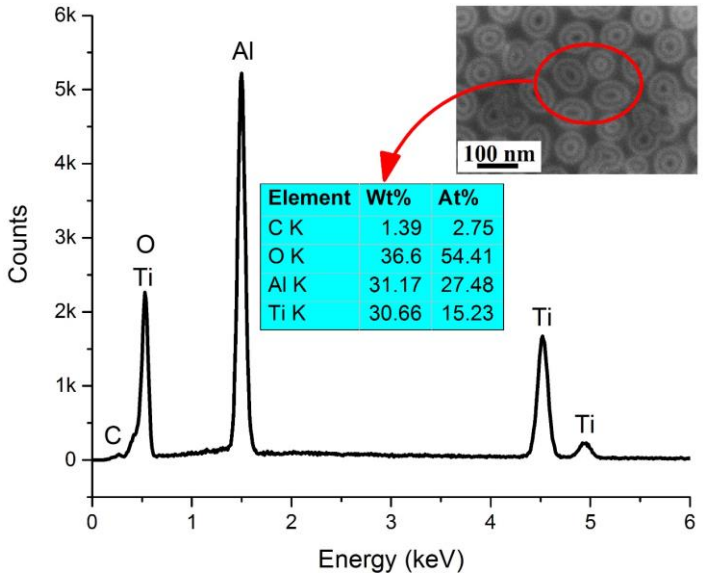

FIG. 6.9. EDX measurement of an AAO template filled with TiO_2 and ALD Al_2O_3 after 19 minutes argon sputtering over layer etch. The spectra is taken from the indicated location on the inset top-view SEM of the filled AAO template

6.2.5 Integration of Multiwall TiO_2 Nanotubes to OFC SAW Gas Sensors

For integration into OFC SAW device, it is most useful to be able to form TiO_2 nanotubes selectively, i.e, form them at the desired locations, but leaving the remaining aluminum film for IDT and reflectors while also consuming the aluminum at the bottom of the pores. Because the anodization process requires an applied potential, it is straightforward to pattern the aluminum layer, forming contacts for anodizing only specific regions. However, as part of the pore enlargement process, samples are subjected to 5% H_3PO_4 for 90 min after the anodization process. This alumina etching process also etches the aluminum IDT and reflectors. After 90 min in 5% H_3PO_4, a 100 nm aluminum thick etches completely. The selectivity can be further enhanced by the addition of a masking layer, such as photoresist, as a protective layer to allow anodization in the desired regions only, leaving IDT and reflectors intact.

This approach was used to selectively anodize the delay line of an OFC SAW gas sensor leaving IDT and reflectors intact after the pore enlargement step. Fig. 6.10 shows a sketch of the fabrication sequence to integrate multiwall TiO_2 nanotubes to the delay line of an OFC SAW gas sensor. The fabrication sequence starts with a 2.7 μm e-beam evaporated aluminum deposition on a $LiNbO_3$ wafer followed with a metal lithography step of the reactive layer of the SAW device. Anodization I is conducted in 3% oxalic at 40V for 8 minutes followed by an alumina etch for 70 °C in a chromic/phosphoric acid solution for 24 hours. Then, a 100 nm aluminum deposition using a magnetron sputtering system is performed. Standard metal lithography of IDT and reflectors is achieved with a 4μm resolution. Anodization II was performed using the same conditions as anodization I after the 2^{nd} metal lithography followed by an alumina etch. Note that the 100 nm aluminum

previously deposited on the reactive layer will be consumed during anodization II and will not affect the pore uniformity formation of the final AAO template. Anodization III is then performed for 24 minutes after the IDT and reflectors were protected with photoresist. This leaves an AAO template with 1.8 µm in height and 40 nm pore diameters. Samples were then subjected to 5% H3PO4 for 90 minutes for pore enlargement from 40 nm to 100 nm, and alumina barrier etch at the bottom of the pores. The photoresist acts as a protective layer so the 100 nm aluminum for IDT and reflectors will not etch away with H_3PO_4. Photoresist is stripped using acetone, IPA and DI rinse after pore enlargement step. This leave a 1.8 µm AAO template with 100 nm pores without a barrier layer at the bottom of the pores on the delay on the SAW device. Samples were immediately followed by a sequential 200°C ALD of TiO_2 and Al_2O_3 using TDMAT, TMA and DI water precursors. This leaves a 40 nm TiO_2/Al_2O_3 over layer which is etch away using an argon sputtering system for 19 minutes. The TiO_2 nanotubes are released from the AAO template and Al_2O_3 ALD sacrificial layer using the chromic/phosphoric acid solution at 70 °C for 14 hours. This fabrication sequences leaves free standing multiwall TiO_2 high-aspect ratio nanotubes in direct contact with the substrate on the delay line of an OFC SAW gas sensor.

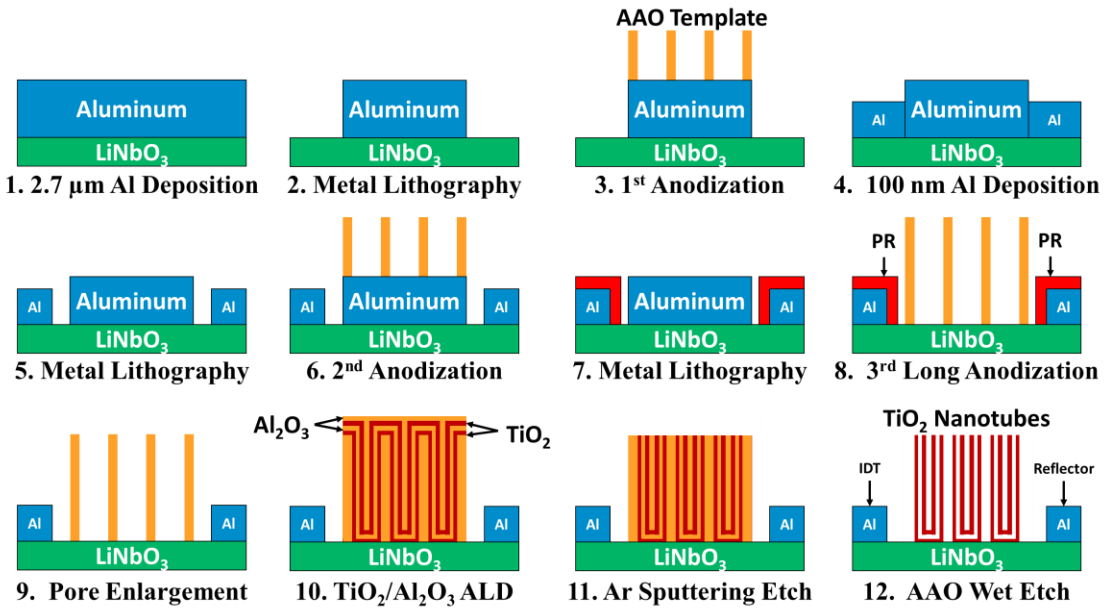

FIG. 6.10. Sketch of fabrication steps of free standing multiwall TiO2 nanotubes on delay line of an OFC SAW gas sensor. Process consists of a combination of aluminum depositions, aluminum anodizations, ALD, sputtering plasma etch and, chemical wet etch.

This fabrication sequence approach was adapted to form an integrated OFC SAW gas sensor. Fig. 6.11 shows a large optical view of the final structure of the device. The SAW layout has been designed with the objective to test the OFC SAW gas sensor surrounded of various concentrations of ammonia at room temperature. The SAW layout consists of an input of 20 interdigital transducers (IDT) with three sets of reflectors of 160 pieces in the reference channel, and three reflectors of 160 pieces in the sensing channel. IDTs and reflectors have a pitch of 4 µm. The OFC SAW device has three un-anodized aluminum reflectors on the reference and sensing channel, un-anodized aluminum IDT, and a reactive multiwall TiO_2 nanotube layer on a 128° YX $LiNbO_3$ substrate. The OFC SAW layout was designed using 228 MHz as center frequency. Reflectors 1, 2 and 3 corresponds to an interrogation frequency of 223.6 MHz, 228.8 MHz and 234.2 MHz respectively. The reflectors and IDT have an un-anodized aluminum thickness of 100nm.

Multiwall TiO_2 nanotubes of 100 nm and 40 nm in diameter, and 1.8 μm in height are integrated in direct contact with the $LiNbO_3$ substrate on the delay line. The dimension of the selective layer is 8.5 mm x 1.5 mm in the delay line and the total chip size is 18.75 mm wide and 2.5 mm long.

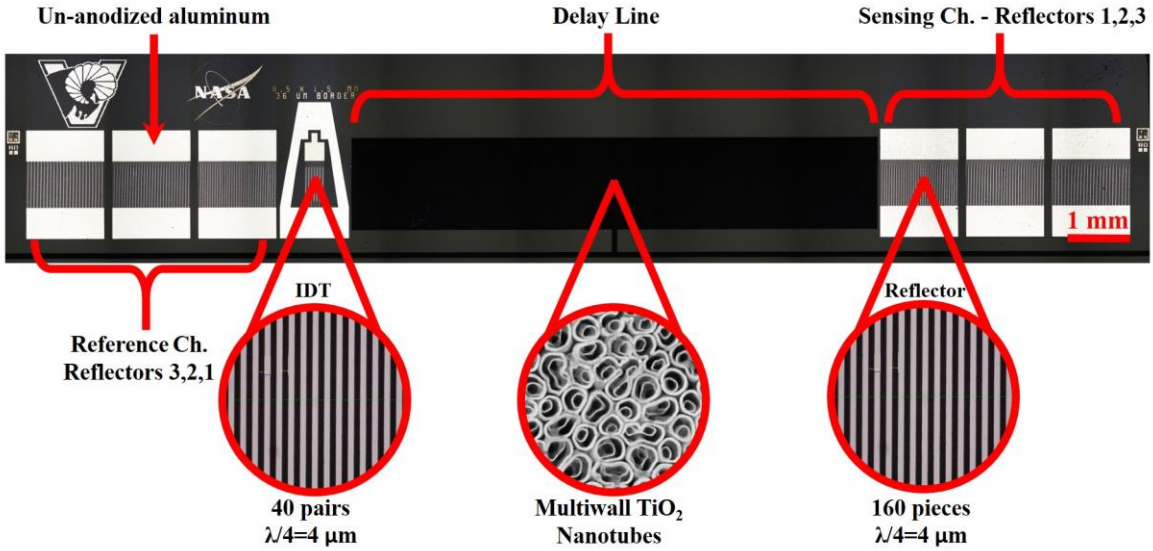

FIG. 6.11. Large optical view of an integrated OFC SAW gas sensor.

6.3. OFC SAW Gas Sensor Testing

The electrical response of the OFC SAW gas sensors with high-aspect ratio multiwall TiO_2 nanotubes were examined using ammonia gas with concentrations ranging from 25-200 ppm, diluted with synthetic air (20% oxygen and 80% nitrogen). The SAW sensor layout was specially designed to be assemble and tested using a H16 stainless steel package from Mini Circuits Inc. The gas sensor chip was bonded to the base plate of the package using a strain gage adhesive (Omega's TT330). Then, it was wire bonded to the chip package using copper bondable terminal pads for ground and signal terminals as shown in Figs. 6.12(a)-(b). All experiments were conducted using an Agilent E8356A PNA Series Network analyzer.

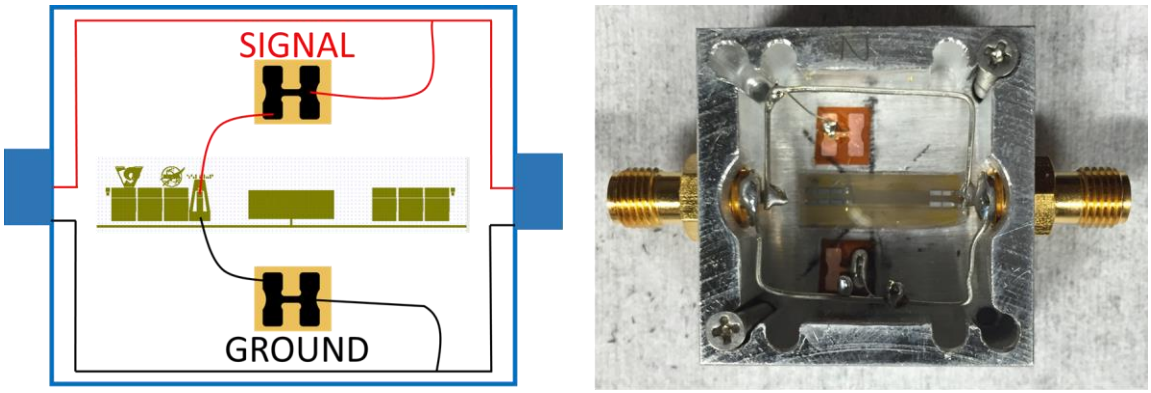

FIG. 6.12. Gas sensor chip assembly by wire bonding in a stainless steel package. (a) Sketch of wire bonded signal and ground connection. (b) Actual image of SAW device bounded to the base of the package connected to bondable terminal pads.

OFC SAW gas sensors with multiwall TiO_2 nanotubes were tested using different concentrations of ammonia gas. Mass flow controllers were used to adjust the ammonia concentration. The SAW gas sensor device was installed in a 400 ml sealed chamber and all experiments were conducted at room temperature (20°C). The total flow was kept constant at 500 sccm throughout the experiment. The chip package was inserted inside a custom made gas air tight chamber during testing of sensor, as shown in Fig. 6.13.

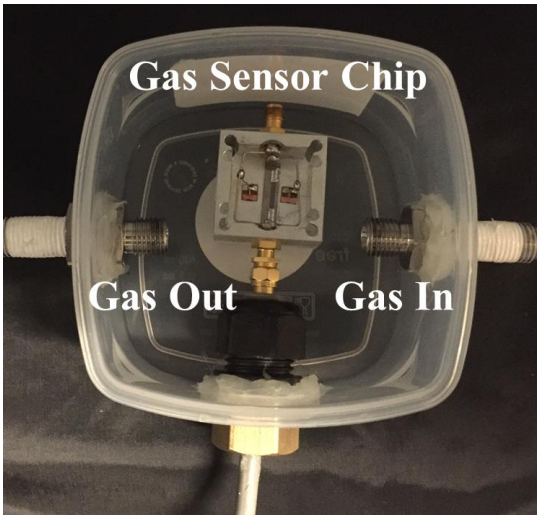

FIG. 6.13. Chip package inserted in a 400 ml gas testing chamber.

Initial testing was carryout to verify if the multiwall TiO_2 nanotubes were actually modifying the characteristics of the SAW without any ammonia present. We compared the full device characteristics of a non-nanotube (Fig. 6.14(a)), and a nanotube device (Fig. 6.14(b)) using the |S11| transducer response of each chip. Figs. 6.14(a)-7(b) indicate that the frequency spectrum of the non-nanotube device has more frequency complex data points than the frequency spectrum of the nanotube device due to the fact that there are no obstructions on the delay line for the traveling wave to move freely along the surface of the $LiNbO_3$ substrate. It is evident that the multiwall TiO_2 nanotubes have profoundly affected the characteristics of the acoustic wave even without any ammonia present.

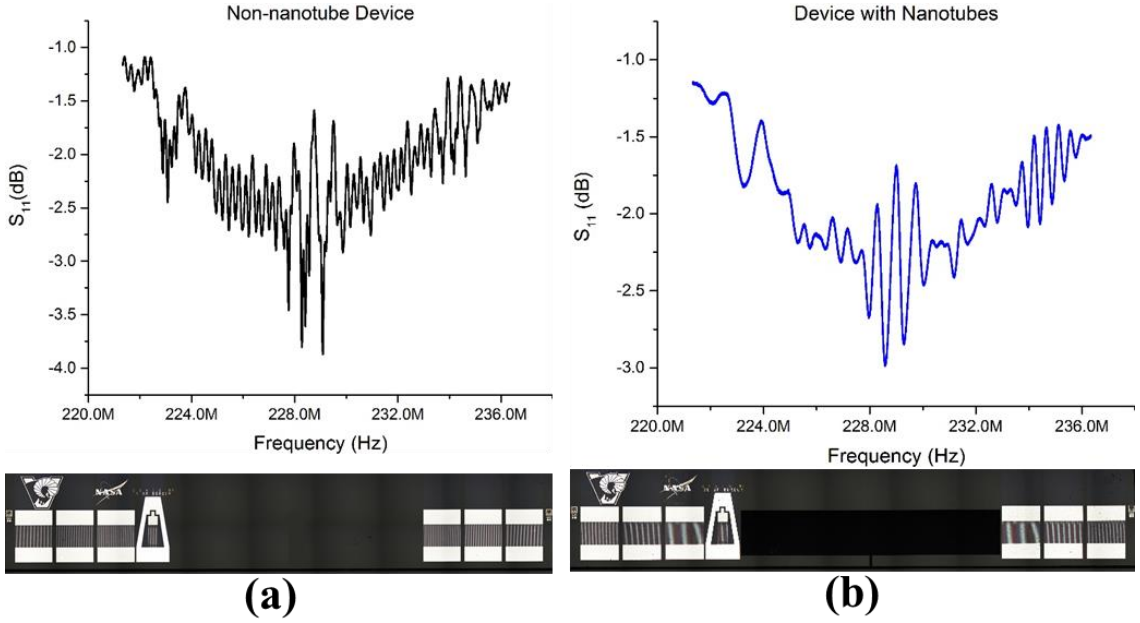

FIG. 6.14. Frequency response of OFC SAW devices using |S11| measurements. (a) Non-nanotube device. (b) Nanotube device with 8.5 mm x 1.5 mm TiO_2 nanotube reactive area on delay line.

In addition, the time response of the non-nanotube and nanotube devices gating the reference and sensing channel were investigated to further verify the impact of the multiwall TiO_2 nanotubes has on the characteristics of the traveling wave without the present of ammonia. Fig. 5.15(a) indicates that there is no variation in the time response of both devices in the reference channel due to the fact that there are no TiO_2 nanotubes on the path of the traveling wave in the reference channel. Fig. 5.15(a) also shows that reflectors one(f_1), two(f_2), and three(f_3) have different periodicity. On the other hand, Fig. 5.15(b) shows that the time response of the nanotube device has suffered a magnitude loss while the time response of the non-nanotube device was unaffected in the sensing channel. This is an indication that the multiwall TiO_2 nanotube are indeed changing the characteristics of the traveling wave in the sensing channel of the nanotube device without the present of ammonia. Figs. 5.15(a)-(b) also indicate that the sensor response comes from the reflectors of the sensing channel from 4.09 µsec – 7.07 µsec.

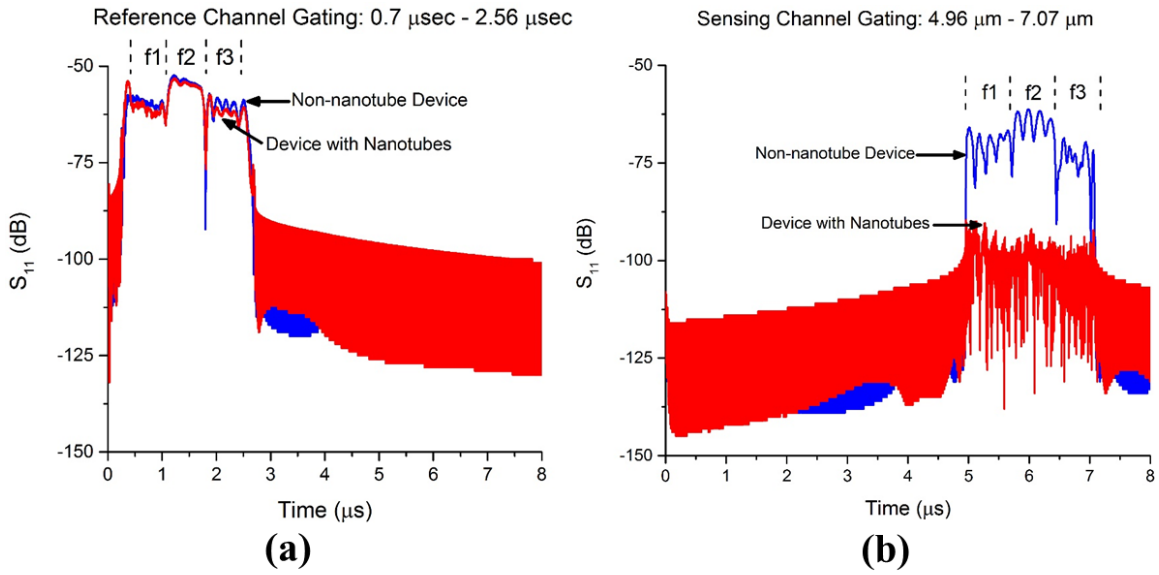

FIG. 6.15. Time response of the three reflectors using |S11| measurements. (a)Reference channel. (b) Sensing channel.

The electrical response of the OFC SAW gas sensor with high-aspect ratio multiwall TiO_2 nanotubes on the delay line was examined using ammonia gas concentrations ranging from 25 ppm to 200 ppm, diluted with synthetic air (20% oxygen and 80% nitrogen). The device was installed in a 400 ml sealed chamber and all experiments were conducted at room temperature (20°C). The total flow was kept constant at 500 sccm throughout all experiments. The transient response of the non-nanotube and nanotube OFC SAW gas sensor devices were measured in the frequency domain by gating the sensing channel reflectors (4.96μm – 7.07μm). By comparing the electrical response from both devices, and gating the sensing channel reflectors, we were certain that the measured electrical response only corresponded to the multiwall TiO_2 nanotubes on the delay line. Samples were first subjected to 1 min air for equilibrium stabilization, and then to 100 ppm ammonia exposure for 60 min. The ammonia source was then switched off and exposed to clean dry air for 90 minutes. By taking into consideration the lowest peak of the frequency spectrums during the air stabilization, 100 ppm ammonia, and air recuperation, a variation of the frequency and amplitude components is evident during the transient response of the non-nanotube and nanotube devices, as shown in Figs. 6.16(a)-(b). For simplicity purposes, variations of the frequency and amplitude components during the complete transient response were analyzed individually in Fig. 6.17 and Fig. 6.18.

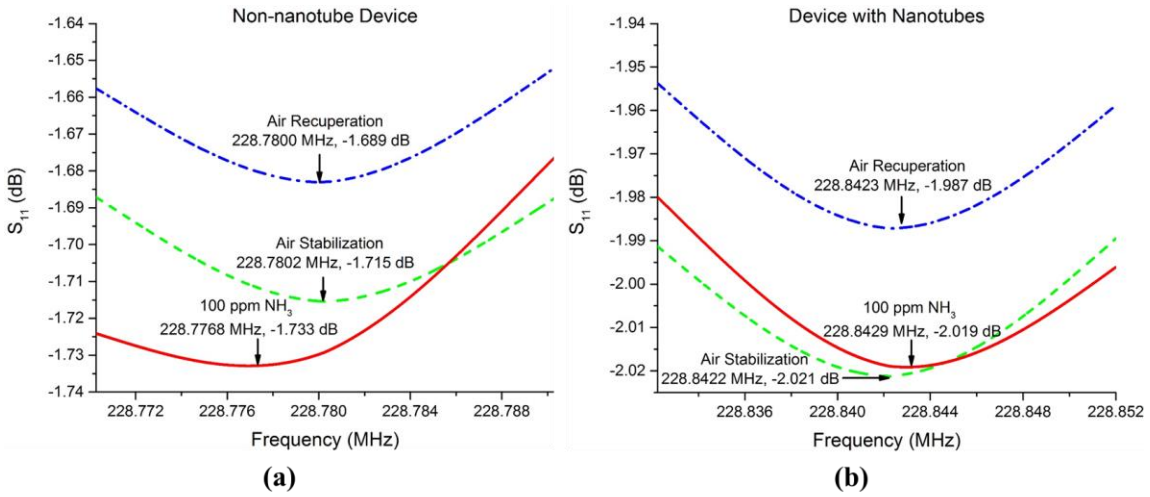

FIG. 6.16. Frequency response of OFC SAW devices using |S11| measurements and gating sensing channel reflector after 1 min air stabilization, 60 min exposure to 100 ppm ammonia, and 90 min in dry air for recuperation. (a) Non-nanotube device. (b) Nanotube device.

Fig. 6.17 indicates that there is a positive frequency shift of the nanotube device and a negative frequency shift of the non-nanotube device during exposure to ammonia gas and air. Both devices reach a recuperation point after 90 min in air after the ammonia gas was switched-off. The frequency variation of the OFC SAW gas sensor under exposure to 100 ppm ammonia can be explained by taking into account the mass, viscoelastic and acoustoelectric loadings during SAW propagation in the following equation [94-99]:

$$\Delta f = -c_m f_o \Delta\left(\frac{m}{A}\right) + 4c_e f_0 \Delta(hG') - \frac{K^2}{2}\left(\frac{1}{1+v_o^2\Delta\left(\frac{C_s}{\sigma_s}\right)^2}\right) \quad (6.1)$$

where C_m= mass sensitivity coefficient; f_o = initial resonant frequency; m/A = change of mass per unit area; c_e= elasticity coefficient; h= thickness of reactive layer; G'= shear modulus; k^2= electromechanical coupling coefficient of substrate; C_s = capacitance per unit length; σ_s= sheet conductivity of sensitive layer; and v_o= SAW velocity. The three terms of Eq. 6.1 indicate the contributions of changes in mass, viscoelastic and acoustoelectric

loading respectively, to the variation in SAW resonant frequency. The acoustoelectric loading corresponds to the chemisorption of oxygen on the surface of the TiO_2 nanotubes followed by charge transfer during the reaction of chemisorbed oxygen with the ammonia gas. When a p-type metal oxide layer is exposed to a reducing gas (e.g. ammonia) the conductivity of the film decreases resulting in an increase in acoustic wave velocity, thereby increasing the resonant frequency [98, 100-104]. As the nanotubes on the delay line of the OFC SAW device are made of p-type TiO_2, the conductivity of the film decreases resulting in a positive frequency variation when exposed to ammonia. However, the acoustoelectric effect causes only significant changes to the propagation wave when the film resistivity is relative high (3 to 10^4 Ω-cm) or in bi-layer structures (semiconductor + metal) [94, 104-107]. Despite the decrease of conductivity of the TiO_2 nanotube array during the exposure to ammonia gas, the acoustoelectric loading is insignificant due to the fact that the film resistivity of the reactive layer is relative small and it is not a by-layer structure. Furthermore, from the frequency variation equation (Eq. (6.1)), the positive frequency response of the nanotube device in Fig. 6.17 also occurs when the viscoelastic loading of the multiwall TiO_2 nanotube layer significantly increases and exceeds the change of mass and acoustoelectric effects, making the viscoelastic loading the dominant factor of the electrical response. Therefore, the positive frequency shift indicates that the modification of viscoelastic loading of the multiwall TiO_2 nanotube layer is the dominant effect for the positive variation of the SAW oscillation frequency during exposure to 100 ppm ammonia. On the other hand, the negative frequency shift of non-nanotube device during the exposure to ammonia gas corresponds to mass loading on the delay line. This mass loading might be coming from the ammonia particles sitting on the delay. The

positive frequency variation of the non-nanotube device in air is an indication that the ammonia particles are being removed from the delay line. The negative frequency shift of the nanotube device in air shows that the viscoelastic loading properties of the TiO_2 nanotubes are recuperating its original characteristics.

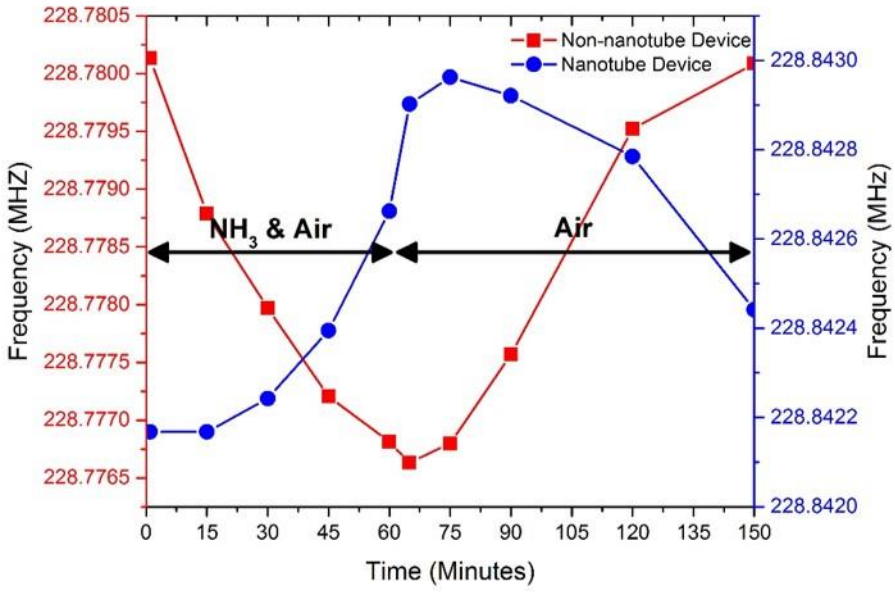

FIG. 6.17. Frequency shift transient response of non-nanotube and nanotube OFC SAW gas sensors using |S11| measurements and gating sensing channel reflectors from 4.96 µm - 7.07 µm.

Fig. 6.18 shows the amplitude variation of the non-nanotube and nanotube OFC SAW devices during exposure to 100 ppm ammonia and air. As shown in Fig. 6.18, the amplitude of the non-nanotube device decreases while the amplitude of the nanotube device stays pretty much constant during exposure to the ammonia gas. Amplitude loss is mainly an indication of increase in mass and/or acoustoelectric loading which is accompanied with a decrease in resonant frequency of the SAW [108, 109]. Therefore, the addition of ammonia particles on the delay line of the non-nanotube devices is the main

factor for the amplitude loss during the exposure to 100 ppm ammonia. On the other hand, the constant amplitude shift of the nanotube device is an indication that mass and acoustoelectric loadings are insignificant. This is another indication that, according to Eq. 6.10, the viscoelastic loading dominates the sensing response since the mass and acoustoelectric loading of the TiO_2 nanotube layer on the delay line are negligible during exposure to 100 ppm ammonia. Fig. 6.18 also shows that once the ammonia is switched off, both devices undergo an amplitude gain. The amplitude of the non-nanotube device increases in the air as an indication that the ammonia particles are being removed from the delay line decreasing the mass loading and increasing the resonant frequency of the acoustic wave. The amplitude gain of the nanotube device in air indicates that the SAW resonant frequency is also increasing, however in this case, due to a decrease in viscoelastic loading of the multiwall TiO_2 nanotubes.

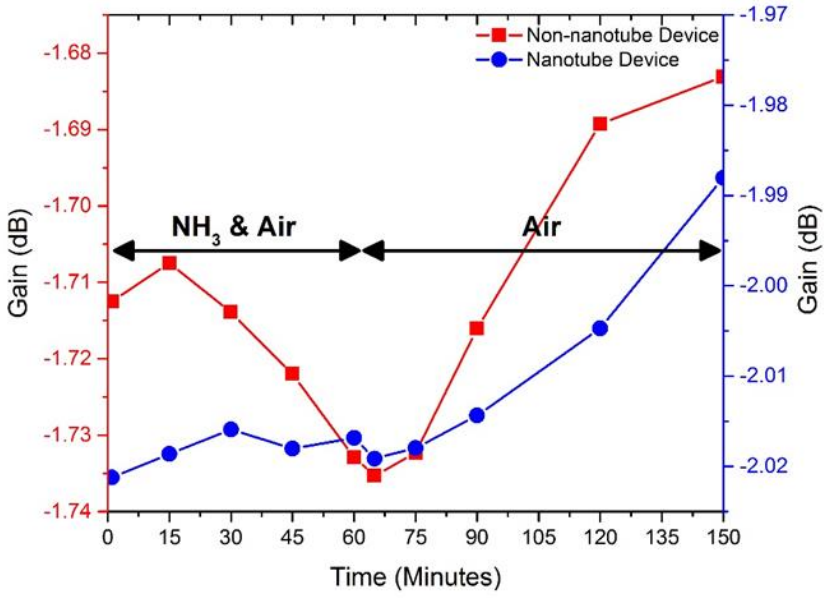

FIG. 6.18. Amplitude shift transient response of nanotube and non-nanotube OFC SAW gas sensors using |S11| measurements and gating sensing channel reflectors from 4.96 µm - 7.07 µm.

We have also measured the sensitivity of the multiwall TiO_2 nanotube device during 45 minute of exposure to 25, 50, 100 and 200 ppm ammonia using the resonant frequency shift of the TiO_2 nanotube layer affecting the reflectors on the sensing channel at room temperature (20°C). The resonant frequency shift is defined as:

$$\Delta f = f_{gas} - f_{air} \tag{6.11}$$

where f_{gas} is the lowest frequency peak point under exposure to air in the frequency domain, while f_{air} is the lowest frequency point in the presence of pure air. Fig. 6.19 shows a nonlinear, monotonic relationship between gas concentration and sensitivity with a detection limit of 100 ppm ammonia.

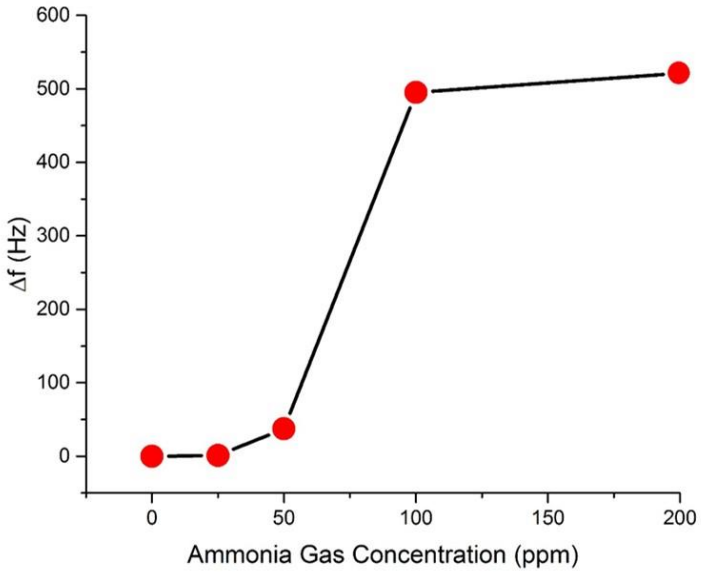

FIG. 6.19. Sensitivity of OFC SAW gas sensor during 45 minute exposure to 25, 50, 100 and 200 ppm ammonia at room temperature.

Chapter 7 Conclusions

A novel, low-temperature fabrication process to selectively form free-standing high-aspect-ratio ZnO nanowires, TiO_2 nanowires, and multiwall TiO_2 nanotubes in a thin, 2.5 μm thick, aluminum film attached to a silicon substrate has been demonstrated and used to form high-aspect-ratio ZnO nanowires on the gate of a metal gate silicon MOSFET. The same fabrication process was optimized to integrated multiwall TiO_2 nanotubes onto the delay line of a OFC SAW gas sensor. The fabrication process of high-aspect ratio metal oxide nanostructures presented is accomplished at low-temperature (< 200 °C) and without the typical electropolishing step required in methods used to form AAO templates in freestanding 100 mm thick aluminum films. By optimizing a multi-step anodization process, ALD deposition and release step, a smooth 2.5 μm thick e-beam evaporated aluminum film was used both for the formation of ZnO nanowires, TiO_2 nanowires and multiwall TiO_2 nanotubes as well as device metallization and interconnects. ZnO nanowires, TiO_2 nanowires and multiwall TiO_2 nanotubes are in a dense array ($1.3x10^{10}$ – $2.3x10^{10}$ nanowires/cm^2) with 40-90 nm diameter and 1-1.7 μm in height (~10:1 and ~18:1 aspect ratio). SEM, EDX , TEM and Hall measurements show high purity and stoichiometric polycrystalline metal oxide nanostructures with excellent electrical properties. The resulting high-aspect ratio metal oxide nanostructure array enhances the sensor surface area by up 220X over a conventional flat film. The response of ChemFETs with ZnO nanowires, TiO_2 nanowires and multiwall TiO_2 nanotubes were measure at room temperature and showed a changed of the I/V characteristics during exposure to ammonia. In addition, OFC SAW device with multiwall TiO_2 nanotubes were also measured at room temperature and showed that the multiwall TiO_2 nanotubes changed the characteristics of

the acoustic wave during exposure to ammonia. This suggests that the low-temperature fabrication process presented in this work could serve as an active component in ChemFETs and SAW gas sensor devices.

In addition, the low-temperature (< 200 °C) nature of this novel process allows it to be integrated with a variety of microelectronic materials and device types, including silicon based microelectronics, III-V semiconductors, flexible or smart material substrates, particularly for the fabrication of high-sensitivity sensors. While demonstrated using ZnO and TiO_2 as sensing material, the integrated thin film AAO template developed here can potentially be used with a variety of materials with different nanostructure shapes.

References

[1] Ljubiša Ristić. *Sensor Technology and Devices Sensor Technology and Devices* 1994.

[2] K. S. Lion. Transducers: Problems and prospects. *Industrial Electronics and Control Instrumentation, IEEE Transactions On (1),* pp. 2-5. 1969.

[3] P. Gründler. P. Gründler. "Introduction - sensor and sensor science," in *Chemical Sensors: An Introduction for Scientists and Engineers* 2007.

[4] N. Yamazoe and K. Shimanoe. N. Yamazoe and K. Shimanoe. "Fundamentals of semiconductor gas sensors," in *Semiconductor Gas Sensors*, R. Jaaniso and O. K. Tan, Eds. 2013, .

[5] A. J. Ricco. SAW chemical sensors. *Interface 3(4),* pp. 38-44. 1994.

[6] B. H. Fisher and D. C. Malocha. B. H. Fisher and D. C. Malocha. A study on the aging of ultra-thin palladium films on SAW hydrogen gas sensors. A study on the aging of ultra-thin palladium films on SAW hydrogen gas sensors. 2010, .

[7] S. J. Ippolito, A. Trinchi, D. A. Powell and W. Wlodarski. S. "Accoustic wave gas and vapor sensors," in *Solid State Gas Sensing*, E. Comini, G. Faglia and G. Sberveglieri, Eds. 2008, .

[8] W. C. Wilson, D. C. Malocha, N. Kozlovski, D. R. Gallagher, B. Fisher, J. Pavlina, N. Saldanha, D. Puccio and G. M. Atkinson. Orthogonal frequency coded SAW sensors for aerospace SHM applications. *IEEE Sensors Journal 9(11),* pp. 1546-1556. 2009.

[9] D. Puccio, D. C. Malocha, N. Saldanha, D. R. Gallagher and J. H. Hines. Orthogonal frequency coding for SAW tagging and sensors. *IEEE Trans. Ultrason. Ferroelectr. Freq. Control 53(2),* pp. 377-384. 2006.

[10] D. C. Malocha, J. Pavlina, D. Gallagher, N. Kozlovski, B. Fisher, N. Saldanha and D. Puccio. Orthogonal frequency coded SAW sensors and RFID design principles.2008.

[11] D. C. Malocha, D. Puccio and D. Gallagher. D. C. Orthogonal frequency coding for SAW device applications. 2004.

[12] B. Fisher. Surface acoustic wave (SAW) cryogenic liquid and hydrogen gas sensors. 2012.

[13] J. R. Humphries and D. C. Malocha. Wireless SAW strain sensor using orthogonal frequency coding. *IEEE Sensors Journal 15(10),* pp. 5527-5534. 2015.

[14] W. Wilson. Multifunctional orthogonally-frequency-coded saw strain sensor. 2013.

[15] D. Puccio, D. C. Malocha, D. Gallagher and J. Hines. SAW sensors using orthogonal frequency coding. SAW sensors using orthogonal frequency coding. 2004, .

[16] B. H. Fisher and D. C. Malocha. Cryogenic liquid sensing using SAW devices. 2007, .

[17] V. A. Smyntyna. *Semiconductor Materials for Gas Sensors Semiconductor Materials for Gas Sensors* 2013.

[18] N. W. Emanetoglu, J. Zhu, Y. Chen, J. Zhong, Y. Chen and Y. Lu. Surface acoustic wave ultraviolet photodetectors using epitaxial ZnO multilayers grown on r-plane sapphire. *Appl. Phys. Lett. 85(17),* pp. 3702-3704. 2004.

[19] X. D. Wang, C. Neff, E. Graugnard, Y. Ding, J. S. King, L. A. Pranger, R. Tannenbaum, Z. L. Wang and C. J. Summers. Photonic crystals fabricated using patterned nanorod arrays. *Adv. Mater. 17(17),* pp. 2103-2106. 2005.

[20] J. Lim, C. Kang, K. Kim, I. Park, D. Hwang and S. Park. UV electroluminescence emission from ZnO light-emitting diodes grown by high-temperature radiofrequency sputtering. *Adv. Mater. 18(20),* pp. 2720-2724. 2006.

[21] Z. Fan, D. Wang, P. Chang, W. Tseng and J. G. Lu. ZnO nanowire field-effect transistor and oxygen sensing property. *Appl. Phys. Lett. 85(24),* pp. 5923-5925. 2004.

[22] K. Keis, E. Magnusson, H. Lindström, S. Lindquist and A. Hagfeldt. A 5% efficient photoelectrochemical solar cell based on nanostructured ZnO electrodes. *Sol. Energ. Mat. Sol. C. 73(1),* pp. 51-58. 2002.

[23] T. S. Herng, A. Kumar, C. S. Ong, Y. P. Feng, Y. H. Lu, K. Y. Zeng and J. Ding. Investigation of the non-volatile resistance change in noncentrosymmetric compounds. *Sci. Rep. 2*pp. 587. 2012.

[24] S. Lee, H. Kim, D. Yun, S. Rhee and K. Yong. Resistive switching characteristics of ZnO thin film grown on stainless steel for flexible nonvolatile memory devices. *Appl. Phys. Lett. 95(26),* pp. 262113. 2009.

[25] Z. L. Wang and J. Song. Piezoelectric nanogenerators based on zinc oxide nanowire arrays. *Science 312(5771),* pp. 242-246. Apr 14, 2006.

[26] L. Vayssieres. Growth of arrayed nanorods and nanowires of ZnO from aqueous solutions. *Adv. Mater. 15(5),* pp. 464-466. 2003.

[27] G. Yi, C. Wang and W. I. Park. ZnO nanorods: Synthesis, characterization and applications. *Semicond. Sci. Tech. 20(4),* pp. S22. 2005.

[28] X. Wang, J. Zhang and Z. Zhu. Ammonia sensing characteristics of ZnO nanowires studied by quartz crystal microbalance. *Appl. Surf. Sci. 252(6),* pp. 2404-2411. 2006.

[29] S. Raychaudhuri, S. A. Dayeh, D. Wang and E. T. Yu. Precise semiconductor nanowire placement through dielectrophoresis. *Nano Lett. 9(6),* pp. 2260-2266. 2009.

[30] E. M. Freer, O. Grachev, X. Duan, S. Martin and D. P. Stumbo. High-yield self-limiting single-nanowire assembly with dielectrophoresis. *Nat. Nanotechnol. 5(7),* pp. 525-530. 2010.

[31] Y. Chang and F. C. Hong. The fabrication of ZnO nanowire field-effect transistors by roll-transfer printing. *Nanotechnology 20(19),* pp. 195302. 2009.

[32] E. Comini. "One- and two-dimensional metal oxide nanostructures for chemical sensing," in *Semiconductor Gas Sensors*, R. Jaaniso and O. K. Tan, Eds. 2013, .

[33] X. Wang, Q. Li, Z. Liu, J. Zhang, Z. Liu and R. Wang. Low-temperature growth and properties of ZnO nanowires. *Appl. Phys. Lett. 84(24),* pp. 4941-4943. 2004.

[34] R. Cross, M. M. De Souza and E. S. Narayanan. A low temperature combination method for the production of ZnO nanowires. *Nanotechnology 16(10),* pp. 2188. 2005.

[35] J. X. Wang, X. W. Sun, Y. Yang, H. Huang, Y. C. Lee, O. K. Tan and L. Vayssieres. Hydrothermally grown oriented ZnO nanorod arrays for gas sensing applications. *Nanotechnology 17(19),* pp. 4995. 2006.

[36] L. E. Greene, M. Law, J. Goldberger, F. Kim, J. C. Johnson, Y. Zhang, R. J. Saykally and P. Yang. Low-temperature wafer-scale production of ZnO nanowire arrays. *Angew. Chem. Int. Edit. 42(26),* pp. 3031-3034. 2003.

[37] E. Comini and G. Sberveglieri. Metal oxide nanowires as chemical sensors. *Mater. Today 13(7),* pp. 36-44. 2010.

[38] M. Grätzel. Photoelectrochemical cells. *Nature 414(6861),* pp. 338-344. 2001.

[39] M. Grätzel. Conversion of sunlight to electric power by nanocrystalline dye-sensitized solar cells. *J. Photochem. Photobiol. A. 164(1),* pp. 3-14. 2004.

[40] M. Grätzel. Dye-sensitized solid-state heterojunction solar cells. *MRS Bull 30(01),* pp. 23-27. 2005.

[41] Q. Wei, K. Hirota, K. Tajima and K. Hashimoto. Design and synthesis of TiO2 nanorod assemblies and their application for photovoltaic devices. *Chemistry of Materials 18(21),* pp. 5080-5087. 2006.

[42] A. L. Linsebigler, G. Lu and J. T. Yates. Photocatalysis on TiO2 surfaces: Principles, mechanisms, and selected results. *Chem. Rev. 95(3),* pp. 735-758. 1995.

[43] M. R. Hoffmann, S. T. Martin, W. Choi and D. W. Bahnemann. Environmental applications of semiconductor photocatalysis. *Chem. Rev. 95(1),* pp. 69-96. 1995.

[44] K. Hashimoto, H. Irie and A. Fujishima. TiO2 photocatalysis: A historical overview and future prospects. *Japanese Journal of Applied Physics 44(12R),* pp. 8269. 2005.

[45] A. E. Aliev and H. W. Shin. Nanostructured materials for electrochromic devices. *Solid State Ionics 154*pp. 425-431. 2002.

[46] L. Vayssieres, Y. Alfredsson and H. Siegbahn. Electrochromic properties of bis (phthalocyaninato) lutetium (III) sensitized nanostructured anatase TiO2 thin films. *Electrochemical and Solid-State Letters 2(12),* pp. 648-650. 1999.

[47] A. Ghicov, S. P. Albu, J. M. Macak and P. Schmuki. High-Contrast electrochromic switching using transparent Lift-Off layers of Self-Organized TiO2 nanotubes. *Small 4(8),* pp. 1063-1066. 2008.

[48] F. Pichot, S. Ferrere, R. J. Pitts and B. A. Gregg. Flexible Solid-State photoelectrochromic windows. *J. Electrochem. Soc. 146(11),* pp. 4324-4326. 1999.

[49] G. De Filpo, F. P. Nicoletta and G. Chidichimo. Flexible nano-photo-electrochromic film. *Chemistry of Materials 18(19),* pp. 4662-4666. 2006.

[50] O. K. Varghese, D. Gong, M. Paulose, K. G. Ong and C. A. Grimes. Hydrogen sensing using titania nanotubes. *Sensors Actuators B: Chem. 93(1),* pp. 338-344. 2003.

[51] O. K. Varghese, D. Gong, M. Paulose, K. G. Ong, E. C. Dickey and C. A. Grimes. Extreme changes in the electrical resistance of titania nanotubes with hydrogen exposure. *Adv Mater 15(7-8),* pp. 624-627. 2003.

[52] Y. Zhu, J. Shi, Z. Zhang, C. Zhang and X. Zhang. Development of a gas sensor utilizing chemiluminescence on nanosized titanium dioxide. *Anal. Chem. 74(1),* pp. 120-124. 2002.

[53] C. A. Grimes. Synthesis and application of highly ordered arrays of TiO 2 nanotubes. *Journal of Materials Chemistry 17(15),* pp. 1451-1457. 2007.

[54] B. C. Yadav, R. K. Shukla and L. M. Bali. Sol-gel processed TiO 2 films on U-shaped glass-rods as optical humidity sensor. 2005.

[55] B. C. Yadav, N. K. Pandey, A. K. Srivastava and P. Sharma. Optical humidity sensors based on titania films fabricated by sol–gel and thermal evaporation methods. *Measurement Science and Technology 18(1),* pp. 260. 2006.

[56] E. Comini, G. Faglia, G. Sberveglieri, Y. X. Li, W. Wlodarski and M. K. Ghantasala. Sensitivity enhancement towards ethanol and methanol of TiO 2 films doped with pt and nb. *Sensors Actuators B: Chem. 64(1),* pp. 169-174. 2000.

[57] G. K. Mor, M. A. Carvalho, O. K. Varghese, M. V. Pishko and C. A. Grimes. A room-temperature TiO 2-nanotube hydrogen sensor able to self-clean photoactively from environmental contamination. *J. Mater. Res. 19(02),* pp. 628-634. 2004.

[58] J. Zhao, X. Wang, R. Chen and L. Li. Fabrication of titanium oxide nanotube arrays by anodic oxidation. *Solid State Commun. 134(10),* pp. 705-710. 2005.

[59] Y. J. Choi, Z. Seeley, A. Bandyopadhyay, S. Bose and S. A. Akbar. Aluminum-doped TiO 2 nano-powders for gas sensors. *Sensors Actuators B: Chem. 124(1),* pp. 111-117. 2007.

[60] T. Chou, T. Ling, M. Yang and C. Liu. Micro and nano scale metal oxide hollow particles produced by spray precipitation in a liquid–liquid system. *Materials Science and Engineering: A 359(1),* pp. 24-30. 2003.

[61] S. Nakade, S. Kambe, M. Matsuda, Y. Saito, T. Kitamura, Y. Wada and S. Yanagida. Electron transport in electrodes consisting of metal oxide nano-particles filled with electrolyte solution. *Physica E: Low-Dimensional Systems and Nanostructures 14(1),* pp. 210-214. 2002.

[62] P. Viswanathamurthi, N. Bhattarai, C. K. Kim, H. Y. Kim and D. R. Lee. Ruthenium doped TiO2 fibers by electrospinning. *Inorganic Chemistry Communications 7(5),* pp. 679-682. 2004.

[63] B. K. Tay, Z. W. Zhao and D. Chua. Review of metal oxide films deposited by filtered cathodic vacuum arc technique. *Materials Science and Engineering: R: Reports 52(1),* pp. 1-48. 2006.

[64] M. Y. Afridi, J. S. Suehle, M. E. Zaghloul, D. W. Berning, A. R. Hefner, R. E. Cavicchi, S. Semancik, C. B. Montgomery and C. J. Taylor. A monolithic CMOS microhotplate-based gas sensor system. *IEEE Sensors Journal 2(6),* pp. 644-655. 2002.

[65] T. Toccoli, S. Capone, L. Guerini, M. Anderle, A. Boschetti, E. Iacob, V. Micheli, P. Siciliano and S. Iannotta. Growth of titanium dioxide films by cluster supersonic beams for VOC sensing applications. *IEEE Sensors Journal 3(2),* pp. 199-205. 2003.

[66] B. Karunagaran, P. Uthirakumar, S. J. Chung, S. Velumani and E. Suh. TiO 2 thin film gas sensor for monitoring ammonia. *Mater Charact 58(8),* pp. 680-684. 2007.

[67] W. Lee and S. Park. Porous anodic aluminum oxide: Anodization and templated synthesis of functional nanostructures. *Chem. Rev. 114(15),* pp. 7487-7556. 2014.

[68] L. Menon. L. Menon. "Synthesis of nanowires using porous alumina," in *Quantum Dots and Nanowires*, S. Bandyopadhyay and H. S. Nalwa, Eds. 2003, .

[69] H. Masuda and K. Fukuda. Ordered metal nanohole arrays made by a two-step replication of honeycomb structures of anodic alumina. *Science 268(5216),* pp. 1466-1468. Jun 9, 1995.

[70] Z. Yao, C. Wang, Y. Li and N. Kim. AAO-assisted synthesis of highly ordered, large-scale TiO 2 nanowire arrays via sputtering and atomic layer deposition. *Nanoscale Research Letters 10(1),* pp. 166. 2015.

[71] D. Gu, H. Baumgart, T. M. Abdel-Fattah and G. Namkoong. Synthesis of nested coaxial multiple-walled nanotubes by atomic layer deposition. *ACS Nano 4(2),* pp. 753-758. 2010.

[72] R. F. Pierret. "MOS fundamentals," in *Semiconductor Device Fundamentals* 1996.

[73] "Mosfet," in *Physics of Semiconductor Devices* Hoboken, NJ: Wiley-Interscience, 1981, pp. 431.

[74] J. W. Gardner, P. K. Guha, F. Udrea and J. Covington. CMOS interfacing for integrated gas sensors: A review. *IEEE Sens. J. 10(12),* pp. 1833-1848. 2010.

[75] J. F. Ross, I. Robins and B. C. Webb. The ammonia sensitivity of platinum-gate MOSFET devices: Dependence on gate electrode morphology. *Sensor Actuator 11(1),* pp. 73-90. 1987.

[76] I. Lundström, S. Shivaraman, C. Svensson and L. Lundkvist. A hydrogen− sensitive MOS field− effect transistor. *Appl. Phys. Lett. 26(2),* pp. 55-57. 1975.

[77] M. Andersson, R. Pearce and A. L. Spetz. New generation SiC based field effect transistor gas sensors. *Sensors Actuators B: Chem. 179*pp. 95-106. 2013.

[78] C. Baratto, E. Comini, G. Faglia, G. Sberveglieri, M. Zha and A. Zappettini. Metal oxide nanocrystals for gas sensing. *Sensors Actuators B: Chem. 109(1),* pp. 2-6. 2005.

[79] A. Kolmakov, Y. Zhang, G. Cheng and M. Moskovits. Detection of CO and O2 using tin oxide nanowire sensors. *Adv Mater 15(12),* pp. 997-1000. 2003.

[80] M. Anderson, A. Lloyd and R. Pearce. "Recent trends in silicon carbide (SiC) and graphene-based gas sensors," in *Semiconductor Gas Sensors*, R. Jaaniso and O. K. Tan, Eds. 2013.

[81] N. Yamazoe, G. Sakai and K. Shimanoe. Oxide semiconductor gas sensors. *Catalysis Surveys from Asia 7(1),* pp. 63-75. 2003.

[82] N. Yamazoe and K. Shimanoe. Theory of power laws for semiconductor gas sensors. *Sensors Actuators B: Chem. 128(2),* pp. 566-573. 2008.

[83] M. J. Madou and S. R. Morrison. M. J. Madou and S. R. Morrison. "Solid-state background," in *Chemical Sensing with Solid State Devices* 2012, .

[84] N. Barsan, M. Huebner and U. Weimar. "Conduction mechanism in semiconducting impact and transduction," in *Semiconductor Gas Sensors*, R. Jaaniso and O. K. Tan, Eds. 2013, .

[85] N. Barsan and U. Weimar. Understanding the fundamental principles of metal oxide based gas sensors; the example of CO sensing with SnO2 sensors in the presence of humidity. *Journal of Physics: Condensed Matter 15(20),* pp. R813. 2003.

[86] W. Lim, J. S. Wright, B. P. Gila, J. L. Johnson, A. Ural, T. Anderson, F. Ren and S. J. Pearton. Room temperature hydrogen detection using pd-coated GaN nanowires. *Appl. Phys. Lett. 93(7),* pp. 72109. 2008.

[87] W. Lim, J. S. Wright, B. P. Gila, S. J. Pearton, F. Ren, W. Lai, L. Chen, M. Hu and K. Chen. Selective-hydrogen sensing at room temperature with pt-coated InN nanobelts. *Appl. Phys. Lett. 93(20),* pp. 202109. 2008.

[88] J. L. Johnson, Y. Choi, A. Ural, W. Lim, J. S. Wright, B. P. Gila, F. Ren and S. J. Pearton. Growth and characterization of GaN nanowires for hydrogen sensors. *J Electron Mater 38(4),* pp. 490-494. 2009.

[89] R. C. Furneaux, W. R. Rigby and A. P. Davidson. The formation of controlled-porosity membranes from anodically oxidized aluminium. *Nature 337(6203),* pp. 147-149. 1989.

[90] Q. Yuan, Y. Zhao, L. Li and T. Wang. Ab initio study of ZnO-based gas-sensing mechanisms: Surface reconstruction and charge transfer. *The Journal of Physical Chemistry C 113(15),* pp. 6107-6113. 2009.

[91] M. Z. Atashbar, S. Krishnamurthy and G. Korotcenkov. "Basic principles of chemical sensor operation," in *Chemical Sensors: Fundamentals of Sensing Materials Volume 1: General Approaches.* , G. Korotcenkov, Ed. 2011, .

[92] J. Janata. J. Janata. "Mass sensors," in *Principles of Chemical Sensors* 2010, .

[93] J. W. Grate, S. J. Martin and R. M. White. Acoustic wave microsensors. *Anal. Chem. 65(21),* pp. 948A. 1993.

[94] A. J. Ricco and S. J. Martin. Thin metal film characterization and chemical sensors: Monitoring electronic conductivity, mass loading and mechanical properties with surface acoustic wave devices. *Thin Solid Films 206(1-2),* pp. 94-101. 1991.

[95] H. Wohltjen. Mechanism of operation and design considerations for surface acoustic wave device vapour sensors. *Sensors and Actuators 5(4),* pp. 307-325. 1984.

[96] X. Chen, D. M. Li, S. F. Liang, S. Zhan and M. Liu. Gas sensing properties of surface acoustic wave NH3 gas sensor based on pt doped polypyrrole sensitive film. *Sensors Actuators B: Chem. 177*pp. 364-369. 2013.

[97] L. Al-Mashat, H. D. Tran, W. Wlodarski, R. B. Kaner and K. Kalantar-zadeh. Polypyrrole nanofiber surface acoustic wave gas sensors. *Sensors Actuators B: Chem. 134(2),* pp. 826-831. 2008.

[98] M. Penza, E. Milella and V. I. Anisimkin. Monitoring of NH3 gas by LB polypyrrole-based SAW sensor. *Sensors Actuators B: Chem. 47(1–3),* pp. 218-224. 1998.

[99] M. Penza, E. Milella and V. I. Anisimkin. Gas sensing properties of langmuir-blodgett polypyrrole film investigated by surface acoustic waves. *IEEE Trans. Ultrason. Ferroelectr. Freq. Control 45(5),* pp. 1125-1132. 1998.

[100] H. Kim and J. Lee. Highly sensitive and selective gas sensors using p-type oxide semiconductors: Overview. *Sensors Actuators B: Chem. 192*pp. 607-627. 2014.

[101] W. P. Jakubik. Investigations of thin film structures of WO3 and WO3 with pd for hydrogen detection in a surface acoustic wave sensor system. *Thin Solid Films 515(23),* pp. 8345-8350. 2007.

[102] M. Hoummady, A. Campitelli and W. Wlodarski. Acoustic wave sensors: Design, sensing mechanisms and applications. *Smart Mater. Struct. 6(6),* pp. 647. 1997.

[103] Z. P. Khlebarov, A. I. Stoyanova and D. I. Topalova. Surface acoustic wave gas sensors. *Sensors and Actuators B: Chemical 8(1),* pp. 33-40. 1992.

[104] A. J. Ricco, S. J. Martin and T. E. Zipperian. Surface acoustic wave gas sensor based on film conductivity changes. *Sensors and Actuators 8(4),* pp. 319-333. 1985.

[105] B. H. Fisher and D. C. Malocha. Study of the acoustoelectric effect for SAW sensors. *IEEE Trans. Ultrason. Ferroelectr. Freq. Control 57(3),* 2010.

[106] W. P. Jakubik. Surface acoustic wave-based gas sensors. *Thin Solid Films 520(3),* pp. 986-993. 2011.

[107] W. P. Jakubik, M. W. Urbańczyk, S. Kochowski and J. Bodzenta. Palladium and phthalocyanine bilayer films for hydrogen detection in a surface acoustic wave sensor system. *Sensors Actuators B: Chem. 96(1–2),* pp. 321-328. 2003.

[108] S. J. Martin, G. C. Frye and S. D. Senturia. Dynamics and response of polymer-coated surface acoustic wave devices. effect of viscoelastic properties and film resonance. *Analytical Chemistry (Washington);(United States) 66(14),* 1994.

[109] "SAW device operation and measurement," in *Surface-Launched Acoustic Wave Sensors: Chemical Sensing and Thin-Film Characterization*, J. D. Winefordner, Ed. Wiley-interscience, 1997, pp. 110-116.